LOW ENERGY EXCITATIONS IN CUPRATE HIGH TEMPERATURE SUPERCONDUCTORS: ANGLE-RESOLVED PHOTOEMISSION SPECTROSCOPY STUDIES

A DISSERTATION
SUBMITTED TO THE DEPARTMENT OF APPLIED PHYSICS
AND THE COMMITTEE ON GRADUATE STUDIES
OF STANFORD UNIVERSITY
IN PARTIAL FULFILLMENT OF THE REQUIREMENTS
FOR THE DEGREE OF
DOCTOR OF PHILOSOPHY

Inna Vishik
August 2013

I certify that I have read this dissertation and that, in my opinion, it is fully adequate in scope and quality as a dissertation for the degree of Doctor of Philosophy.

(Zhi-Xun Shen) Principal Adviser

I certify that I have read this dissertation and that, in my opinion, it is fully adequate in scope and quality as a dissertation for the degree of Doctor of Philosophy.

(Tom Devereaux)

I certify that I have read this dissertation and that, in my opinion, it is fully adequate in scope and quality as a dissertation for the degree of Doctor of Philosophy.

(Steve Kivelson)

Approved for the University Committee on Graduate Studies

Abstract

The mechanism of superconductivity in the cuprate high temperature superconductors is an enduring problem in condensed matter physics, and a detailed experimental phenomenology is a crucial starting point for microscopic understanding. Angle-resolved photoemission spectroscopy (ARPES) measures electronic structure in momentum-space. Low-energy excitations in the cuprates, including the superconducting gap, are known to be anisotropic in momentum space, so the momentum resolution afforded by ARPES is key to understanding the physics and uncovering the mechanism. This dissertation presents experiments which pursue the cuprate superconductivity problem from several angles: understanding electron-boson coupling which may be involved in mediating superconductivity (Chapters 6 and 7 and Appendix B), understanding the momentum-space structure of the normal state pseudogap (Chapter 5 and Appendix A), understanding how superconductivity coexists with the pseudogap and other phases (Chapters 3 and 4). Much of this work took advantage of a recent development in ARPES technology, using a UV laser as a light source, which allows experiments to be performed with superior energy and momentum resolution. These experiments highlight the wealth of information that is available in ARPES data, including dispersions, scattering rates, and spectral gaps, and they demonstrate the importance of exploring these variables comprehensively as a function of temperature, doping, and momentum.

One of the quantities that can be measured most precisely with ARPES is the spectral gap. When the gap is attributed to an ordered electronic state, its magnitude and momentum-dependence can give information about the order parameter. Chapter 3 comprehensively studies gaps in/near the superconducting state with a

focus on near-nodal momenta. It turns out that the near-nodal superconducting gap sensitively reflects other phases which coexist with superconductivity, such as the pseudogap. Evidence of momentum-dependent competition between superconductivity and the pseudogap is observed, with the pseudogap relinquishing a portion of the Fermi surface when it is suppressed at low temperature and/or higher doping. With this information, a revised phase diagram is proposed which consolidates conflicting phase diagrams in the literature.

When the pseudogap coexists with superconductivity, this coexistence is often described as a nodal/antinodal dichotomy, with superconductivity dominating near the node and the pseudogap, which is now thought to be a distinct phase, dominating near the antinode. However, there is subtlety in this dichotomy, as discussed in Chapter 4, because superconducting quasiparticles exist over the entire Fermi surface below T_c, even at momenta where the gap magnitude reflects strong influence from the pseudogap.

An important question in the cuprates is the momentum space gap structure of the pseudogap, as this information can narrow down the field of plausible theoretical descriptions. Chapter 5 studies the lineshape above T_c and finds that the maximum Fermi arc length at T_c is shorter than previously thought. Appendix A explores other proposed data analysis techniques in order to assess what information they can and cannot give about the pseudogap.

Another quantity that ARPES can measure precisely is the band disperion, and there are 'kinks' in cuprate dispersions which indicate strong electron-boson coupling. The identity of the bosons and whether they are related to superconductivity is not answered for most kinks in cuprates. Future directions for reaching those answers are explored in Appendix B. Chapter 6 presents a new kink at very low energy ($\approx$10 meV) which was discovered by laser ARPES. This kink gets stronger with underdoping, producing a doping dependent Fermi velocity, which allows correspondence between ARPES and bulk thermal conductivity measurements. The energy position of this low energy kink follows the momentum dependence of the d-wave superconducting gap away from the node, indicating that the coupling is peaked at small $\mathbf{q}$. The doping and momentum dependence agrees with theoretical calculations which

consider electrons coupled to acoustic phonons. Though the energy is too low to be the cause of cuprate superconductivity, coupling to acoustic modes may enhance T_c. Another promising direction for uncovering the connection between kinks and superconductivity is studying Hg1201 which has a very high T_c for a single-layer cuprate. Chapter 7 presents the highest quality ARPES data on Hg1201 to date, measuring the magnitude of the superconducting gap and pinning down the nodal kink energy for the first time.

Acknowledgement

I want to begin by thanking Z.-X. for being such a good adviser and a true role model of how to manage a research group and be a good scientist. He knows how to motivate people without being a micromanager, and how to reassure us when papers get rejected from 3 journals. I appreciate that he is not dogmatic and is open to revising his views when new experimental data warrants. His drive to innovate and move into new research areas is inspiring. His network of scientific friends and collaborators is incredible and a tremendous resource for the students. Most of all, I am thankful that he gives his students the space and freedom to find their own direction as scientists.

I am grateful the other members of my reading committee, Tom Devereaux and Steve Kivelson. Tom has been like a second advisor to me, and much of the theory I understand has been patiently explained to me (maybe several times) by him and his group members. Most amazing is that Tom still manages to write and run codes now that he is director of SIMES. Steve's scientific ideas stick in my mind vividly. He has also drilled into my mind the importance of using precise language. I will never again use the word 'universal' to describe something that is merely doping and/or materials independent (though other people do). My undergraduate advisor Martin Greven has remained an important mentor throughout my PhD, always offering helpful guidance on my career. Additionally, I am grateful to him and his group members for providing and preparing Hg1201 samples for our experiments.

I want to thank Andrew Merriam of Lumeras (where we got our new laser from!) for teaching me everything I know about optics and UV optics cleanliness and other miscellaneous lab tricks.

The Shen group is a vibrant wonderful group of people, and it was a true privilege to work with such smart, nice, and unique colleagues. Any problem you might have, from instrumentation to programming to writing, there is someone who can guide you. The people I worked most closely with in the past few months were Ming, Yu, and Zhongkai. Without them, the 11eV laser would not have gotten off the ground. They are reliable, effective, eager, and brilliant, and it was so much fun to work with this bunny-suit-clad team. Go team Tyvek! My first mentor when I joined the Shen group was Wei-Sheng, and he taught me everything I needed to know to get started with ARPES on cuprates. He also did many of the foundational experiments which motivated my research. Most of all, he gave me the confidence to be an independent experimenter, and he also granted me dominion over the 7eV laser, which was extremely fruitful for my research. In recent years, I have worked closely with Makoto, enjoying a nodal-antinodal dichotomy in studying Bi-2212. Makoto is a truly creative scientist, and I have been inspired many times by his innovative ARPES experiments and data analysis. Best of all, he is patient in mentoring the younger folks studying cuprates. In the basement and beamline, Felix, Rob, Donghui, and now JJ have patiently mentored me in UHV instrumentation and they have been tireless in keeping all our equipment running. I want to acknowledge Patrick, Jonathan, and Shuolong for all of their optics and laser expertise, a lifesaver for both the 7eV and 11eV lasers.

I was extremely fortunate to work in McCullough and be part of SIMES with many helpful collaborators and/or critics including Brian, Michael, Steve, and Beth from Tom's group and George and Sam from Steve's group. In addition, Trish, our Shen group admin, was always extremely effective in tracking down ZX, and always maintained a chipper demeanor despite the large amount of work on her plate. Mark Gibson is another valuable person of the McCullough community, tirelessly searching for us throughout McCullough to make sure we receive our urgent shipment. I am also grateful to the SIMES admins who are always so pleasant and helpful: Margo, Chris, Nancy, and Lorraine.

The Applied Physics department admins, Paula and Claire are truly gems in the department. They are such sweet and warm people, and somehow manage to keep

track of all the details of so many students with effectiveness, grace, and patience.

I am grateful for my parents for always giving me lots of love, enrichment, and independence. I couldn't have gotten to this point without their constant reassurance and helpful advice throughout my PhD. Finally, I want to thank my husband Eden. You are an amazing, hilarious, brilliant, and kind person, and I am so grateful that we found each other.

Contents

List of Tables

List of Figures

Chapter 1

Introduction: superconductivity and cuprates

1.1 Superconductivity

1.1.1 Conventional Superconductivity

Conventional superconductivity was first explained by the theory of Bardeen, Cooper, and Schreiffer [1] (BCS). A basic overview can be found in Ref. [2], and is sketched below. Rather than going through a full derivation, this section will highlight key concepts that are used in this thesis.

A superconductor is a charge $2e$ condensate, and the electron pairs (usually singlet) are called called a Cooper pair. Although electrons normally repel each other, interactions with atomic vibrations mediate electron pairing. In the real space picture, an electron moving through a lattice of positively charged ions can displace an ion and create a local excess of positive charge which attracts the next passing electron. This retarded attraction is possible because the atoms are much heavier than the electrons and move slower.

In momentum space, one electron emits a phonon of momentum $\hbar\mathbf{q}$ which is

absorbed by a second electron. This interaction is given by

$$V_{eff}(\mathbf{q},\omega) = |g_{\mathbf{q}\lambda}|^2 \frac{1}{\omega^2 - \omega^2_{\mathbf{q}\lambda}} \tag{1.1}$$

where $\mathbf{q}$ and $\omega_{\mathbf{q}\lambda}$ are the wavevector and energy of the phonon, $g_{\mathbf{q}\lambda}$ is an electron-phonon coupling vertex (matrix element). A negative V_{eff} means attractive interaction. Simplifications make this problem more easily solvable. $g_{\mathbf{q}\lambda}$ is replaced by a constant, $\omega_{\mathbf{q}\lambda}$ is replayed by the Debye frequency (ω_D). Additionally, only electrons within $\pm k_B T$ of the Fermi level are considered, so ω is always much smaller than ω_D at the temperatures relevant to conventional superconductivity. The end result is an energy and momentum independent interaction given by $V_{eff}=-|g_{eff}|^2$, where a factor of $1/\omega_D^2$ has been folded into the effective electron-phonon coupling vertex.

The next step is to show that this attraction yields a bound state. The starting point is two electrons outside a filled Fermi sea at zero temperature. They are located at momenta **k** and -**k** such that the center of mass momentum is zero, which minimizes energy. The wave function is given by

$$\Psi(\mathbf{r}_1,\sigma_1,\mathbf{r}_2,\sigma_2) = \varphi(\mathbf{r}_1 - \mathbf{r}_2)\phi^{spin}_{\sigma_1,\sigma_2} \tag{1.2}$$

Fermionic antisymmetry dictates that for a spin singlet spin wave function (as in BCS superconductors and cuprates), the wave function $\varphi(\mathbf{r}_1\text{-}\mathbf{r}_2)$ must be even under exchange of electrons at positions $\mathbf{r}_1$ and $\mathbf{r}_2$. Expanding in terms of Bloch waves gives

$$\varphi(\mathbf{r}_1 - \mathbf{r}_2) = \sum_{\mathbf{k}} \varphi_{\mathbf{k}} e^{i\mathbf{k}(\mathbf{r}_1 - \mathbf{r}_2)} \tag{1.3}$$

Substituting this into the Schrodinger equation yields

$$E\varphi_{\mathbf{k}} = 2\epsilon_{\mathbf{k}}\varphi_{\mathbf{k}} - |g_{eff}|^2 \sum_{\mathbf{k}'} \varphi_{\mathbf{k}'} \tag{1.4}$$

Where the single particle energies $\epsilon_{\mathbf{k}}$ are referenced to the Fermi level and E is the

total energy of the pair in the two-particle state. Solving this gives

$$\varphi_{\mathbf{k}} = -C|g_{eff}|^2 \frac{1}{E - 2\epsilon_{\mathbf{k}}} \tag{1.5}$$

where

$$C = \sum_{\mathbf{k}} \varphi_{\mathbf{k}} \tag{1.6}$$

The above two equations are combined to give

$$1 = |g_{eff}|^2 \sum_{\mathbf{k}} \frac{1}{E - 2\epsilon_{\mathbf{k}}} = |g_{eff}|^2 g(\epsilon_F) \int_0^{\hbar\omega_D} d\epsilon \frac{1}{E - 2\epsilon} \tag{1.7}$$

where g(ϵ_F) is the density of states at the Fermi level. Solving the integral yield the expression for the bound state energy

$$-E = 2\hbar\omega_D e^{-1/|g_{eff}|^2 g(\epsilon_F)} = 2\hbar\omega_D e^{-1/\lambda} \tag{1.8}$$

where λ is the electron-phonon coupling parameter. BCS theory does not require phonons to provide the pairing interactions. Some other boson would change the form of V_{eff} in Eqn. 1.1. The required starting point is a filled Fermi sea such that g(ϵ_F) is nonzero giving a bound state energy which is also nonzero. Equation 1.8 highlights one of the profound insights of BCS theory–that the Fermi sea is unstable to infinitesimally small attractive interactions.

The coherent many-body wave function describing an aggregate of Cooper pairs is given by

$$|\Psi_{BCS}\rangle = \prod_{\mathbf{k}} (u^*_{\mathbf{k}} + v^*_{\mathbf{k}} \hat{P}^\dagger_{\mathbf{k}}) |0\rangle \tag{1.9}$$

where $\hat{P}^\dagger_{\mathbf{k}} = c^\dagger_{\mathbf{k}\uparrow} c^\dagger_{-\mathbf{k}\downarrow}$ is the pair creation operator, and $|0\rangle$ is the vacuum state. The physical meaning of the parameters $u_{\mathbf{k}}$ and $v_{\mathbf{k}}$ relates to particle number: their magnitude represents the probability that a state at a given momentum is electron-like or hole-like. These parameters follow the normalization constraint $|u_{\mathbf{k}}|^2 + |v_{\mathbf{k}}|^2 = 1$ such that particle number is conserved, and in terms of the band structure, they are

given by the following equations

$$|u_{\mathbf{k}}|^2 = \frac{1}{2}(1 + \frac{\epsilon_{\mathbf{k}} - \mu}{\sqrt{(\epsilon_{\mathbf{k}} - \mu)^2 + |\Delta|^2}}) \tag{1.10}$$

$$|v_{\mathbf{k}}|^2 = \frac{1}{2}(1 - \frac{\epsilon_{\mathbf{k}} - \mu}{\sqrt{(\epsilon_{\mathbf{k}} - \mu)^2 + |\Delta|^2}}) \tag{1.11}$$

where μ is the chemical potential, $\epsilon_{\mathbf{k}}$ is the band dispersion, and Δ is the superconducting gap parameter. Fig. 1.1 illustrates these parameters. In the superconducting state, electron and hole energy levels are hybridized, giving energy eigenvalues $\pm E_{\mathbf{k}} = \sqrt{(\epsilon_{\mathbf{k}} - \mu)^2 + |\Delta|^2}$. At k_F, the lowest lying excitation is at E=$\pm\Delta$ instead of $E = 0$. For k<k_F, $|v_{\mathbf{k}}|^2$ approaches one, meaning states there are predominantly electron-like. For k>k_F, $|u_{\mathbf{k}}|^2$ approaches one, meaning states there are predominantly hole-like. For this reason, the intensity of the electron-like band is shown to fade away for k>k_F. At k_F, $|u_{\mathbf{k}}|^2 = |v_{\mathbf{k}}|^2 = 1/2$, indicating equal hole and electron character. At elevated temperatures below T_c in the cuprates, ARPES can observe both the occupied and a portion of the unoccupied band shown in Fig. 1.1(a), as will be shown in Chapter 4.

In conventional superconductors, the gap parameter Δ at zero temperature is given by

$$|\Delta| = 2\hbar\omega_D e^{-1/\lambda} \approx 1.76 k_B T_c \tag{1.12}$$

where the latter numerical value holds well for many but not all conventional superconductors. The superconducting gap is related to the order parameter, as it is zero above T_c and nonzero below T_c. In BCS superconductors, the superconducting gap is of simple s-wave form–same magnitude and phase at every momentum on the Fermi surface. Spectral gaps such as the superconducting gap can be measured very precisely with ARPES, and is the focus of Chapter. 3

1.1.2 Unconventional superconductors

Unconventional superconductors differ from superconductors described by BCS theory in that their pairing mechanism is not derived from electron-phonon interaction

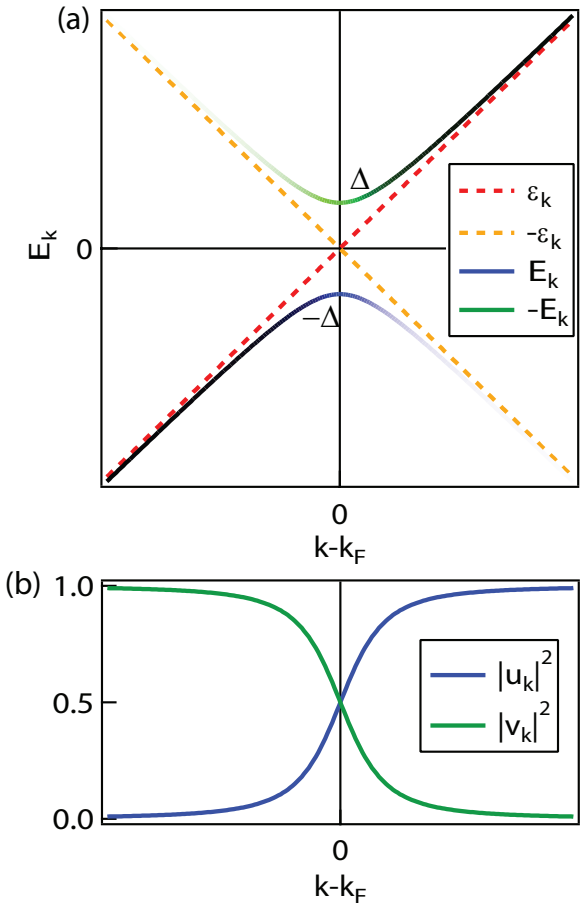

Figure 1.1: (a) Electron (red dashed line) and hole (orange dashed line) energy levels. Energy eigenvalues in superconducting state, $E_{\mathbf{k}} = \sqrt{(\epsilon_{\mathbf{k}} - \mu)^2 + |\Delta|^2}$ are shown in green (blue) for electron (hole) band. (b) $|u_{\mathbf{k}}|^2$ and $|v_{\mathbf{k}}|^2$.

and/or in that their superconducting order parameters are not simple s-wave [3]. This section will discuss a few classes of materials which seem to feature similar physics to the cuprates. In particular, in many unconventional superconductors, superconductivity emerges when another (usually magnetic) phase is pushed to zero temperature via doping or pressure.

One of the first discovered families of unconventional superconductors were the heavy Fermion materials [4], where the f-electron derived bands yield effective masses up to 1000 times the bare electron mass. Superconductivity in heavy Fermion materials was a surprised because there are localized magnetic moments [5]. Heavy

Fermion superconductivity is believed to be mediated by magnetic interactions, and the superconducting order parameter varies among materials. As an example, two commonly studied compounds are UPt_3 and $CeCoIn_5$ with the former thought to have f-wave pairing symmetry and the latter thought to be a d-wave superconductor [6]. Though the T_c is low in heavy Fermion superconductors, some of them provide clean access to quantum critical points–second order phase transitions pushed to zero temperature by a non-thermal control parameter–which are suspected to be involved in superconductivity in cuprates and other unconventional superconductors.

Soon after the heavy Fermions, organic superconductors were discovered. Like cuprates, they feature reduced dimensionality and Mott physics. Like the heavy Fermion materials, superconductivity can be tuned with pressure. Their high critical field, beyond the Pauli limit, suggests that they are triplet superconductors at least in a magnetic field[6].

In 2006, a new family of high T_c materials was discovered [7]–the iron-based superconductors–with T_cs topping 50K in some compounds. Intriguingly, the phase diagram seems similar to the cuprates at first glance as the parent compound features magnetic order. However, this magnetic phase is not a Mott insulator and it coexists with and competes with superconductivity [8]. The mechanism of superconductivity in iron-based materials is still debated, though electron-phonon interaction is not thought to be the culprit. The anisotropy of the gap is also debated and may depend on doping and materials system [9].

1.2 Cuprates

Superconductivity in copper-oxide containing compounds (cuprates) was a nobel-prize winning discovery made by J. Bednorz and K. Müller in 1986 [10]. Motivated by superconductivity in oxygen-doped $SrTiO_3$, they cooled down $LaBaCuO_4$ and discovered that it superconducts below 30K. Many other cuprate superconductors were discovered within the next few years. Significantly, some of these compounds have superconducting transition temperatures higher than 77K, the boiling temperature of liquid nitrogen, opening the possibility for wider application. The highest recorded

T_c is 166K, observed in a Hg-based cuprate under pressure. Cuprate superconductors thus manifest quantum mechanics not only over macroscopic length scales, but at temperatures over 1/2 of room temperature [11].

Cuprates are layered materials whose elementary units are CuO_2 planes, separated by spacer layers containing other atoms (Fig. 1.2). This spacer layer is called the charge reservoir layer because dopant atoms are usually introduced there, rather than directly into the CuO_2 planes. The excess electrons or holes from the dopants go primarily into the CuO_2 planes, and cuprate properties are varied by controlling the charge carrier concentration inside the CuO_2 planes, with possibility for both electron and hole doping. This thesis will focus on the hole-doped side.

Cuprates can have one, two, three, or more CuO_2 layers per unit cell. The T_c is maximum for triple-layer compounds in families where it is possible to synthesize them, but it is difficult to grow large single-phase crystals of most triple layer cuprates which is why most experiments on single crystals are in single and bi-layer cuprates.

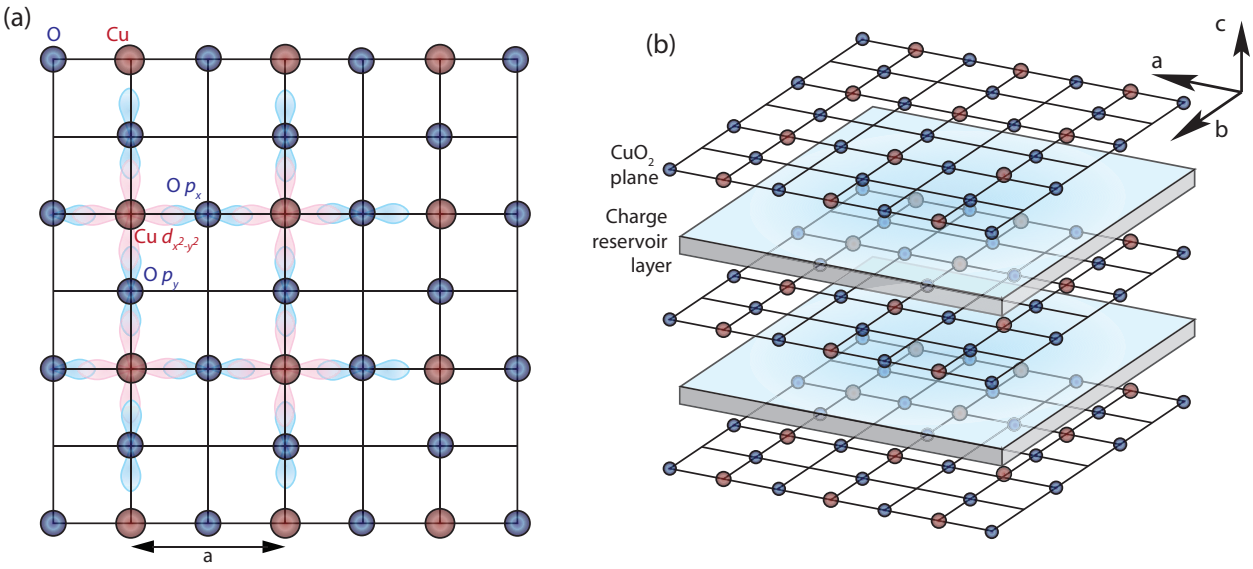

Figure 1.2: (a) CuO_2 plane with Cu atoms in red and oxygen atoms in blue. Cu $d_{x^2-y^2}$ and O $p_{x,y}$ orbitals are also sketched. (b) Schematic of cuprate crystal structure consisting of alternating CuO_2 planes and charge reservoir layers.

Superconductivity originates from the electronic states in the CuO_2 plane, though three dimensional phase coherence is required to have a bulk superconductor. The

charge reservoir layers in most cuprates do not produce bands which cross the Fermi level. Nevertheless, T_c varies substantially even among materials with the same number of CuO_2 planes per unit cell, a result attributed to disorder [12] or chemistry of the spacer layers between the CuO_2 planes [13].

1.2.1 Electronic structure

The electronic structure of the cuprates is derived from Cu-$3d^9$ and O-$2p^6$ bands, as illustrated in Fig. 1.3. In single-layer hole-doped cuprates, the Cu atoms sit in an octahedral environment, surrounded by four planar oxygens (Fig. 1.3(a)) and two apical oxygens. Jahn-Teller distortion–stretching the CuO_6 octahedra along the c-axis–lowers the energy of the z-orbitals relative to the planar orbitals, splitting the t_g and e_{2g} levels into 4 total levels. The lowest bonding and highest antibonding states are derived from hybridization of Cu-$d_{x^2-y^2}$ states and O-$p_{x,y}$ states.

A tight-binding model with only nearest neighbor hopping between Cu-d and O-p orbitals (t_{pd}) can be solved to produce the three bands given by the following expressions [14]:

$$E_{AB,BB}(k_x,k_y) = \frac{\varepsilon_p+\varepsilon_d}{2} \pm \sqrt{(\frac{\varepsilon_p-\varepsilon_d}{2})^2 + 4t_{pd}^2(\sin^2(k_xa/2)+\sin^2(k_ya/2))} \quad (1.13)$$

$$E_{NB} = \varepsilon_p \quad (1.14)$$

This is graphed in Fig. 1.3(c). The antibonding band crosses the Fermi level at half filling (Fig. 1.3(c) and Fig. 1.4(a)) which does not agree with experiment. An on-site repulsion term U is needed to reproduce the insulating parent compound. The parent compound of the cuprates is insulating because the on-site repulsion on the Cu atom is larger than the bandwidth. This parameter splits the antibonding band into the upper Hubbard band (UHB) and lower Hubbard band (LHB), as shown in Fig. 1.4(b). The Cu-O charge transfer gap (energy difference between non-bonding band and upper Hubbard band), Δ, also needs to be considered. In the case of the cuprates, the charge transfer energy is smaller than the Cu on-site repulsion, so Fig. 1.4(c) is a more accurate illustration. When holes are doped into the cuprates,

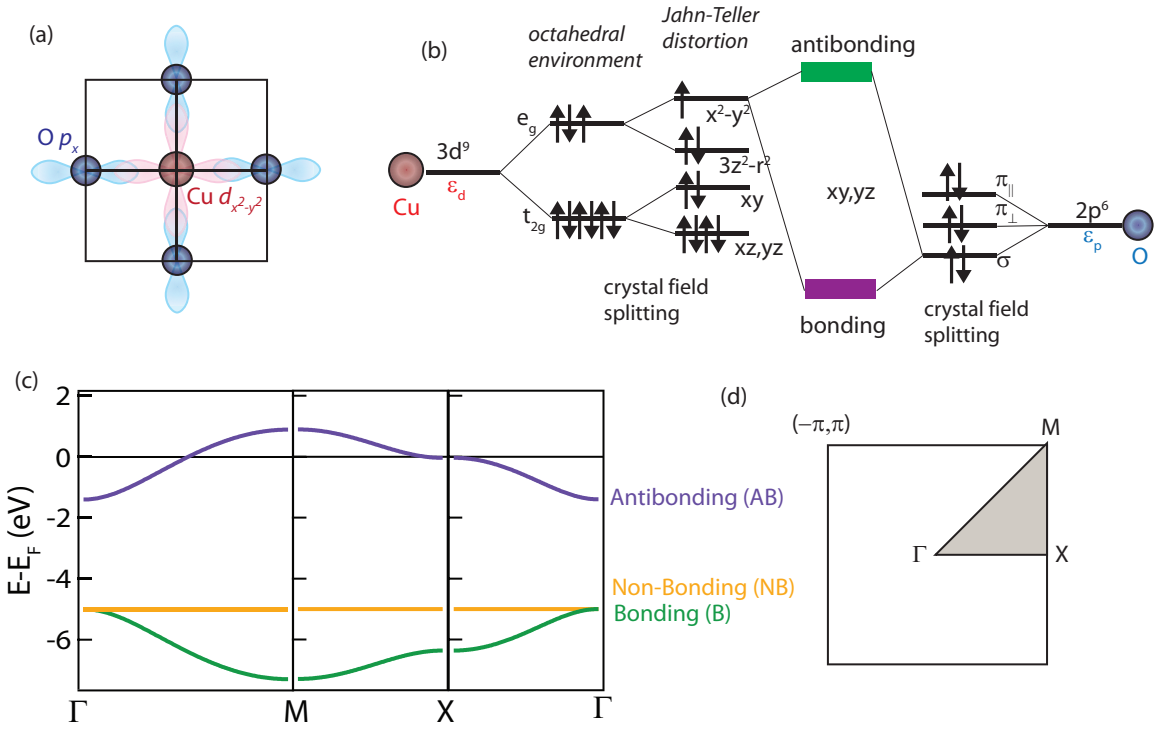

Figure 1.3: (a) Schematic of CuO_2 plaquette. (b) Diagram of crystal field splitting and hybridization of Cu-d levels and O-p levels. (c) Band structure at half filling, from eqn. 1.13 using $\varepsilon_p = -5$ eV, $\varepsilon_d = -1.4$ eV, $t_{pd} = 3.6eV$. (d) 2D projected Brillouin zone for generic CuO_2 plane with irreducible sector shaded in gray.

there are differing proposals to how states at E_F emerge. One possibility is that the chemical potential, μ is pinned inside the charge transfer gap and doping transfers spectral weight from the UHB and bonding band (Fig. 1.4(c)). Another possibility is that μ shifts into the valence band and spectral weight is simultaneously transferred from the UHB by correlation effects (Fig. 1.4(e)). It appears that different scenarios are realized in different cuprates, as the chemical potential appears to be pinned in LSCO, but in other cuprates, doping is realized through a chemical potential shift [15, 16]. With doping, antiferromagnetic correlations are reduced and eventually.

1.2.2 Phase Diagram

The richness of cuprate physics is encompassed in the phase diagram, and the hole-doped side is shown in Fig. 1.5. This phase diagram focuses on phases that will be discussed in this thesis. Generally, antiferromagnetism, superconductivity, and the pseudogap are included in every version of the hole-doped cuprate phase diagram, and other phases shown in Fig. 1.5 are recent developments and/or subject to debate. The composition at zero hole-doping is called the 'parent compound' and it is an antiferromagnetic insulator due to onsite coulomb repulsion. With hole doping, long-range antiferromagnetic order is rapidly suppressed (T_N=0 at 2% in LSCO) but incommensurate fluctuations persist near (0.5, 0.5) to higher dopings [17]. Superconductivity sets in at about 5% hole doping (depending on compound family) and exists within a dome-shaped region. The maximum of the superconducting dome is at p≈0.16 and is called optimal doping (OP). The underdoped (UD) regime refers to p<0.16 and the overdoped (OD) regime refers to p>0.16. In some families, a dip in T_c is observed near 1/8 hole doping, attributed to competing stripe ($La_{2-x}Sr_xCuO_4$ (LSCO)) or charge density wave ($YBa_2Cu_3O_y$ (YBCO)) order. Because of the proximity between the superconducting phase and antiferromagnetic phase, many proposals for the mechanism of superconductivity invoke a pairing boson of spin origin. Some versions of the phase diagram show a spin glass or spin-density wave order at the underdoped edge of the superconducting dome [18, 19]. This will be discussed in the context of ARPES experiments in Chapter 3.

Above T_c, the cuprate phase diagram features an enigmatic phase known as the pseudogap [20]. The pseudogap has an onset temperature T* and signatures in many experimental techniques. Its origin is a fundamental question in the cuprates, with explanations falling into two general categories: preformed Cooper pairs ("one-gap") or a distinct quantum phase from superconductivity ("two gaps"). Understanding the pseudogap is believed to be the key hurdle to developing a microscopic theory to explain cuprate superconductivity.

Finally, two different resistivity regimes are observed. The strange metal regime has T-linear resistivity up to exceedingly high temperature and exists over a broad doping range near optimal doping; Fermi liquid resistivity ($\rho \propto T^2$) is observed at

low temperatures on the overdoped side, usually beyond the superconducting dome [21, 22, 23].

1.2.3 Superconductivity and pseudogap

Much of cuprates research focuses on superconductivity and the pseudogap, so these phases will be discussed in more detail.

Although the mechanism of cuprate superconductivity is debated, there is much agreement about certain aspects of the superconducting state. Several key experiments demonstrated a d-wave form of the superconducting gap, more specifically $d_{x^2-y^2}$, and this order parameter is widely accepted. Phase sensitive tunneling showed that the phase of the order parameter changes sign every 90 degrees [24]. ARPES indicated that the nodes of the gap function lie on the zone diagonal [25]. In some ways, the superconducting state is considered to be unsurprising, other than the d-wave order parameter and the high T_c: there are singlet Cooper pairs and Ginzburg-Landau phenomenology is obeyed in the regime it is applicable. Nevertheless, as we shall see in Chapter 3, other phases coexist with superconductivity below T_c. These other phases strongly affect the spectroscopic properties of the superconducting state, and in that way, superconductivity is not so boring after all. It is a crucial window into other phases which may be involved in promoting or inhibiting superconductivity.

The pseudogap was first observed in NMR and subsequently in many other experimental techniques [20]. There is substantial debate about if T* is a phase transition. In specific heat, there is no jump at T*, and instead, T* marks the temperature where the electronic component of the specific heat starts to decrease [26]. This lack of specific heat signature is used to argue against a phase transition at T*, but it is crucial to revisit those experiments, as sample quality has improved tremendously. In ARPES, the pseudogap manifests as truncated 'Fermi arcs' near nodal momenta (where the Fermi surface intersects the (0,0)-(π,π) line) and gaps which persist at antinodal momenta (near (π,0)) [27]. It should be noted that although the terms 'node' and 'antinode' strictly refer to the superconducting order parameter in the cuprates, those same terms are used to reference general momentum regions in the

Brillouin zone, even in the absence of superconductivity. The gap structure in the pseudogap regime highlights the key difficulty of the cuprates problem. While one might be compelled to formulate a BCS-like theory for the cuprates with a different pairing glue, the lack of a filled Fermi sea just above T_c short circuits that approach. This will be explored in Chapter 5

A full Fermi surface is recovered above T*. At dopings where no pseudogap is observed above T_c, a complete, closed Fermi surface is recovered above T_c.

By the mid-2000s there was accumulating evidence that the psuedogap is a distinct phase from superconductivity, rather than a disordered or fluctuating superconductor. Experimental signatures fall into several categories: 1) a non-superconducting signal which rises in an order-parameter-like fashion below T* (neutron scattering [28], polar Kerr effect [29]) 2) different sign or trend of a signal $T<T^*$ as compared to $T<T_c$ (transient reflectivity [30], Nernst coefficient [31]) 3) Distinct phenomenology in different momentum or temperature regimes (ARPES [32, 33, 34, 35, 36, 37], Raman [38]) 4) Evidence for the pseudogap phase boundary inside the superconducting dome (ARPES [39], transport [40]). The ARPES signatures of two-gap physics are described in chapter 3. This paints a phase diagram similar to other unconventional superconductors where superconductivity appears to emerge around a quantum critical point. As a caveat, there is evidence for the T=0 endpoint of the pseudogap inside the superconducting dome, but on the hole doped side, there has not been definitive proof that this constitutes a true quantum critical point.

1.2.4 Bi-2212

Most of the experiments in this thesis are on $Bi_2Sr_2CaCu_2O_{8+\delta}$ (Bi-2212), which is favored for surface spectroscopies because of its pristine cleaved surfaces. The crystal structure is shown in Fig. 1.6(a), and has a CuO_2 bi-layer as its structural unit. There are thus two Fermi surface sheets, the bonding band and the (higher energy) antibonding band. ARPES experiments are usually configured such that only one band is visible, for simpler data analysis.

Although other cuprates might be cleaner, not other cuprate yields sharper spectra

than Bi-2212 (and its single-layer and tri-layer cousins). Thus, to take full advantage of state-of-the-art spectroscopies and to properly interpret spectroscopy data, Bi-based cuprates are the clear choices. This thesis presents several doping-dependence studies, and Fig. 1.5 shows the doping range in which different chemistries of Bi-2212 can be grown. Intrinsic Bi-2212, where doping is controlled only by oxygen annealing, can only access the near-optimally-doped regime. To produce more overdoped Bi-2212 which is stable, it is usually required to dope Pb on the Bi site. This has the additional effect of reducing or eliminating the incommensurate modulation in the BiO layers which contaminates ARPES spectra. To achieve stable deeply underdoped samples, Ca is substituted with Y or Dy, followed by subsequent oxygen annealing to precisely control T_c. The full consequences of substitutional doping deserve further study. However, alternate methods of underdoping (generally annealing films) yield poorer quality spectra, which suggests that T_c might be diminished because of disorder, not doping.

1.2.5 Approaches to the cuprate problem

This thesis approaches the cuprate problem from two general directions: studying bosons which may be involved in promoting or suppressing superconductivity and studying other phases which exist nearby or with superconductivity on the phase diagram. Of course, these two approaches to the cuprates are related, because quantum phases usually have associated elementary excitations to which electrons might strongly couple.

In BCS superconductors, the electron-phonon mechanism of Cooper pairing has ample experimental support [42, 43]. One line of cuprates research has been to seek out an analogous pairing glue which can produce a high T_c. ARPES can observe evidence of electron-boson coupling via 'kinks' in the band dispersion. One can then attempt to pin down which boson causes the kink via phenomenology (temperature and doping dependence, momentum space structure), comparisons to other experiments, and input from theory. Finally, one must understand whether these bosons cause and/or enhance superconductivity.

Another approach addresses the impediment of a non-Fermi liquid normal state. Originally, this line of research focused on trying to understand what the pseudogap is. However, with evidence that the pseudogap exists even below T_c, the question has been broadened to understanding how superconductivity interacts with the pseudogap and other coexisting phases.

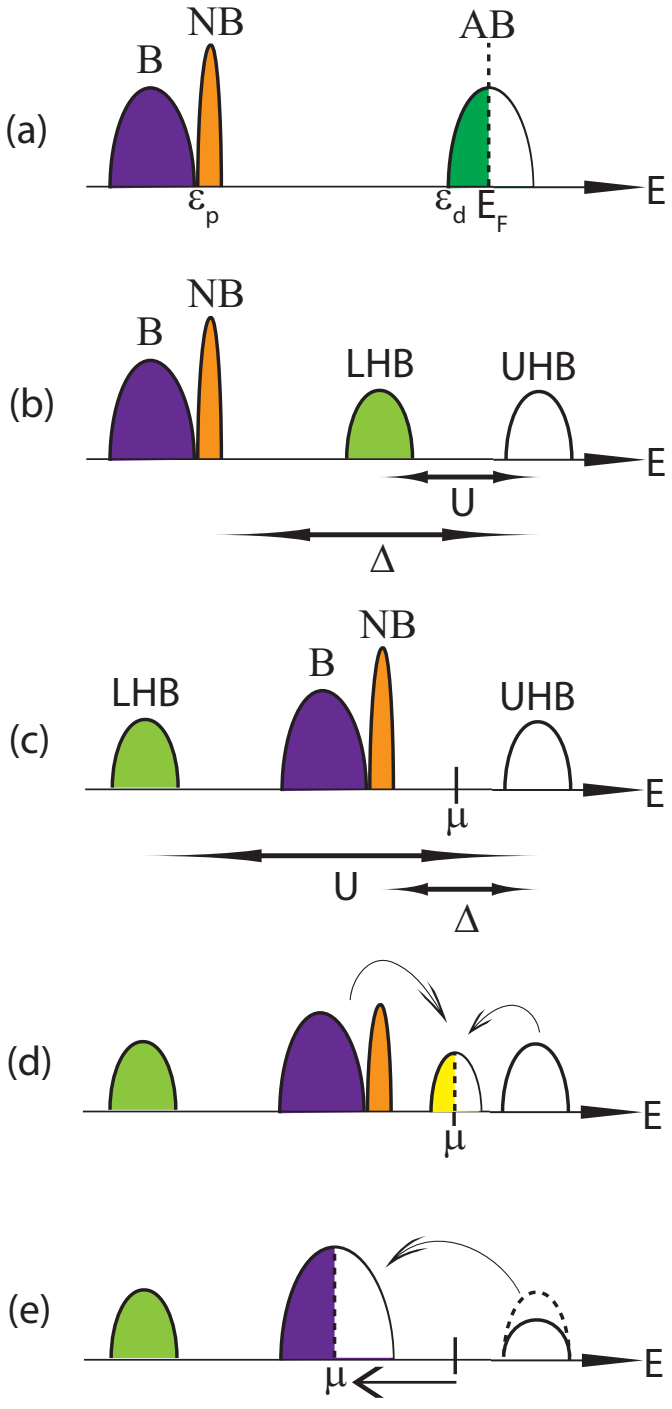

Figure 1.4: (a) Density of states (DOS) in Fig. 1.3(c) for non-correlated case (b) U<Δ (c) U>Δ is more accurate for cuprates. (d)-(e) possibilities for doping charge transfer insulator. (d) μ is pinned inside the charge transfer gap, and metallic states are derived from spectral weight transfer (e) μ shifts with doping and spectral weight is transferred from UHB.

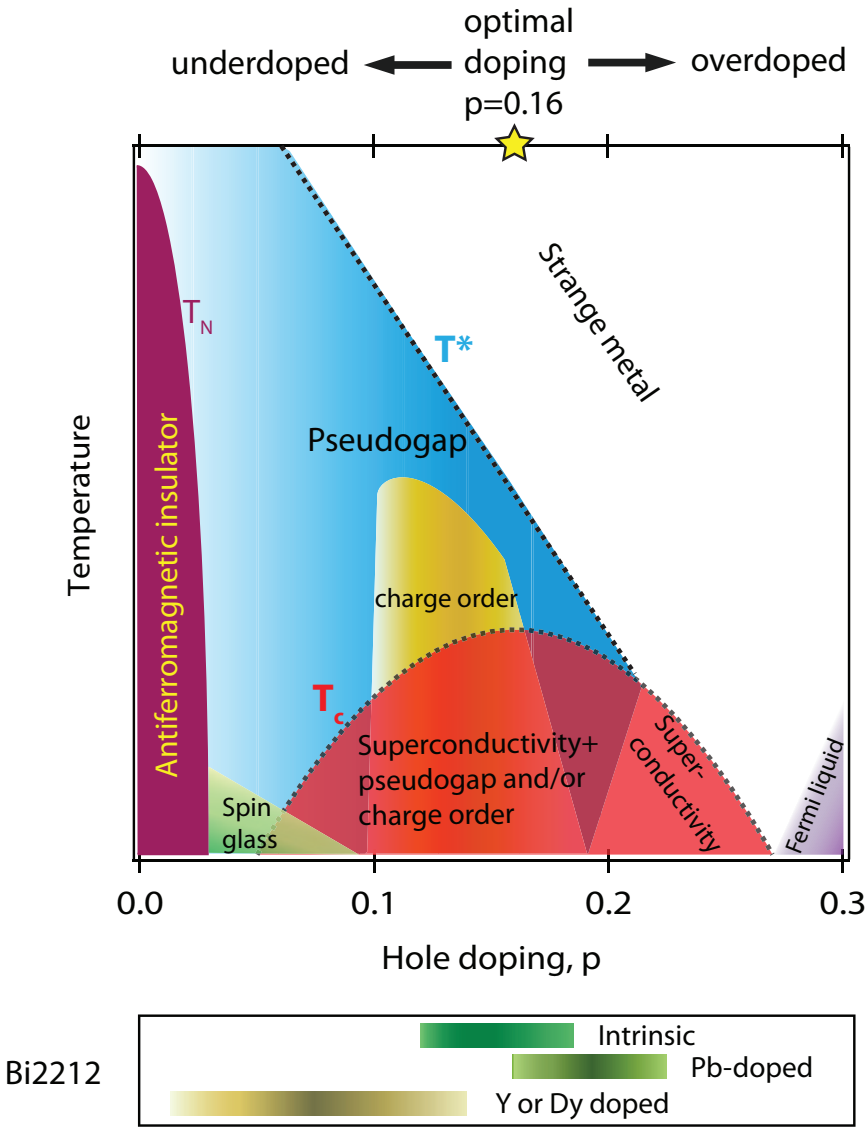

Figure 1.5: Schematic of hole-doped phase diagram in zero magnetic field, illustrating phases that will be encountered in this thesis. Lower panel shows the dopings that can be achieved with different compositions: intrinsic ($Bi_2Sr_2CaCu_2O_{8+\delta}$), Pb-doped ($(Bi,Pb)_2Sr_2CaCu_2O_{8+\delta}$), and Y or Dy doped ($Bi_2Sr_2(Ca,Dy/Y)Cu_2O_{8+\delta}$)

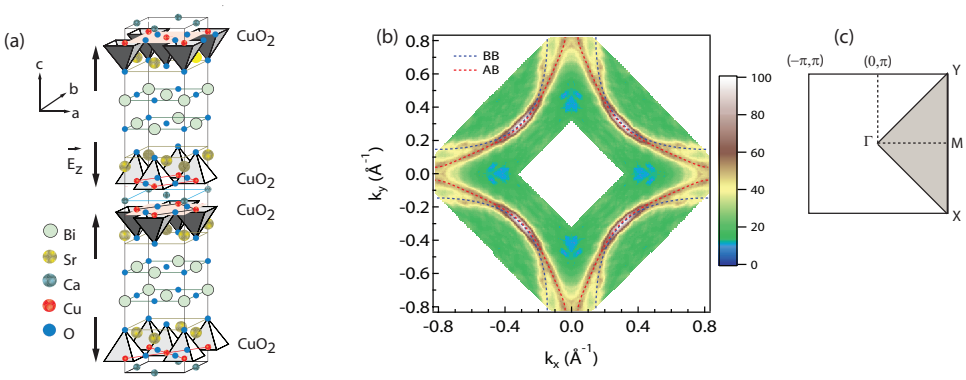

Figure 1.6: (a) crystal structure of $Bi_2Sr_2CaCu_2O_{8+\delta}$ (Bi-2212) from Ref. [41]. (b) Fermi surface mapping of Bi-2212 (OD65) showing bonding (BB) and antibonding (AB) bands. (b) 2D projected Brillouin zone with irreducible unit shaded in grey.

Chapter 2

Laser-based ARPES

2.1 ARPES

2.1.1 Overview

This section gives a broad overview of the angle-resolved photoemission spectroscopy (ARPES) technique, focusing on concepts key to this thesis. Further details as well as a review of ARPES experiments on cuprates prior to 2004 can be found in Ref. [44] and Ref. [45].

Angle resolved photoemission spectroscopy is based on the photoelectric effect. UV light of energy $h\nu$ shines on the sample and photoelectrons are emitted. An analyzer measures the emission angle (ϑ) and kinetic energy (E_{kin}) of these photoelectrons, which is related via energy and momentum conservation to the binding energy (E_B) and crystal momentum ($\mathbf{k}_{||}$) that the electrons had inside the sample.

$$E_{kin} = h\nu - \phi - |E_B| \tag{2.1}$$

$$\mathbf{p}_{||} = \hbar\mathbf{k}_{||} = \sqrt{2mE_{kin}} \cdot \sin\vartheta \tag{2.2}$$

The intensity in an ARPES experiment is given by

$$I(\mathbf{k},\omega) = I_0(\mathbf{k},\nu,\mathbf{A}) f(\omega) A(\mathbf{k},\omega) \otimes R(\Delta\mathbf{k},\Delta\omega) \tag{2.3}$$

where I_0 is a matrix elements term, f(ω) is the Fermi-Dirac cutoff, A(k, ω) is the single particle spectral function, and R(Δk,$\Delta\Omega$) is the resolution. Each of these terms will be discussed in turn, with a focus on how they pertain to topics in this thesis. Data can be sliced in two ways: energy distribution curves (EDCs) and momentum distribution curves (MDCs). The former plots the intensity as a function of energy at fixed momentum, and it is usually used to learn about spectral gaps. The latter plots the intensity as a function of momentum at fixed energy, and it gives information about the band position at each energy.

Matrix elements

ARPES spectra are interpreted in terms of the three step model, where the photoemission process is modeled as three sequential, independent steps: (1) Excitation of an electron in the bulk by incident photon (2) Electron travels to surface (3) emission from sample surface.

The matrix element term is given by

$$I_0(\mathbf{k}, \nu, \mathbf{A}) = |\langle \Psi_f | \mathbf{A} \cdot \mathbf{p} | \Psi_i \rangle|^2 \tag{2.4}$$

Where Ψ_f and Ψ_i are the final and initial many-electron wavefunctions, $\mathbf{p}$ is the electron momentum, and $\mathbf{A}$ is the vector potential of the photon.

Matrix elements can be quantified by symmetry, in the case that the beam and the detector lie in a mirror plane (plane perpendicular to surface of the sample across which there is reflection symmetry). A-priori knowledge of the orbital character of the final states can be used to construct experiments which highlight certain bands or Fermi surface regions [45] and experimental geometry can be configured to clarify the orbital character of band seen experimentally [46, 47].

Matrix elements sometimes have the practical effect of selectively suppressing bands. In Bi-2212, photon energy is chosen to individually select either the bonding or antibonding band such that experiments are easier to interpret. As two examples, 7 eV selects the antibonding band [48] and 22.7 eV is used to select the bonding band in ΓM cut geometry near optimal doping.

Fermi-Dirac cutoff

The Fermi-Dirac function, f(ω)=(1+e$^{\omega/k_BT}$)$^{-1}$, truncates the ARPES spectrum such that only the occupied states are accessible at low temperature. At higher temperature, there is more thermal population above the Fermi level, and information can be gleaned about unoccupied states provided sufficient care is taken to correct for detector nonlinearity and beamline diffraction artifacts.

A number of methods are used to remove the Fermi-Dirac cutoff during data analysis. If particle-hole symmetry is obeyed, as it is at k$_F$ in a metal or conventional superconductor, symmetrization removes the Fermi function. The symmetrized EDC is given by the following expression

$$A(\mathbf{k}_F,\omega)f(\omega) + A(\mathbf{k}_F,-\omega)f(-\omega) = A(\mathbf{k}_F,\omega) \tag{2.5}$$

More generally, one can divide by the Fermi function convolved with the energy resolution.

$$A(\mathbf{k}_F,\omega) \otimes R(\Delta k,\Delta\omega) \approx \frac{A(\mathbf{k}_F,\omega) \otimes R(\Delta k,\Delta\omega)}{f(\omega) \otimes R(\Delta\omega)} \tag{2.6}$$

This is not exact, since the commutation operation is not distributive, but the discrepancy is not too large at higher temperature.

Single particle spectral function

The effects of interactions are captured by the single-particle spectral function, which is the microscopic quantity measured by ARPES

$$A(\mathbf{k},\omega) = -\frac{1}{\pi}\frac{\Sigma"(\mathbf{k},\omega)}{(\omega-\epsilon_{\mathbf{k}}-\Sigma'(\mathbf{k},\omega))^2-(\Sigma"(\mathbf{k},\omega))^2} \tag{2.7}$$

whose expression contains the bare band dispersion ($\epsilon_{\mathbf{k}}$) and the self energy $\Sigma(\mathbf{k},\omega)$=$\Sigma$'($\mathbf{k}$,$\omega$)+$i\Sigma$"($\mathbf{k}$,$\omega$). $\epsilon_{\mathbf{k}}$ is the bare band dispersion, which is usually not known a-priori. Σ'($\mathbf{k}$,ω) renormalizes the bare band dispersion and Σ"($\mathbf{k}$,ω) is related to the scattering rate. For example, in the case of a Fermi liquid, the self energy is given by

$$\Sigma_{FL}(\omega) = \alpha\omega + i\beta[\omega^2 + (\pi k_B T)^2] \tag{2.8}$$

where the well known T^2 contribution to electrical resistivity is apparent in the imaginary part.

For most analysis, it is assumed that $\Sigma(\mathbf{k},\omega)$ is very weakly $\mathbf{k}$-dependent, such that for each energy, $A(\mathbf{k},\omega)$ follows a Lorentzian lineshape. This is supported by experiments on many compounds showing Lorentzian MDCs [44]. Self energies will be explored in terms of mode coupling in subsequent Chapters 6 and 7, and Appendix B.

Resolution

The first three terms in Eqn. 2.3 are convolved with a resolution ellipsoid with gaussian energy widths $\Delta\omega$ and momentum width $\Delta\mathbf{k}$. The momentum resolution function is usually taken to be a gaussian, but a 'window' function is also sometimes used [49]. The momentum resolution is set by the angular resolution of the analyzer and the photon energy of the experiment via Eqn. 2.1.

$$\hbar\Delta\mathbf{k} = \sqrt{2mE_{kin}} \cdot \cos\vartheta\Delta\vartheta \tag{2.9}$$

The SES 2002 analyzer used in laser ARPES experiments in this thesis has an angular resolution ($\Delta\vartheta$) of 0.2°, and the R4000 analyzer used for synchrotron experiments has an angular resolution of 0.3° in wide angle mode (±15°). At normal incidence, this corresponds to momentum resolutions of 0.009 $\mathring{A}^{-1}$ for 7eV photons and 0.036 $\mathring{A}^{-1}$ for 22.7eV photons.

The energy resolution is affected by the bandwidth of the lightsource, the energy resolution of the analyzer, and the electronics. In synchrotron experiments, a band of photon energies is chosen by rotating a diffraction grating relative to a 'white' UV beam and the energy width of this band is adjusting by narrowing down beamline slits. Thus, there is a tradeoff between photon counts and energy resolution.

Photoemitted electrons enter the analyzer via a slit, and there is an additional component of momentum resolution perpendicular to this analyzer slit which serves

to 'integrate' ideal 1-dimensional cuts over a finite momentum window.

2.2 7eV laser

Laser ARPES uses a quasi-continuous wave UV laser, usually in the energy range 6-7 eV as a narrow bandwidth lightsource, with VUV wavelengths typically achieved by by higher harmonic generation (HHG) in nonlinear crystals. $KBe_2BO_3F_2$ (KBBF) is the nonlinear crystal which can produce the shortest wavelength UV light [50, 51], and it is used in the generation of 7 eV for laser ARPES. 7 eV laser ARPES has been demonstrated with total experimental resolution below 1 meV [52].

For the work in this thesis, 7 eV (177.3 nm) laser light is produced by frequency doubling of light from a 3.5 eV (354.7) laser (Coherent, Palladin) with a KBBF device. The 3.5 eV laser represents a frequency-tripling of a Nd:YAG oscillator (1064 nm). This section will give an overview of the nonlinear optics (NLO) principles which are key to the operation of the 7 eV laser in the Shen lab and describe they key optical elements in the setup. A good introductory text for the topic is *Nonlinear Optics* by Robert Boyd [53], and much of the following section follows the treatment given in that text.

2.2.1 Second harmonic generation

The electric polarization (P(t)), in a medium can generally be expressed in terms of the susceptibility ($\chi^{(n)}$) and the electric field (E(t)).

$$P(t) = \chi^{(1)}E(t) + \chi^{(2)}E^2(t) + \chi^{(3)}E^3(t) + ... \tag{2.10}$$

$\chi^{(1)}$ is the linear susceptibility. The higher order terms in Eqn. 2.10 give rise to nonlinear optics which makes second harmonic generation possible. The second order susceptibility is only nonzero in media without inversion symmetry.

Consider a time-varying electric field of the form

$$E(t) = Ee^{i\omega t} + c.c. \tag{2.11}$$

where ω is the frequency. The quadratic term of the polarization is then given by:

$$P^{(2)}(t) = \chi^{(2)}E^2(t) \tag{2.12}$$
$$= \chi^{(2)}[Ee^{-i\omega t} + E^*e^{i\omega t}]^2 \tag{2.13}$$
$$= 2\chi^{(2)}EE^* + \chi^{(2)}[E^2e^{-2i\omega t} + c.c.] \tag{2.14}$$

The first term does not generate electromagnetic radiation. The second term contains an electric field with a frequency double the original. This logic can be easily extended to a system with multiple frequencies to produce sum and difference frequencies.

$$E(t) = E_1e^{i\omega_1 t} + E_2e^{i\omega_2 t} + E_3 2e^{i\omega_3 t} + ... + c.c. \tag{2.15}$$

2.2.2 Phase matching

Eqn. 2.12 is that of a time varying polarization, which can act as a source for electromagnetic fields. In a real material, there will be many sources, as atoms will develop an oscillating dipole moment under influence of the time-varying polarization. For useful generation of higher harmonics, the relative phases of the radiation from each dipole need to add constructively in the forward direction. Thus, the derivations in this section consider the spatial components of electric field too.

Assume that each component of the electric field obeys the driven wave equation in NLO media,

$$\nabla^2 E - \frac{n^2}{c^2}\frac{\partial^2 E}{\partial t^2} = \frac{4\pi}{c^2}\frac{\partial^2 P^{NL}}{\partial t^2} \tag{2.16}$$

where n is the refractive index and P^{NL}, is the nonlinear component of polarization. In general, n is frequency dependent, so each frequency component of the electric field must be considered separately.

$$E(r,t) = \sum_n E_n(r,t) = \sum_n [E_n(r)e^{-i\omega t} + c.c.] \tag{2.17}$$

Eqn. 2.16 holds for each of the frequency components of the electric field. For the

case of second harmonic generation, there are two components: ω and 2ω. Considering propagation only in the z-direction, the electric field is given by

$$E_\omega = A_\omega(z)e^{i(k_\omega z-\omega t)} + c.c. \tag{2.18}$$
$$E_{2\omega} = A_{2\omega}(z)e^{i(k_{2\omega} z-2\omega t)} + c.c. \tag{2.19}$$

where $A_\omega(z)$ and $A_{2\omega}(z)$ are amplitudes which vary slowly with z. k is the wave number, where $k_\omega = n_\omega\omega/c$. The nonlinear component of polarization in Eqn. 2.16 is given by:

$$P^{NL} = \chi^{(2)}[A_\omega e^{i(k_\omega z-\omega t)} + A_{2\omega}e^{i(k_{2\omega} z-2\omega t)}]^2 + c.c. \tag{2.20}$$
$$= \chi^{(2)}[A_\omega^2 e^{2i(k_\omega z-\omega t)} + 2A_{2\omega}A_\omega^* e^{i(k_{2\omega} z-k_\omega-\omega t)} + c.c. + \text{higher order terms}] \tag{2.21}$$

Now we plug Eqns. 2.18 and 2.20 into the driven wave equations separately for each frequency component. Since we are only considering the z-direction, ∇^2 is replaced by d^2/dz^2. At this point, the explicit reference to the complex conjugate is also dropped.

$$\frac{d^2A_{2\omega}}{dz^2} + 2ik_{2\omega}\frac{dA_{2\omega}}{dz} = -e^{i(2k_\omega-k_{2\omega})z}\frac{16\pi\omega^2}{c^2}\chi^{(2)}A_\omega^2 \tag{2.22}$$
$$\frac{d^2A_{\omega}}{dz^2} + 2ik_{\omega}\frac{dA_{2\omega}}{dz} = -e^{i(-2k_\omega+k_{2\omega})z}\frac{8\pi\omega^2}{c^2}\chi^{(2)}A_{2\omega}A_\omega^* \tag{2.23}$$

In the slow-varying-amplitude approximation, the first term in each equation is dropped, and we are left with the following coupled equations

$$\frac{dA_{2\omega}}{dz} = e^{i\Delta kz}\frac{8i\pi\omega^2}{k_{2\omega}c^2}\chi^{(2)}A_\omega^2 \tag{2.24}$$
$$\frac{dA_{2\omega}}{dz} = e^{-i\Delta kz}\frac{4i\pi\omega^2}{k_{\omega}c^2}\chi^{(2)}A_{2\omega}A_\omega^* \tag{2.25}$$

where the phase mismatch Δk is given by

$$\Delta k = 2k_\omega - k_{2\omega} \tag{2.26}$$

A common approximation is that A_ω is constant, and in this case, the amplitude of the second harmonic a distance L from the origin is given by integrating both sides of Eqn. 2.24.

$$\int_0^L \frac{dA_{2\omega}}{dz} = \frac{8\pi\omega^2}{k_{2\omega}c^2\Delta k}\chi^{(2)}A_\omega^2[e^{i\Delta kL} - 1] \tag{2.27}$$

The intensity (I) of a beam is given by the electric field squared, which is proportional to $A_{2\omega}$.

$$I \propto |A_{2\omega}|^2 \propto \frac{L^2}{(\Delta k)^2}(e^{i\Delta kL}-1)(e^{-i\Delta kL}-1) = \frac{L^2\sin^2(\frac{\Delta kL}{2})}{(\Delta kL/2)^2} = L^2 sinc^2(\Delta kL/2) \tag{2.28}$$

The sinc function is strongly peaked at zero, indicating that the second harmonic intensity is maximized when Δk=0. This is the phase matching condition. Expressing this in terms of indices of refraction gives

$$\Delta k = 2n_\omega\omega - 2n_{2\omega}\omega = 0 \tag{2.29}$$

Generally, materials have dispersion and $n_\omega \neq n_{2\omega}$. However, a solution to Eqn. 2.29 can be found in a birefringent crystal where the indices of refraction are different along different crystallographic axes. By adjusting the angle of the nonlinear crystal (angle tuning) relative to the polarizations of the fundamental and second harmonic, one can achieve the phase matching condition in Eqn. 2.29. The details below are after Refs. [53] and [54].

The wave equation in a dielectric medium is given by

$$\nabla \times \nabla \times \mathbf{E} + \frac{1}{c^2}\frac{\partial^2\mathbf{E}}{\partial t^2} = -\frac{1}{c^2}\sqrt{\mathbf{n^2 - 1}}\frac{\partial^2 E}{\partial t^2} \tag{2.30}$$

Where $\mathbf{n}$ is a diagonal 3×3 matrix for the refractive index along 3 crystallographic

axes.

$$\mathbf{n} = \begin{pmatrix} n_1 & 0 & 0 \\ 0 & n_2 & 0 \\ 0 & 0 & n_3 \end{pmatrix} \tag{2.31}$$

Usually uniaxial materials are used for second harmonic generation. Uniaxial crystals have two axes of equal index of refraction and one that is unequal.

$$\mathbf{n_{uniaxial}} = \begin{pmatrix} n_o & 0 & 0 \\ 0 & n_e & 0 \\ 0 & 0 & n_o \end{pmatrix} \tag{2.32}$$

The subscripts refer to the ordinary (o) and extraordinary (e) axes.

Eqn. 2.30 has plane wave solutions $e^{i(\mathbf{k}\cdot\mathbf{r}-\omega t)}$ where the wavevector $\mathbf{k}$ satisfies

$$\mathbf{k}\times\mathbf{k}\times\mathbf{E} + \frac{\omega^2}{c^2}\mathbf{E} = -\frac{\omega^2}{c^2}\sqrt{\mathbf{n^2}-\mathbf{1}}\mathbf{E} \tag{2.33}$$

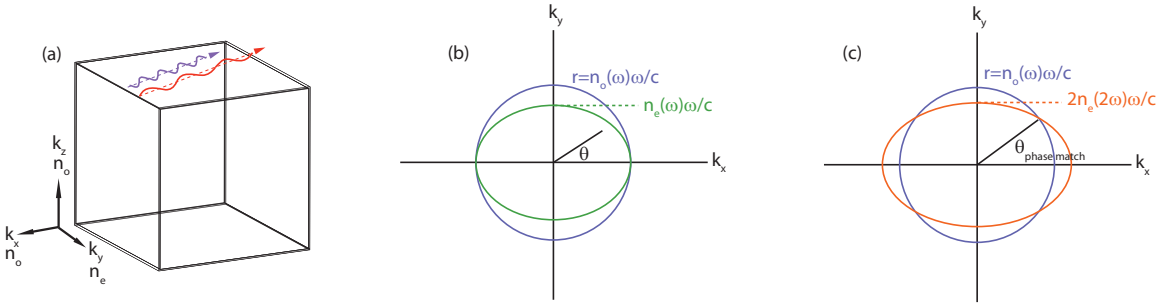

Figure 2.1: (a) sketch of a uniaxial birefringent crystal. beams propagate in k_x-k_y plane. (b) Index of refraction as a function of planar angle (θ) for light of frequency ω polarized along the ordinary direction (purple circle) and extraordinary direction (green ellipse). (c) Index of refraction for light of frequency ω polarized along the ordinary direction (purple circle) and light of frequency 2ω polarized along extraordinary direction (orange ellipse). Their intersection gives the phase matching angle, $\theta_{phasematch}$

This can also be expressed in matrix form, $\mathbf{M}\cdot\mathbf{E}$=0, and the equation has a solution

if the determinant of $\mathbf{M}$ is zero.

$$\mathbf{M} = \begin{pmatrix} (n_o\omega/c)^2 - k_y^2 - k_z^2 & k_x k_y & k_x k_z \\ k_y k_x & (n_e\omega/c)^2 - k_x^2 - k_z^2 & k_y k_z \\ k_z k_x & k_z k_y & (n_o\omega/c)^2 - k_x^2 - k_y^2 \end{pmatrix} \tag{2.34}$$

Now consider only the k_x-k_y plane such that k_z=0. The determinant of $\mathbf{M}$ is zero if either or both of the following two expressions holds:

$$k_x^2 + k_y^2 = (n_o\omega/c)^2 \tag{2.35}$$

$$\frac{k_x^2}{(n_e\omega/c)^2} + \frac{k_y^2}{(n_o\omega/c)^2} = 1 \tag{2.36}$$

These are equations for a circle and an ellipse as illustrated in Fig. 2.1(b). This figure illustrates the indices of refraction as a function of angle in the k_x-k_y plane. We are assuming a negative uniaxial crystal where $n_o > n_e$ The circle is for a beam of frequency ω polarized in the ordinary direction and the ellipse is for a beam of frequency ω polarized in the extraordinary direction. Next, we consider a beam of frequency 2ω polarized in the extraordinary direction (Fig. 2.1(c)). The equation for the index of refraction ellipse is given by

$$\frac{k_x^2}{4(n_e(2\omega)\omega/c)^2} + \frac{k_y^2}{4(n_o(2\omega)\omega/c)^2} = 1 \tag{2.37}$$

Note the explicit indication that n_o and n_e are functions of frequency. Assuming the fundamental is polarized along the ordinary direction and the second harmonic is polarized along the extraordinary direction, the points where the circle and the ellipse intersect in Fig. 2.1(c) marks the phase matching angle. This is the angle where the fundamental and second harmonic have the same index of refraction such that Eqn. 2.29 is satisfied. This angle is given by:

$$\sin^2(\theta) = \frac{n_e^2(2\omega)[n_o^2(2\omega) - n_o^2(\omega)]}{n_o^2(\omega)[n_o^2(2\omega) - n_e^2(2\omega)]} \tag{2.38}$$

2.2.3 Prism coupled KBBF-device

The refractive indices of KBBF are given in Ref. [55] and they determine the phase matching angle.

$$n_o(354.7nm) = 1.4932 \tag{2.39}$$

$$n_o(177.3nm) = 1.5681 \tag{2.40}$$

$$n_e(177.3nm) = 1.4800 \tag{2.41}$$

$$\theta = 66.3^\circ \tag{2.42}$$

KBBF is a very flaky material which cannot be cut at the phase matching angle. Thus, a prism-coupled device is used to ensure that light enters the KBBF at the phase matching angle [56, 51]. The device, sketched in Fig. 2.2(a) consists of a plate-like piece of KBBF crystal sandwiched between two CaF_2 prisms. CaF_2 is chosen because it has a similar index of refraction as KBBF at 177nm, thus minimizing losses at the interface. The KBBF and the faces of the prism are highly polished in order to achieve optical contact, and light pressure is applied via mechanical clamp in order to maintain contact (Fig. 2.2(b)). The incidence angle of the 354.7nm light is adjusted such that it enters the KBBF at the phase matching angle ($n_{354.7nm}$ (CaF_2)=1.446). Thus, for prisms having the phase matching angle, the 354.7 nm light will not be incident normal to the prism. The fundamental and second harmonic exit the prism at different angles. For the geometry shown in Fig. 2.2 (a), they are 6.8° apart.

Thicker KBBF crystals tend to have higher second harmonic generation efficiency [56]. We have built and tested two KBBF prism-coupled devices. The thicker one capable of generation more 7eV power has been used for more than five years with no catastrophic degradation. A measurement of the 7eV power generation as a function of 3.5 eV power for both devices is shown in Fig. 2.3. We note that this varies somewhat when the laser ARPES system is re-aligned, as different spots on the KBBF crystal may differ in optical quality and optical contact with the CaF_2 prisms. Conversion efficiencies up to 0.1% have been achieved with our KBBF devices.

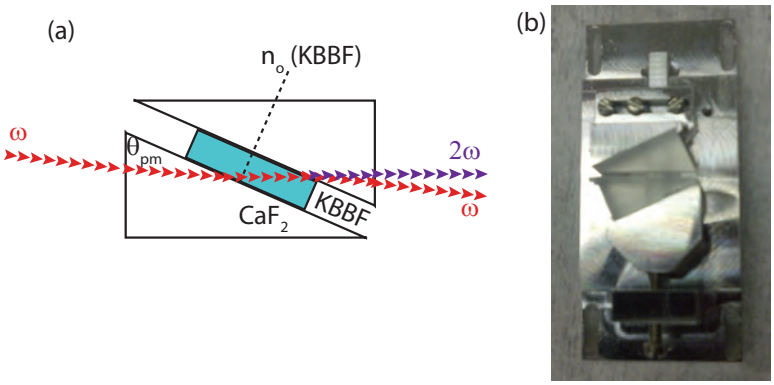

Figure 2.2: (a) Schematic of prism coupled device, consisting of KBBF sandwiched between two CaF_2 right-angle prisms with one of the angles being the phase matching angle (θ_{pm}). Dashed line indicates extraordinary direction in KBBF. (b) Photograph of prism coupled device used in laser ARPES experiments in this thesis.

2.2.4 Laser ARPES system

A schematic of the optics setup is shown in Fig. 2.4. At the entrance, a rotating polarizer is used to control the 3.5 eV power and a lens is used to focus the beam onto the KBBF. The KBBF device sits on a 3-axis translation stage, and this is used to find the portion of the KBBF with the highest transmission. Then, the KBBF device is rotated such that the 3.5 eV light enters the KBBF at the phase matching angle. The 3.5 eV fundamental and 7 eV second harmonic exit the KBBF device at different angles, and they are directed in opposite directions by turning mirrors. The 7 eV light is sent through a quarter wave plate which can be rotated to adjust the polarization from linear to right-hand circularly-polarized to left-hand circularly polarized and elliptical polarizations in between. The 7eV beam is initially polarized in plane, orthogonal to the incoming 3.5 eV. The quarter wave plate can be replaced with a half wave plate in order to rotate the linear polarization. A phototube (Hamamatsu) is used to measure the 7eV power, and it is flipped out of the beam path when not in use. It has a coating to reject the 3.5 eV light, which is important because there is plenty of diffuse and specular scatter. Finally, a lens is used to focus the 7eV light onto the ARPES sample.

The optics are enclosed in a chamber which is purged with nitrogen, because 7eV

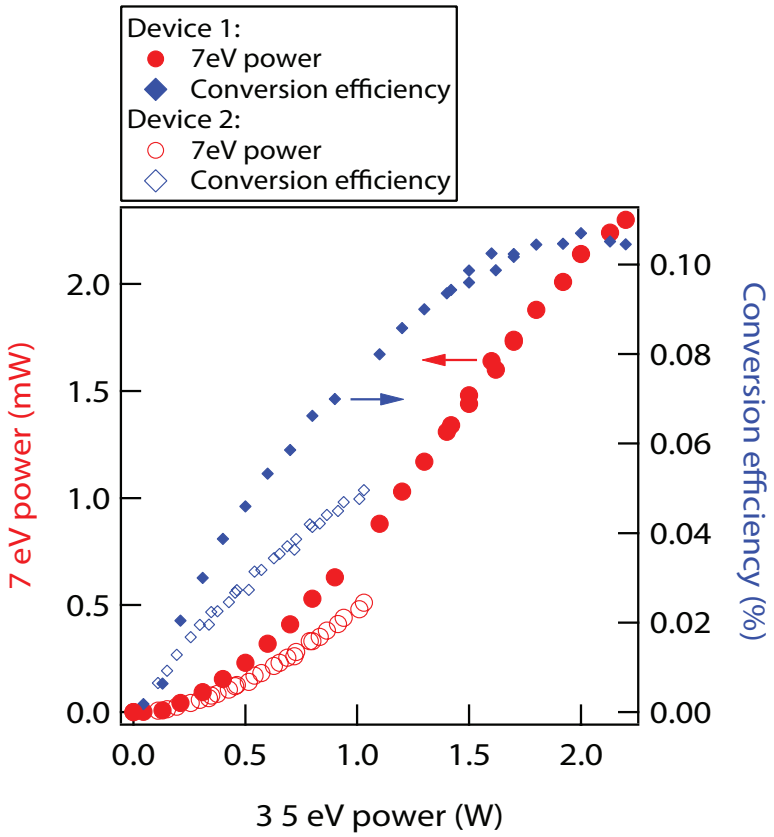

Figure 2.3: 7 eV power generated as a function of 3.5 eV power (red) and efficiency of second harmonic generation (blue) for two KBBF devices. The one with higher 7 eV power generation was used for experiments in this thesis.

is readily suppressed by oxygen and water. A MgF_2 window is used to transmit the beam into the ARPES chamber. Typical experiments are performed with 10-20μWatts of 7eV.

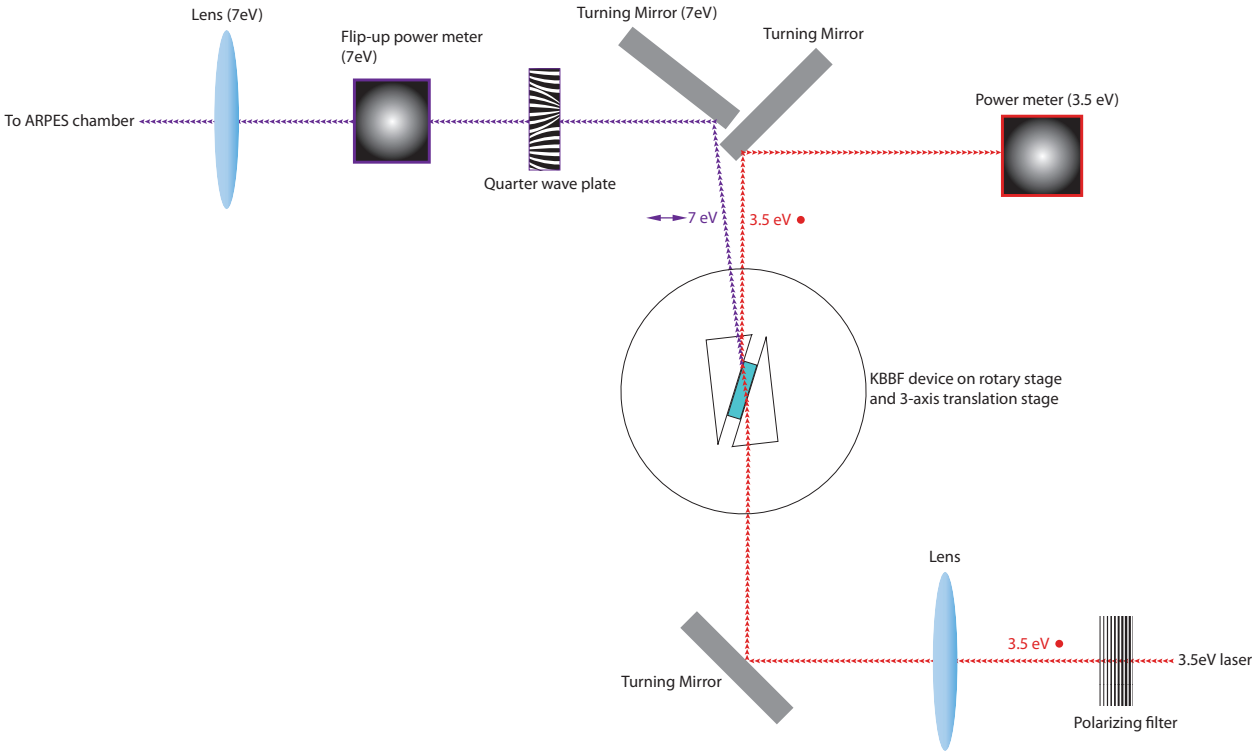

Figure 2.4: Schematic of 7eV laser optics, not to scale. 3.5 eV beam is polarized out of plane, and 7eV beam is polarized in plane.

Chapter 3

Phase competition in trisected superconducting dome

The enhanced photon flux in laser ARPES allows for more efficient data acquisition than traditional synchrotron-based ARPES. This allows to investigate more momenta and temperatures during an experiment before samples age (usually 24-48 hours for cuprates). We have used this advantage to perform the most comprehensive study of spectral gaps in Bi-2212 to date, exploring every variable available to ARPES: temperature, doping, and momentum dependence. The superior energy and momentum resolution of laser ARPES gives unprecedented access to the near-nodal region where gaps are smallest and the lowest lying excitations relevant to ground state properties exist. Understanding the subtle temperature dependence of gaps near and across T_c allows us to formulate a picture of how superconductivity and the pseudogap compete in a momentum-dependent manner. The laser ARPES data are supplemented with synchrotron ARPES data to give a full momentum-space picture, which allows us to propose a revised diagram. All of the temperatures and dopings that were studied are shown in Fig. 3.1. This research is published in Ref. [39].

3.1 Introduction

The momentum-resolved nature of ARPES makes it a key probe of the cuprates whose emergent phases have anisotropic momentum-space structure [25, 27, 57, 58]: both the *d*-wave superconducting gap and the pseudogap have a maximum at the antinode (AN, near (π,0)) and are ungapped at the node, though the latter phase also exhibits an extended ungapped arc [32, 59, 60, 61]. Ordering phenomena often result in gapping of the quasiparticle spectrum, and while ARPES does not always directly reveal the origin of spectral gaps, such information can be inferred from characteristic temperature, doping, and momentum dependence of gaps arising distinct quantum states. This was demonstrated by recent ARPES experiments that argued that the pseudogap is a distinct phase from superconductivity based on their unique phenomenology [32, 33, 34, 35, 36, 37, 62]: the pseudogap dominates near the antinode (AN) [32, 35], and its magnitude increases with underdoping [35, 36], whereas near-nodal (NN) gaps can be attributed to superconductivity and close at T_c [32, 36]. Previous measurements focused on AN or intermediate (IM) momenta, but laser-ARPES, with its superior resolution and enhanced statistics, allows for precise gap measurements near the node where gaps are smallest. This work is unique in its attention to NN momenta using laser-ARPES, and it demonstrates, via a single technique, that three distinct quantum phases manifest in different NN phenomenology as a function of doping.

3.2 Samples

The composition and experimental setup (temperature, photon energy, cut geometry) for the low temperature portion of the study is shown in Table 6.1. All of the dopings and temperatures investigated are summarized in Fig. 3.1.

Table 3.1: ΓY refers to cuts taken parallel to the (0,0)-(π,π) line and ΓM refers to cuts taken parallel to (π,0)-(π,π). Dopings determined from T_c via an empirical curve, T_c=$T_{c,max}$*[1-82.6(p-0.16)^2], taking 96K as the optimum T_c for Bi-2212 [63].

Sample	Composition	Temperature (Fig. 3.3)	Experiment
UD22	$Bi_2Sr_2(Ca,Dy)Cu_2O_{8+\delta}$	10	7eV, ΓY
UD34	$Bi_2Sr_2(Ca,Dy)Cu_2O_{8+\delta}$	11	7eV, ΓY
UD40	$Bi_2Sr_2(Ca,Dy/Y)Cu_2O_{8+\delta}$	12	7eV, ΓY; 19eV, ΓY
UD50	$Bi_2Sr_2(Ca,Y)Cu_2O_{8+\delta}$	10	19eV, ΓY
UD55	$Bi_2Sr_2(Ca,Dy)Cu_2O_{8+\delta}$	11	7eV, ΓY
UD65	$Bi_{2+x}Sr_{2-x}CaCu_2O_{8+\delta}$	12	7eV, ΓY
UD75	$Bi_2Sr_2CaCu_2O_{8+\delta}$	10	22.7eV, ΓM
UD83	$Bi_2Sr_2CaCu_2O_{8+\delta}$	13	7eV, ΓY
UD85	$Bi_2Sr_2CaCu_2O_{8+\delta}$	13	22.7eV, ΓM
UD92	$Bi_2Sr_2CaCu_2O_{8+\delta}$	10	7eV, ΓY; 22.7eV, ΓM
OP96	$Bi_2Sr_2(Ca,Y)Cu_2O_{8+\delta}$	10	21.2eV, ΓY
OP98	$(Bi,Pb)_2Sr_2CaCu_2O_{8+\delta}$	30	18.4eV, ΓM
OD92	$(Bi,Pb)_2Sr_2CaCu_2O_{8+\delta}$	10	18.4eV, ΓY
OD86	$Bi_2Sr_2CaCu_2O_{8+\delta}$	18	22.7eV, ΓM
OD80	$(Bi,Pb)_2Sr_2CaCu_2O_{8+\delta}$	12,30	7eV, ΓY; 18.4eV, ΓM
OD71	$(Bi,Pb)_2Sr_2CaCu_2O_{8+\delta}$	30	18.4eV, ΓM
OD65	$(Bi,Pb)_2Sr_2CaCu_2O_{8+\delta}$	10, 18	7eV, 21.2eV, ΓY

3.3 Results

The energy gap in energy distribution curves (EDCs) can be quantified by several metrics: the position of the leading edge midpoint (LEM) relative to E_F, the energy positions of a quasiparticle peak, or by fitting data to an assumed model. The first two methods do not take the lineshape into account, and are less suitable for comparing gaps among samples with different dopings. Thus, we determined the gap at each cut by fitting symmetrized EDCs at the Fermi wavevector, k_F, to a minimal model proposed by Norman *et al.* [64], $\Sigma(\mathbf{k}, \omega)$=-$i\Gamma_1$+ $\Delta^2/[(\omega+i0^+) + \epsilon(\mathbf{k})]$, where Γ_1 is taken to be a single particle scattering rate, $\epsilon(\mathbf{k})$ is the dispersion, and the gap, Δ, is the quantity of interest in the fitting. It is assumed that $\epsilon(\mathbf{k}_F)$=0, and k_F is defined by the minimum gap locus. A quadratic background was also included to fully account for the lineshape in the deeply underdoped regime or at momenta far from the node. This fitting is applicable to our data as long as a peak is visible in the EDC. Fig. 3.2,

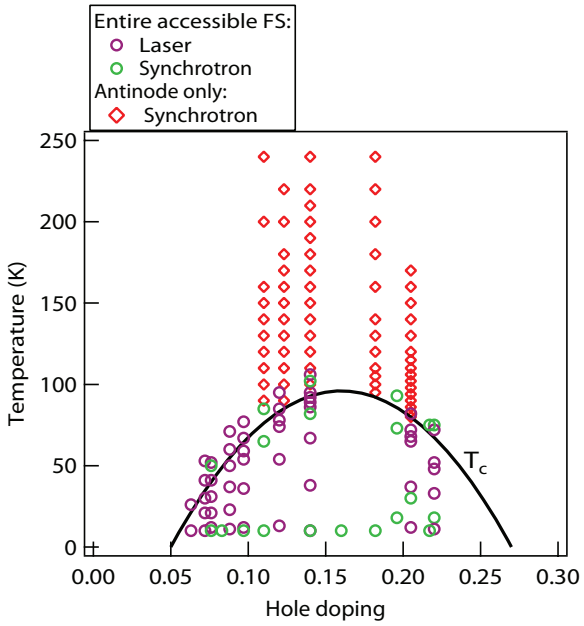

Figure 3.1: Summary of samples and temperatures studied for this thesis chapter and Ref. [39]. Circles: momentum-dependence study; diamonds: antinode only.

shows the low energy portion (ω<110meV) of symmetrized EDCs at low temperature together with fits. In laser ARPES data, EDC peaks become smaller away from the node, which is not intrinsic for most dopings. Synchrotron data taken at higher photoenergy with cuts parallel to ΓM do not show such a substantial decrease in peak intensity [65, 66], with the exception of deeply underdoped samples (p<0.09). The intensity of the quasiparticle peak relative to the higher energy part of the spectrum is also generally not intrinsic, but comparisons between different dopings can be made if experimental conditions (photon energy, polarization, cut geometry) are identical. EDC peaks become smaller and broader with decreasing doping, a correlation and disorder effect, as widely reported [67], and the Norman model provides a good and stable fit to all data throughout the doping range, even though it is a minimal model and does not capture the full physics of the system.

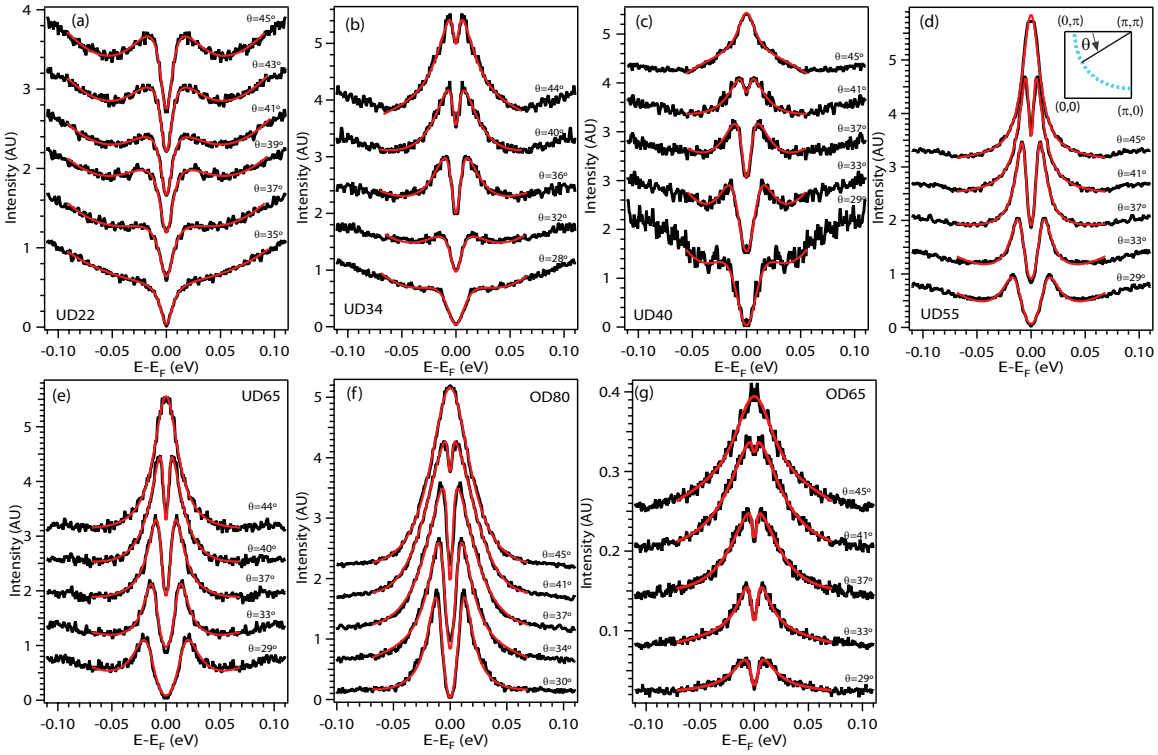

Figure 3.2: Selected symmetrized EDCs at low temperatures with fits. All data taken with 7eV laser and cuts parallel to ΓY.

3.3.1 Low Temperature

Near-nodal region

Fig. 3.3(a)-(c) shows gaps around the Fermi surface in terms of the simple d-wave form, $0.5|\cos(k_x)-\cos(k_y)|$, measured near 10K for the samples in the study. These data are quantified by the gap slope, v_Δ, which measures how fast the d-wave gap increases as a function of momentum away from the node. We find that the low-temperature v_Δ changes suddenly at two dopings, p=0.076 and p=0.19, which are marked in the energy-doping phase diagram in Fig. 3.3(d), dividing the superconducting dome into three regions, labeled **A**, **B**, and **C**. In a d-wave superconductor, v_Δ is expected to scale with T_c, and in region **C** (p>0.19, Fig. 3.3(c)), v_Δ and T_c indeed decrease together. Region **B** ($0.076 \leq p \leq 0.19$), exhibits a markedly different behavior: NN gaps are almost coincident over a large portion of the Fermi surface for

all samples shown in Fig. 3.3(b1-b2), indicating a doping-*independent* v_Δ, despite T_c varying by more than a factor of two. The laser-ARPES gap functions show a slight curvature, nearly identical for all dopings, which is not visible in synchrotron-ARPES data (Fig. 3.4), due to poorer resolution and a sparser sampling of momenta. We note that the crossover between regions **B** and **C** is very abrupt, as v_Δ decreases by almost 25% for a change in doping $\Delta p=0.01$, after having been constant within error bars for $\Delta p=0.12$. In addition, it appears that the gap function also changes at the same doping, as the slight curvature in gap function observed in 3.3(b1) is not observed in region **C**.

There is also a very abrupt transition between regions **A** and **B** at p=0.076 (Fig. 3.3(a)), as region **A** exhibits a gap at every Fermi surface momentum and there is no node where the gap is identically zero. The gap minimum (Δ_{node}) is at the nodal momentum (along (0,0) - (π,π)) and increases with underdoping. Though v_Δ is no longer defined, the gap is anisotropic around the Fermi surface, so we define a gap anisotropy parameter, v_A, from the slope of the gap as a function of momentum. In region **A**, v_A decreases with underdoping. The low-temperature NN energy scales which characterize each of the three phase regions are summarized in Fig. 3.3(d). These findings are an important refinement to previous results which indicated that the NN region is dominated by superconductivity. They demonstrate more conventional *d*-wave superconductivity in region **C**, unconventional doping-independent *d*-wave superconductivity in region **B**, and a nodeless unconventional superconductivity in region **A**.

Near-antinodal region

Figure 3.5 shows the doping dependence of the antinodal gap, Δ_{AN}, for $0.076<p<0.22$, plotted together with v_Δ and v_A. Δ_{AN} is extracted by fitting the energy position of the superconducting quasiparticle peak at the antinode (the strongly peaked features in Fig. 3.5). Values quantitatively agree with area-averaged STS [68]. Δ_{AN} increases with underdoping $p<0.12$, shows weak doping dependence for $0.12\leq p\leq 0.19$, and decrease with increasing doping $p>0.19$. Moving into region **A**, antinodal EDCs at low temperature become entirely featureless 3.6. The absence of a quasiparticle peak in

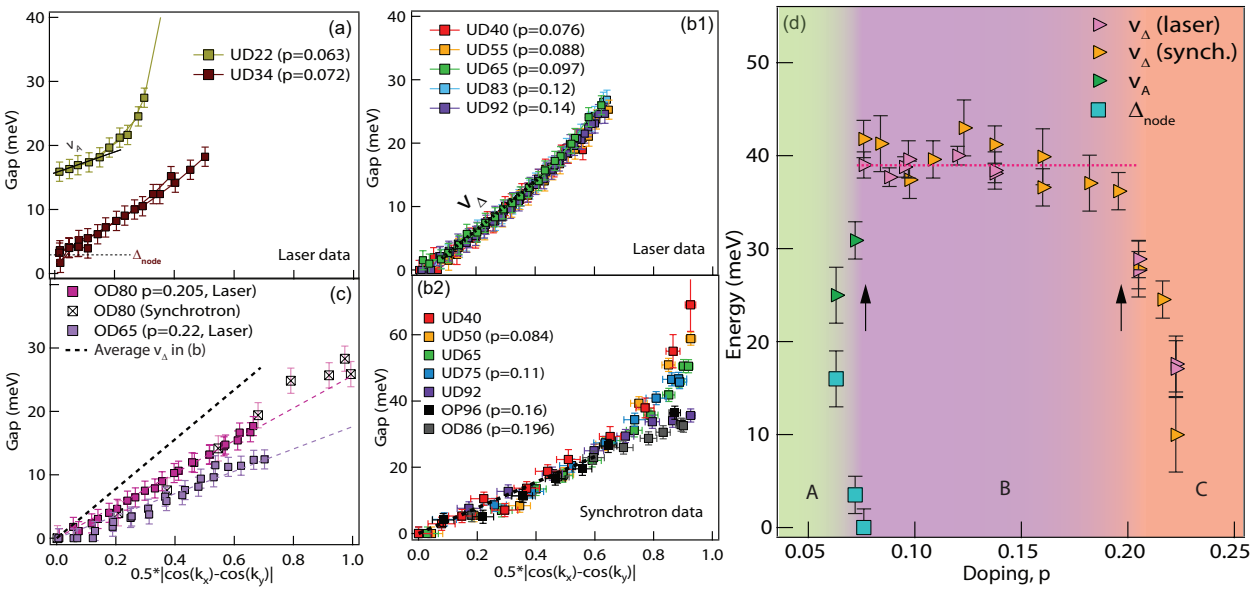

Figure 3.3: Three distinct phase regions at low temperature. Label UD/OP/OD denotes underdoped/optimal/overdoped sample with T_c given by the number which follows. (a)-(d) Gaps plotted in terms of the simple d-wave form. v_Δ (v_A) is from a fit over the linear portion of the gap function, as shown by dotted(solid) line in (b1,a). (a) In region **A**, Fermi surface is fully gapped with gap minimum, Δ_{node}, at nodal momentum. Gap anisotropy v_A decreases with underdoping. (b1-b2) Region **B** has doping-independent v_Δ. (c) In region **C**, v_Δ decreases as T_c decreases. Dashed line is guide-to-the-eye for average v_Δ observed in region **B**. Error bars in laser-ARPES reflect 3σ error in fitting procedure and an additional 100% margin. Error bars in synchrotron data reflect uncertainty of determining E_F (± 0.5 meV), error from fitting procedure, and an additional 100% margin. (d) Summary of low-temperature NN energy scales. Arrows mark critical dopings dividing phase diagram into three phase regions.

ARPES spectra is not definitive, because it may indicate that the optimal experimental conditions (photon-energy, polarization, cut direction) were not employed for that particular sample. However, it is intriguing that remnants of antinodal quasiparticles disappear at the same doping where a gap appears at the nodal momentum.

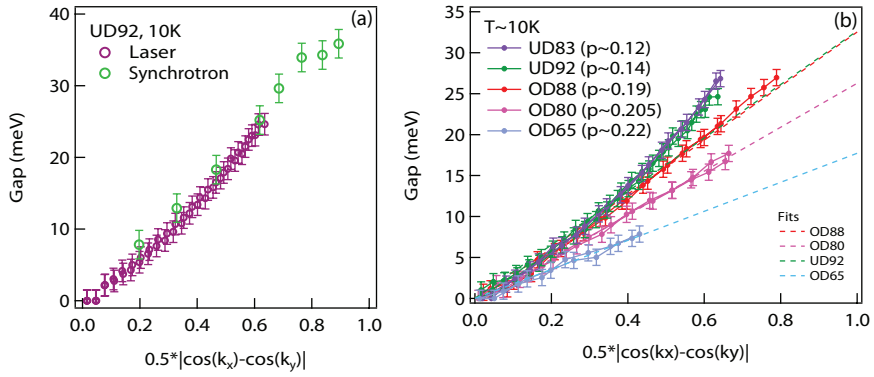

Figure 3.4: Gap functions at 10K. (a) UD92: laser/synchrotron comparison. (b) Change in momentum-dependence of gaps going from lightly underdoped to overdoped regime. Dotted lines are fits to v_Δ as described in Fig. 3.3.

3.3.2 Temperature Dependence

In Fig. 3.7 we compare low temperature gaps with gaps just above T_c in each of the three phase regions. For samples which are in region **A** at low temperature, the NN gaps are temperature-independent across T_c, and the Fermi surface remains gapped at every momentum above T_c, in agreement with LSCO data in Ref. [69]. This indicates that the gap at the nodal momentum does not have a purely superconducting origin and that the onset doping for region **A** is the same at low temperature and T_c. In region **B**, gaps close or diminish near the node at T_c while AN gaps remain above T_c. This observation of Fermi arcs near the node and gaps near the antinode is the usual ARPES signature of the pseudogap above T_c. Here, Fermi arcs are defined as momenta where the symmetrized EDCs at k_F are peaked at E_F implying zero gap [61]. All of the samples which exhibit characteristic doping-independent NN gaps of region **B** at low temperature also display a Fermi arc and antinodal gap above T_c. Additionally, OD80 ($p\approx0.205$) has an AN gap persisting $T>T_c$, demonstrating a pseudogap above T_c at this doping. Thus, we classify the temperature-dependence of OD80 with region **B** in Fig. 3.7 even though it exhibits region **C** phenomenology at low temperature. This suggests that the doping separating regions **B** and **C** may be different at low temperature and T_c and that the pseudogap may exist at higher temperature for $p>0.19$. Finally, the most overdoped sample in the study, OD65,

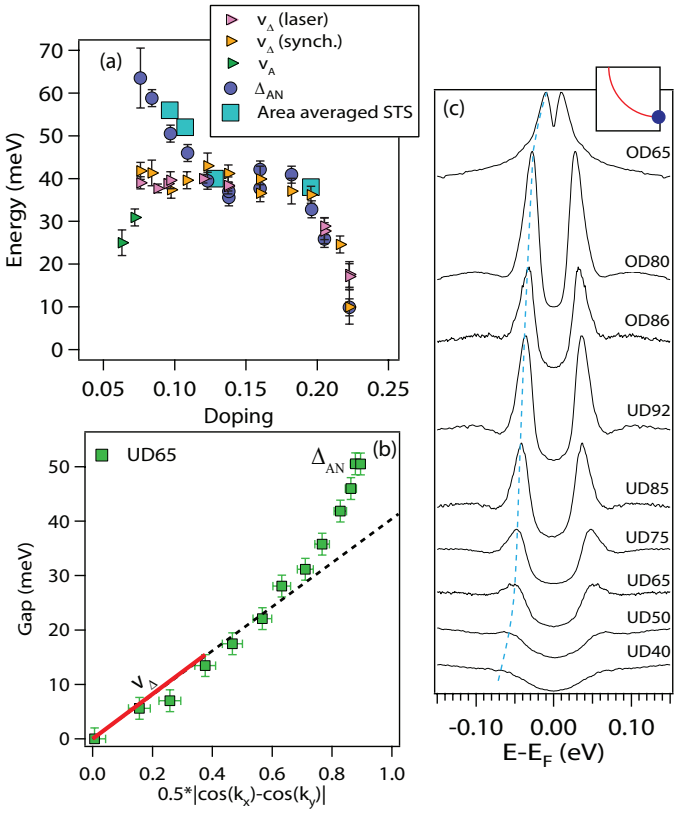

Figure 3.5: Antinodal gap at low temperature. (a) Comparisons of v_Δ, V_A, and Δ_{AN}, the antinodal gap. STS data for comparison from Ref. [68]. (b) definition of Δ_{AN}. (c) antinodal EDCs for a selection of dopings.

exhibits an ungapped Fermi surface T>T_c, demonstrating that the pseudogap above T_c persists until p≈0.22, in agreement with other recent ARPES results [70].

We study temperature-and-doping dependence of gaps below T_c in two ways: doping dependence at comparable temperature and temperature dependence at varied dopings. The former is shown in Fig. 3.8, where three dopings (UD40, UD65, and UD92) are studied at three temperatures. These three dopings are chosen to be in a doping regime where superconductivity and pseudogap energy scales are separated to varying degree. Two distinct doping dependencies are observed in different regions of the Fermi surface: doping-independent gaps and gaps which increase with underdoping. At 10K, doping-independent gaps are observed at NN and IM momenta and gaps which increase with underdoping are observed at the AN. Just below

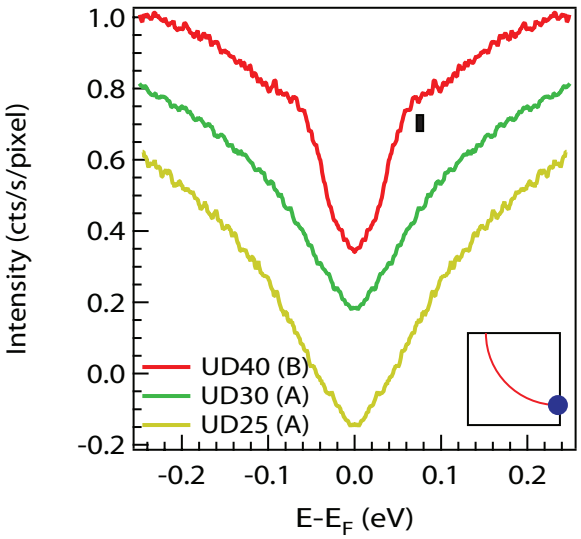

Figure 3.6: Antinodal symmetrized EDCs for dopings in region **A** (UD30, UD25) and region **B** (UD40). Cuts taken parallel to ΓY at 10K with 19eV photons in the second Brillouin zone. While UD40 shows remnants of quasiparticles at antinode below T_c, antinodal spectra for region **A** samples are featureless.

T_c, however, doping-dependent gaps extend into the IM region. Above T_c, gaps increase with underdoping everywhere except the Fermi arc. Notably, a region of the Fermi surface, marked with a dashed box in Fig. 3.8 is home to doping-*independent* gaps at low temperature but doping-*dependent* gaps near/above T_c. Fig. 3.9(a)-(g) shows a full temperature dependence of gaps from low temperature to just above T_c for a number of dopings ranging from UD34 to OD80. Temperature dependence near the node occurs in a limited temperature range within 25% of T_c, showing the temperature-dependence of the gap to be more abrupt than a mean-field model. The momentum region where gaps decrease near T_c becomes larger with increasing doping. This is seen by comparing the temperature dependence of gaps for different dopings at selected momenta (Fig. 3.9(h)-(m)). At the example momentum closest to the node ($0.5 * |\cos(k_x) - \cos(k_y)| = 0.2$), all dopings show the gap closing at T_c. At $0.5 * |\cos(k_x) - \cos(k_y)| = 0.4$, a doping dependence is clearly observed: the most underdoped sample (UD40) shows a gap which is unchanged across T_c, moderately underdoped samples (UD55, UD65) show gaps which close by about 30% across T_c,

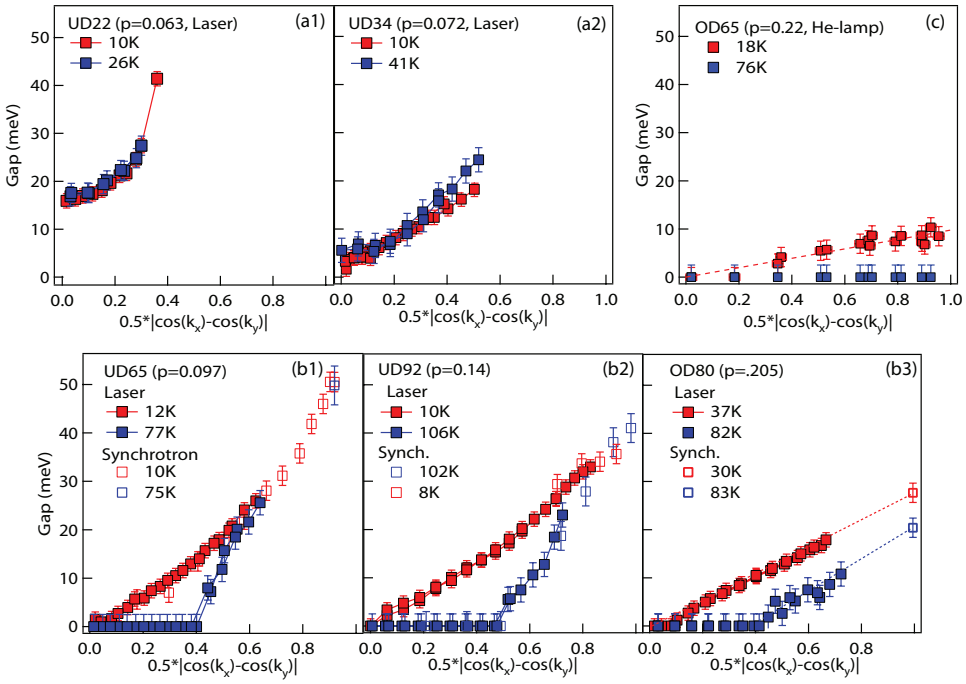

Figure 3.7: Distinct temperature dependence of gap in each of three phase regions. Red: low temperature gap. Blue: gap T>T_c. (a1-a2) In region **A**, NN gaps do not close across T_c. (b1-b3) In region **B**, NN gaps partially close at T_c, with AN pseudogap remaining T>T_c. OD80 is in phase region **C** at low temperature, but behaves like phase region **B** T>T_c. (c) He-lamp data. For p≥0.22, gap closes everywhere on Fermi surface T>T_c.

and the highest dopings (OD88, OD80) show gaps which close completely across T_c. At the antinode, most dopings show a gap which is unchanged across T_c, except for OD80 which shows a moderate temperature dependence (≈ 20%).

3.4 Discussion

3.4.1 Phase region A

Whereas some ARPES experiments suggest a smooth evolution of phenomenology from the moderately underdoped regime to the edge of the superconducting dome [61, 71, 72], our data indicate distinct physics in region **A** (p<0.076) which coexists

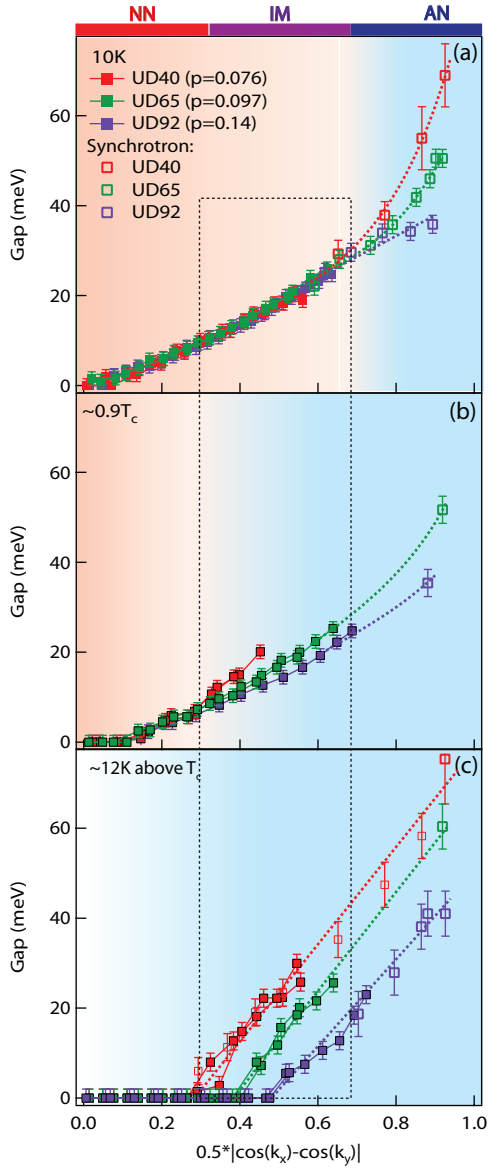

Figure 3.8: Phase competition in region **B**. (a)-(c) Gaps in UD40, UD65, and UD92 at 10K, 0.9T$_c$, and 12K above T$_c$. Synchrotron (laser) data shown with open (filled) symbols. Dashed lines are guides-to-the-eye. Doping-independent (dependent) gaps indicated by pink (blue) shading. Dashed box marks momenta where gaps are doping-dependent in (b)-(c) but doping-independent in (a).

with superconductivity, characterized in ARPES by gaps at every Fermi surface momentum. This is commonly called a 'nodal gap' even though that phrase is a bit of

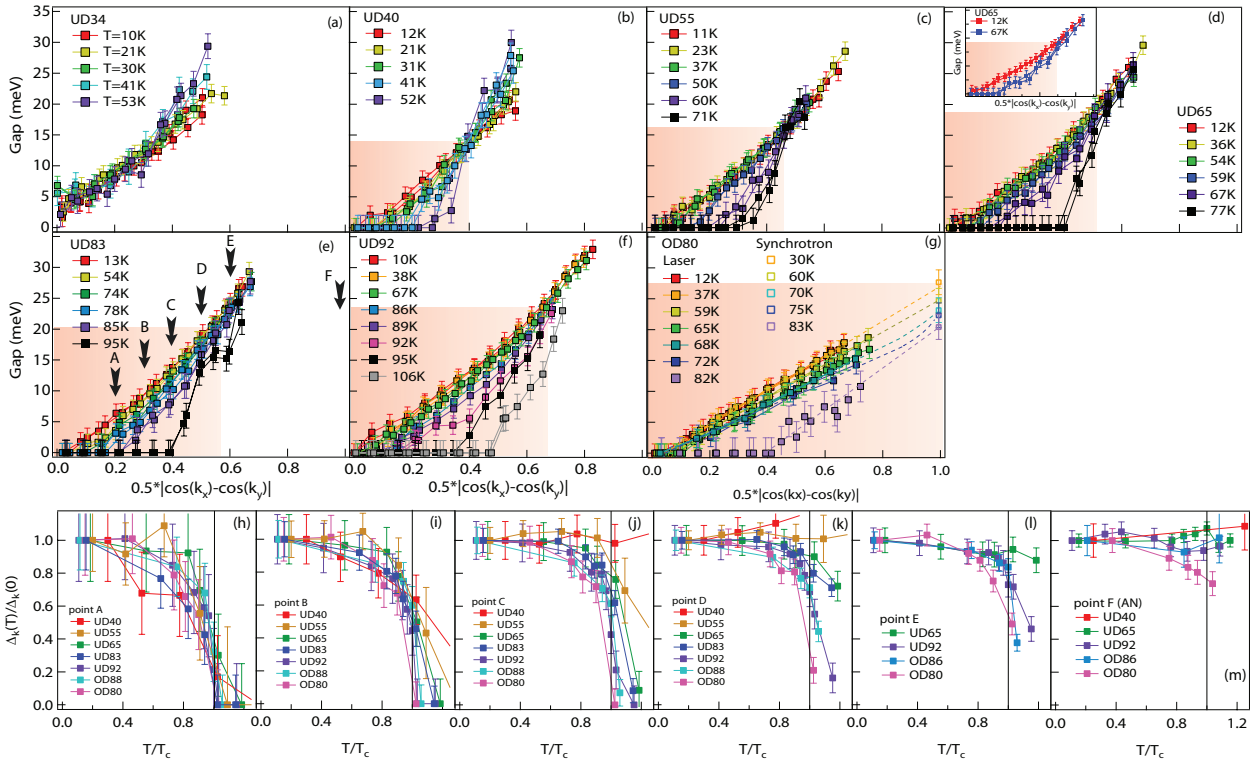

Figure 3.9: Temperature dependence of gaps across T_c in two ways: comparison of different temperatures at fixed dopings (a)-(g) and comparison of different dopings at fixed momenta (h)-(m). (a)-(g) Gaps from low temperature to $T>T_c$. Shaded region denotes momenta where gap $T>T_c$ is smaller than low temperature gap, as explained in inset of (d). (h)-(m) Gaps for different dopings at momenta indicated in panel (e).

an oxymoron. These results are supported by similar data in other cuprates. A fully gapped state at the underdoped edge of the superconducting dome has been shown in $Ca_{2-x}Na_xCuO_2Cl_2$ (Na-CCOC) [73] and $Bi_2Sr_{2-x}La_xCuO_{6+\delta}$ (La-Bi2201) [16], and our study is the first report of a fully gapped Fermi surface, both above and below T_c, in Bi-2212 at superconducting dopings. More recently, there have been published studies focusing on the nodal gap in superconducting $La_{2-x}Sr_xCuO_4$ (LSCO)[69] and La-Bi2201 [74], demonstrating that the nodal gap is a ubiquitous at the underdoped edge of the superconducting dome. It should be noted that these reports of a gap at the nodal momentum do not necessarily mean that the density of states at E_F is zero. For example, in Fig. 3.2(b), the density of states is clearly not zero. In Bi-2212,

there are three abrupt changes in NN gap phenomenology at p=0.076: a fully gapped Fermi surface appears, the gap anisotropy away from the nodal momentum starts to decrease, and the NN gaps become temperature-independent across T_c such that Fermi arcs are not observed. Notably, EDCs in region **A** remain sufficiently sharp near the nodal momentum, such that it is unlikely that this behavior is primarily disorder driven (Fig. 3.2). There have been recent reports of a similar critical doping p≈0.07-0.10 in $YBa_2Cu_3O_y$ (YBCO), varyingly attributed to a metal-insulator quantum critical point [75], a Lifshitz transition [76], or spin density wave order [19]. While a similar onset doping might suggest a common origin of phenomena observed in YBCO and Bi-2212, there are some inconsistencies, such as thermal conductivity data, which do not support a fully gapped Fermi surface at low dopings in YBCO [77]. This discrepancy may be materials-dependent, reflecting differences in disorder and Fermiology. Alternately, the ground state in region **A** may exhibit intrinsic time or spatial variation such that different techniques are sensitive to different aspects, which is supported by neutron scattering and muon spin-relaxation measurements in YBCO indicating slowly fluctuating spin order at the edge of the superconducting dome [78].

3.4.2 Phase Regions B and C

Though superconductivity has been shown to dominate at NN momenta [32, 33], Fig. 3.3(b) indicates that NN gaps are remarkably insensitive to T_c in a broad doping range constituting region **B**, suggesting that NN gaps in region **B** do not reflect the bare superconducting order parameter. Another interpretation is that it is not depairing which limits T_c, but rather, phase fluctuations [79]. Other experiments also support a doping-independent v_Δ, including specific heat measurements in YBCO [80] and scanning tunneling spectroscopy (STS) data in Bi-based cuprates [81, 82]. We note that a recent paper (Ref. [83]) discussed the momentum-and-doping dependence of low-temperature gaps in terms of a monotonically increasing magnitude of higher harmonics in the gap function towards underdoping. The data agree quantitatively between that work and ours. however, their interpretation is that the

doping-independent v_{Delta} in region **B** is a coincidence, and our interpretation is that it is not a coincidence and is a manifestation of pseudogap physics. We interpret the sudden change in v_Δ at p=0.19 as the T=0 endpoint of the pseudogap, in agreement with penetration depth and Cu-site impurity doping experiments [80, 84]. Additionally, earlier ARPES data showed a maximum in the antinodal quasiparticle spectral weight at p=0.19 [67]. The more conventional relation between T_c and v_Δ in region **C** likely reflects a pure superconducting ground state at low temperature. Region **B** is identified as a coexistence regime of superconductivity and the pseudogap, with support from independent ARPES data in our study. For all of region **B**, coexistence of pseudogap and superconductivity in Bi-2212 manifests in ARPES via distinct temperature dependence of gaps near the node and further away from the node [32]. For the most underdoped portion of region **B** (p<0.12), coexistence also manifests in a gap function which deviates strongly from a simple *d*-wave form at the AN, such that $v_\Delta < \Delta_{AN}$, where Δ_{AN} is the antinodal gap. The doping where Δ_{AN} first surpasses v_Δ is not significant, and simply indicates the doping where the superconducting gap (NN) energy scale is sufficiently smaller than the pseudogap (AN) energy scale. For some lower T_c cuprates, gaps already deviate from a simple *d*-wave form at optimal doping and show stronger deviation than Bi-2212 in the underdoped regime [33, 36, 85]. Although the pseudogap is considered to be primarily an antinodal phenomenon, these new results uniquely demonstrate that its presence in region **B** also manifests at NN momenta, namely, the doping-independent v_Δ. Similarly, the absence of the pseudogap in the ground state p>0.19 is also apparent at NN momenta, via a doping-dependent v_Δ. The origin of the doping-independent v_Δ in region **B** remains unresolved, but it may indicate a superconducting gap whose magnitude is renormalized by coexistence with the pseudogap.

The temperature dependence of spectral gaps provides microscopic information about the momentum-and-temperature dependence of the superconductivity/pseudogap coexistence in region **B**. Fig. 3.8 demonstrates that at IM momenta, gaps have characteristic pseudogap-like doping-dependence–increasing with underdoping [20, 86]–when superconductivity is weak (absent) just below (above) T_c, but are doping-independent at low temperature. This demonstrates that the pseudogap is not static

below T_c, but rather, it is suppressed by superconductivity at low temperature. This nuance within the 'two-gap' picture indicates that the temperature dependence of the pseudogap must also be considered for quantitative understanding of the superconducting state.

Fig. 3.5 demonstrates that there is a doping range $0.12 \leq p \leq 0.19$ where Δ_{AN} is almost independent of doping and the gap function is close to a simple d-wave form (defined at $v_\Delta \approx \Delta_{AN}$); notably, in this doping range, T* decreases with doping (Fig. 3.11). This itself is a non-trivial observation which provides additional evidence that the pseudogap is suppressed by superconductivity below T_c, because the antinodal region assumes the doping-independence of near-nodal gaps, rather than the doping-dependence of T*. It must be noted that although a slight curvature away from a simple d-wave form is observed in laser-ARPES data for UD83 and UD92, both with $p \geq 0.12$ (Fig. 3.4, but $v_\Delta \approx \Delta_{AN}$ in those samples, such that near-nodal and antinodal energy scales are similar and the gap function is not considered to deviate strongly from a simple d-wave form. Nevertheless, this slight curvature of the gap function may be important for understanding subtleties of pseudogap/superconductivity coexistence.

Fig. 3.8 shows that the Fermi arc just above T_c does not represent the only momenta where superconductivity emerges, because the doping-independent gap region at T=10K extends beyond the Fermi arc measured $T > T_c$. A better way to define momenta with superconducting character is by temperature dependence near T_c, and the superconductivity-dominated momentum region defined in this manner expands with doping. Although a pure superconducting gap closes entirely at T_c, we use a more lenient definition–a gap which diminishes approaching T_c–to define momenta with superconducting character. This momentum region is shaded in pink in Fig. 3.9(a)-(g) and gets larger with increasing doping. We note that superconductivity exists over the entire Fermi surface in Bi-2212, as sharp quasiparticles are observed at the AN for $p > 0.08$ [65, 67], but our definition of the 'superconducting region' selects the portion of the Fermi surface where the temperature dependence of gaps indicates significant spectral contributions from superconductivity. This definition also permits for coexistence of pseudogap and superconductivity at some momenta,

accounts for the observation that the pseudogap itself has temperature dependence, and is not hindered by difficulties in defining the Fermi arc length due to its temperature dependence [61]. The temperature dependence data in Figs. 3.9 and 3.8 provides a phase competition picture of superconductivity/pseudogap interaction in momentum space: the pseudogap is suppressed by superconductivity at low temperatures and larger dopings. When the pseudogap is suppressed, it surrenders a portion of the Fermi surface where it once existed.

Determining T*

Fig. 3.11 shows T* from ARPES, STS, and SIS tunneling experiments together, because these are comparable techniques where T* is determined by a suppression of antinodal density of states at E_F. If T* is sufficiently low to be accessible by ARPES, we use a standard definition [61, 87], defining T* as the temperature when symmetrized antinodal EDCs at k_F exhibit a single peak at E_F, as shown in Fig. 3.10 (a). For more underdoped samples, T* is not reliably accessible by ARPES, because oxygen can become mobile above T≈200K changing the doping near the surface during the course of an experiment. In those cases, T* is determined by extrapolating parameters measured in the pseudogap state at lower temperature, such as the spectral loss function [61] or the fitted gap [64], as shown in Fig. 3.10(b)-(d).

3.4.3 Proposed Phase Diagram

The starting point of the phase diagram proposed in Fig. 3.11 is the observation of three distinct phase regions at low temperature as a function of doping, separated by two potential quantum critical points inside the superconducting dome at p=0.076 and p=0.019. The former marks the onset of region **A**, whose experimental signatures in ARPES suggest an emergent phase which coexists with superconductivity, while the latter is interpreted as the T=0 endpoint of the pseudogap. The p=0.19 critical point of the pseudogap has support from thermodynamic experiments in several cuprates [80, 84], and various experiments support a distinct phase at the underdoped edge of the superconducting dome [19, 73, 75], though its precise identification

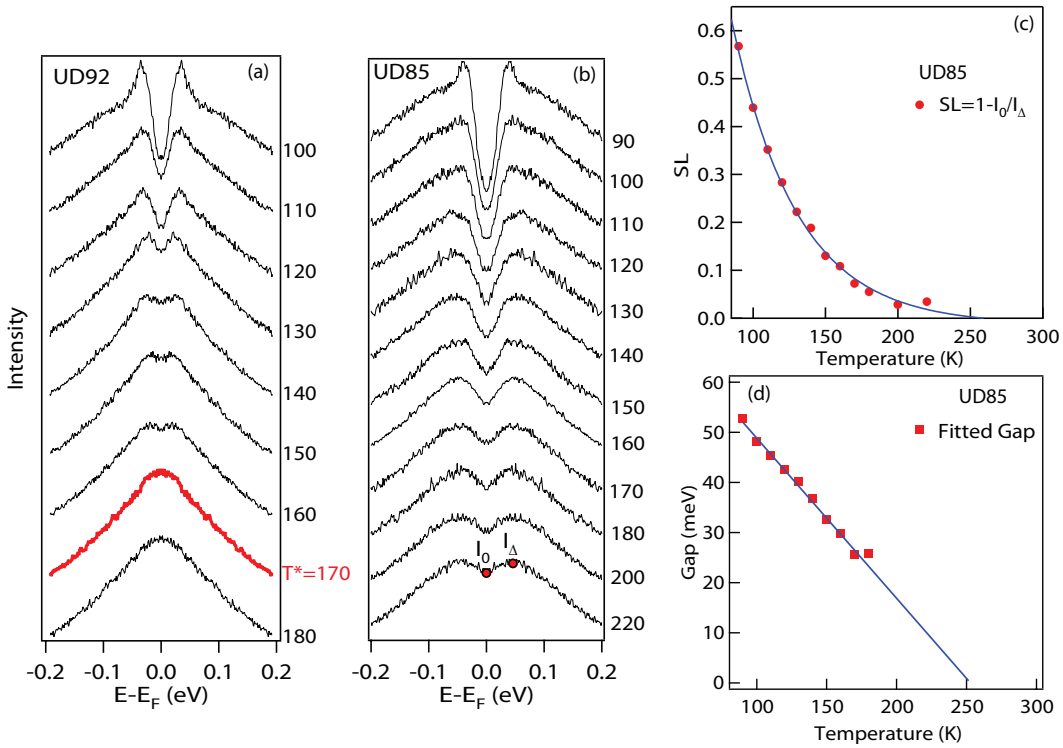

Figure 3.10: Extracting T* from ARPES data. (a) UD92. Symmetrized EDCs at k_F T>T_c. T* highlighted in red, defined as temperature when symmetrized EDCs show a single peak at E_F. (b) UD85, symmetrized EDCs at k_F. (c)-(d) T* determined from extrapolating spectral loss function (SL)[61] or fitted gap [64]. Because antinodal spectra are considerably broader above T_c, an additional lifetime term is included in the fitting, as discussed in Ref. [64].

is still debated. A trisected ground state has support from transport experiments in a magnetic field [76, 40] and some theoretical proposals also favor a ground state with multiple critical points [88]. Our data demonstrate how these critical points manifest in the phenomenology of NN spectral gaps. The phase diagram in Fig. 3.11 also features conjectured re-entrant behavior of the pseudogap inside the superconducting dome, as a direct consequence of phase competition between superconductivity and the pseudogap [89, 90, 91] which is reflected in temperature dependent ARPES data (Fig. 3.8, Fig. 3.9. The phase boundary between regions **B** (SC+PG) and **C** (SC) is anchored by ARPES data at T=0 and T=T_c, which show a sudden change in v_Δ and an absence of pseudogap T>T_c, respectively. It is supported by OD80 data which

obeys region **C** phenomenology at low temperature, but region **B** phenomenology at higher temperature, with the pseudogap persisting above T_c. It has been shown that the T=0 endpoint of a competing order is expected to shift under the superconducting dome [92], such that high temperature measurements of the pseudogap phase boundary do not extrapolate to the T=0 endpoint seen inside the superconducting dome. This manifests clearly in the $BaFe_2As_2$ family of iron pnictides compounds where both magnetic and structural phases have been shown to coexist with and be suppressed by superconductivity [93, 8], and a phase diagram with re-entrant behavior has been demonstrated [8]. A phase diagram with a reentrant pseudogap resolves conflicting reports about the fate of the pseudogap transition temperature, T*, inside the superconducting dome. Some experiments suggest that the T* line intersects the superconducting dome and reaches T=0 at p=0.19 [20, 80], whereas others, particularly spectroscopies, including our ARPES measurements of T* shown in Fig. 3.11, indicate that T* and T_c merge on the strongly overdoped side [70, 94, 95, 96]. Though variations between different experiments are expected, the data in this chapter demonstrate both behaviors within a single technique.

3.5 Conclusions

We have performed a thorough doping-and-temperature dependence study of spectral gaps in superconducting Bi-2212. At low temperature, there are three distinct phase regions with different characteristic phenomenology of NN gaps. In phase region **B** ($0.076<p<0.19$), which is identified as a regime where superconductivity coexists with the pseudogap in the ground state, gaps at NN and IM momenta are independent of doping. In region **C** ($p>0.19$), identified as a pure superconducting ground state, the *d*-wave superconducting gap decreases as T_c decreases. Region **A** ($p<0.076$) is identified as an emergent phase characterized by a fully gapped Fermi surface and a gap anisotropy which decreases with underdoping. Temperature dependence of gaps reveals a phase competition picture of the pseudogap and superconductivity, where pseudogap physics dominates a smaller region of the Fermi surface at low temperatures and larger dopings. From these doping-and-temperature dependence

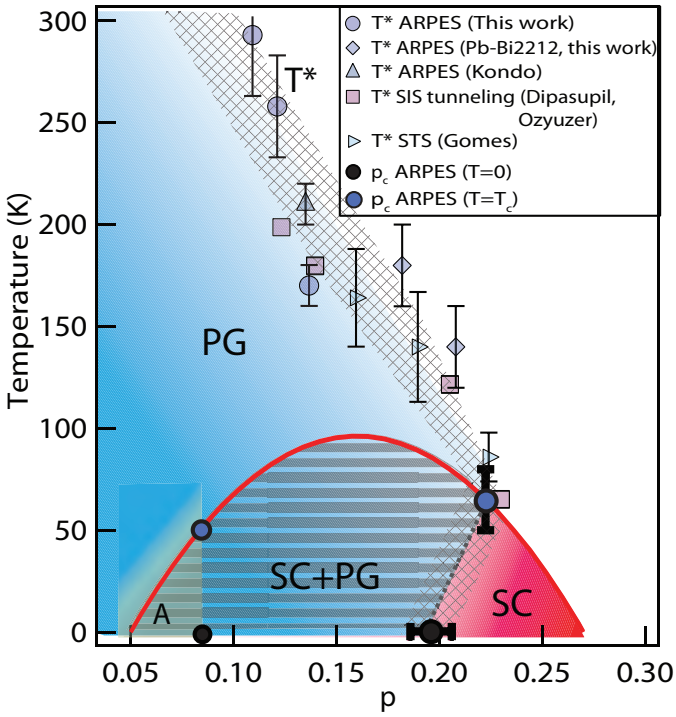

Figure 3.11: Proposed phase diagram. T* is determined from ARPES measurements at antinode (SI appendix and Ref. [87]), STS [94], and SIS tunneling [95, 96].

data we propose a new phase diagram featuring a trisected superconducting dome and conjectured re-entrant behavior of the pseudogap.

Chapter 4

Quasiparticles in Bi-2212

4.1 Introduction

This chapter focuses on quasiparticles in the superconducting state. The first section highlights the appearance of well defined momentum eigenstates even when the gap function deviates from a simple d-wave form (published in Ref. [66]). The second section makes comparisons between ARPES and Fourier-transform scanning tunneling spectroscopy to illustrate different conclusions about quasiparticles from single particle and two particle experiments (Ref. [65]). The final section discusses the presence of upper Bogoliubov peaks below T_c and their absence above T_c (published in supplements of [39]).

Table 4.1: Summary of samples studied for this chapter with their composition.

Sample	Composition
UD50	$Bi_2Sr_2(Ca,Y)Cu_2O_{8+\delta}$
UD65	$Bi_{2+x}Sr_{2-x}CaCu_2O_{8+\delta}$
UD75	$Bi_2Sr_2CaCu_2O_{8+\delta}$
UD92	$Bi_2Sr_2CaCu_2O_{8+\delta}$

4.2 Quasiparticles and deviation from simple *d*-wave form

Recently there has been increasing experimental evidence indicating that superconductivity and the pseudogap are distinct quantum phases with the former dominating near the node, the latter dominating near the antinode, and both coexisting below T_c [32, 33, 34, 35, 36, 37, 62]. The topic of quasiparticles is relevant in this context because it highlights important subtleties in this 'two-gap' picture below T_c.

In the simplest realization of a nodal/antinodal dichotomy between superconductivity and the pseudogap, the two orders are completely disjointed and occupy different momenta on the Fermi surface. In this scenario, one would not expect superconducting quasiparticles at the antinode. However, sharply peaked spectral features are observed over the entire Fermi surface in Bi-2212 (Fig. 4.1), and those near the antinode are likely of superconducting origin because they disappear above T_c. Closer to the node where the gap is smaller, upper Bogoliubov quasiparticles are observed, confirming the superconducting origin of quasiparticles there. Thus, below T_c, ARPES observes superconducting features over the entire Fermi surface, even in the antinodal region. This subtlety within the two-gap picture cannot be neglected: although the pseudogap dominates near the antinode, superconducting spectral features are also seen there.

One manifestation of the pseudogap below T_c is a deviation of the gap function from a simple *d*-wave form near the antinode [35, 36, 33]. This is observed $p \leq 0.125$ in Bi-2212 and at optimal doping for lower T_c cuprates such as LSCO and Bi-2201. It has been suggested that this deviation from a simple *d*-wave form is measured only because sharp quasiparticles are absent in the antinodal region–i.e. the gap is defined differently at the antinode or its energy is difficult to define because of broader spectra [97, 98]. While antinodal quasiparticles may be less robust in lower T_c cuprates, this idea is not borne out in ARPES data in Bi-2212. Figure 4.1 shows quasiparticles from the node to the antinode for four underdoped Bi-2212 samples at 10K, together with fits of the gap at each momentum. Notably, for the three most underdoped samples, the gap function deviates from a simple *d*-wave form, but

quasiparticles are still observed at the momenta where this deviation happens. The gap fits in Fig. 4.1(e)-(h) reflect the energy position of the superconducting feature. However, its energy position is strongly influenced by the underlying pseudogap such that the superconducting feature appears at a higher binding energy than it would in the absence of the coexisting pseudogap.

It has also been suggested that the gap function in Bi-2212 only deviates from a simple d-wave form in samples with cation substitution on the calcium site, and this observation thus reflects more disordered samples. However, the gap function deviates from a simple d-wave form in the UD75 sample where doping is achieved only by oxygen annealing. In addition, the quasiparticle spectral weight, the antinodal energy gap, and other pertinent spectral features show a continuous evolution from the lightly underdoped regime (only oxygen annealing) to the deeply underdoped regime (cation substitution). Nevertheless, the details of how different chemical substitutions affect cuprate physics is an important thing to quantify in subsequent studies. Oxygen annealing can only dope Bi-2212 in a limited range (see Fig. 1.5) which is insufficient for truly comprehensive studies, so substitutional doping is unavoidable. It is crucial to understand what else changes besides doping when those chemical substitutions are made.

4.3 Quasiparticles in ARPES and STM

Scanning tunneling spectroscopy (STS), a real-space probe, has been used to infer momentum space properties of cuprates by studying the Fourier transform of spatial conductance maps [99, 100, 101, 102]. In quasiparticle interference (QPI), quasiparticles scattering from impurities in a superconductor interfere with one another, producing a standing wave pattern in the local density of states $\rho(\mathbf{r},\omega)$, which can be studied via Fourier transform, $\rho(\mathbf{q},\omega)$. The dispersion of the peaks in $\rho(\mathbf{q},\omega)$ as a function of bias voltage ω is analyzed in terms of the octet model and yields information about the Fermi surface and momentum dependence of the superconducting gap [100, 101, 102]. Dispersing QPI peaks are observed over a limited energy range, corresponding to the portion of the Fermi surface indicated in Fig. 4.2. At low bias

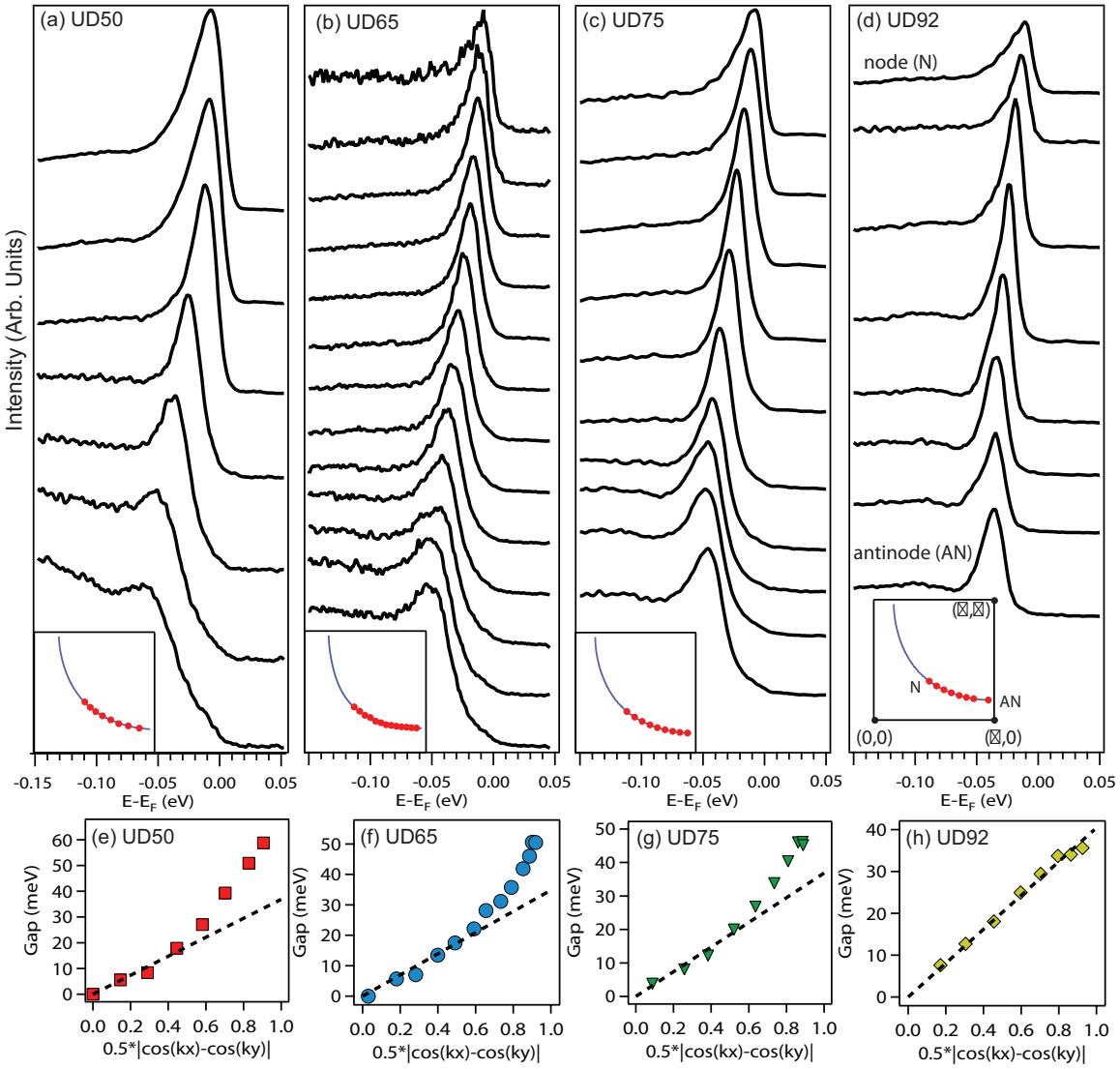

Figure 4.1: EDCs and gap fits for underdoped Bi-2212. (a)-(d) EDCs at k_F (T=10K) for four dopings. Top curve is near the node and bottom curve is near the antinode. Insets sketch where cuts intersect Fermi surface. Sharp peak in all EDCs demonstrate that quasiparticles are observed by ARPES all around the Fermi surface in underdoped Bi-2212 in this doping regime. (e)-(h) Gaps fit from the EDCs in (a)-(d). The three most underdoped data show a deviation from a simple d-wave form near the antinode, while still having sharp quasiparticle peaks at the same momenta.

voltage, it is likely that QPI is weak or absent because of tunneling matrix elements

which suppress near-nodal states [103], and this explanation also reproduces the disagreement in the momentum dependence of the superconducting gap between ARPES and QPI. Dispersing QPI peaks are also absent at higher bias voltage: upon reaching the bias voltage associated with the antiferromagnetic (AF) zone boundary (line connecting (π,0) and (0,π)), many of the peaks in $\rho(\mathbf{q},\omega)$ disappear, leaving behind a localized state which breaks translational and rotational symmetry, which has been associated with pseudogap physics [100, 104]. From the extinction of QPI at the AF zone boundary, it has been suggested that superconducting quasiparticles themselves become extinct at the antiferromagnetic zone boundary, even in overdoped materials which are far away from the parent antiferromagnetic Mott-insulator state on the phase diagram. Fig. 4.1(a)-(d) clearly refutes the claim of extinction, as sharp peaks are seen all the way to the antinode, and Fig. 4.2(b)-(c) show that these peaks are always quasiparticle-like (scattering rate is smaller than binding energy) and their fitted scattering rate evolves smoothly around the Fermi surface, without diverging near the antiferromagnetic zone boundary.

To address this discrepancy, Ref. [65] considered a single impurity and a 'patch' impurity in a d-wave superconductor and studied the momentum dependence of the $\hat{T}$-matrix, which is the Fourier transform of the impurity Hamiltonian. From this, it was shown that certain types of impurities can suppress QPI peaks (a two-particle experiment), even though the quasiparticle is still present in the single-particle measurement (ARPES).

Thus, the proper thing to do is compare single-particle experiments to other single particle experiments, which is shown in Fig. 4.3. ARPES measures the single particle spectral function in a momentum-resolved manner, but without spatial resolution, while STS measures the density of states (momentum integrated) at every spatial point $\mathbf{r}$. They can be related to each other by integrating ARPES spectra over momentum and STS spectra over position.

$$\int \sigma(V)\mathrm{d}r \propto \int \mathrm{d}\omega[-\mathrm{f}'(\omega - eV)] \sum_{\mathbf{k}} |M_k|^2 A(\mathbf{k},\omega) \tag{4.1}$$

where f' is the derivative of the Fermi function, which is almost a delta function at

low temperature, A($\mathbf{k}$,ω) is the single particle spectral function measured by ARPES, and $|M_k|^2$ is a tunneling matrix element which reflects the momentum-dependence of tunneling probability. The tunneling matrix element in the cuprates is still debated [105], but functional form of the low-voltage tunneling conductance suggests that $|M_k|^2 \propto (\cos(k_x a) - \cos(k_y a))^2$. Implementing this matrix element provides good agreement between area-averaged STS and momentum-averaged ARPES at low bias voltage. The energy positions of the coherence peaks do not agree, with area averaged STS giving peaks which are about 6 meV larger than momentum-averaged ARPES. This may be because STS at positive bias is being compared to occupied ARPES spectra (corresponding to negative bias). If so, the particle-hole asymmetry may be meaningful and should be explored further. Alternately, this discrepancy may arise from experimental details of STS which are not being considered.

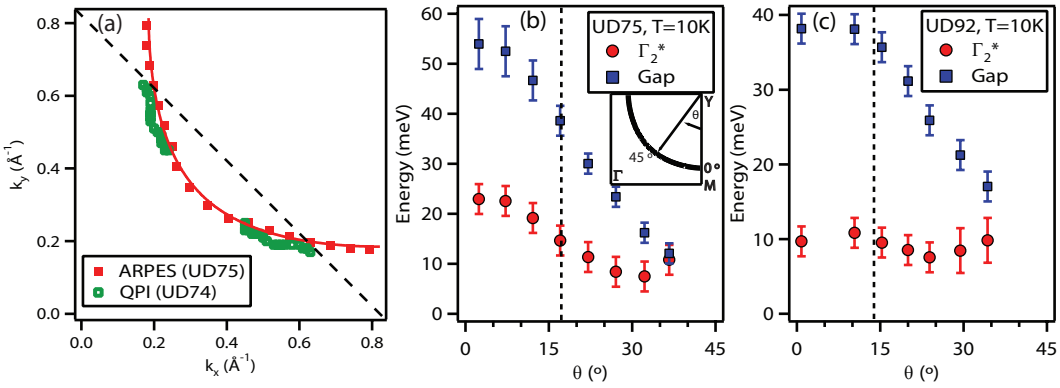

Figure 4.2: Comparison to QPI and momentum dependence of scattering rate. (a) Locus of quasiparticles observed by ARPES and QPI (Ref. [65, 100]) for samples of similar T_c. ARPES observes sharp quasiparticles all around the FS, whereas QPI implies quasiparticle termination at the antiferromagnetic zone boundary (dashed line). (b)-(c) Gap and scattering rate around the Fermi surface for UD92 and UD75, demonstrating that all the peaks in Fig. 4.1(a)-(d) are quasiparticle-like with a smoothly-evolving scattering rate. Details of fitting in Ref. [65]

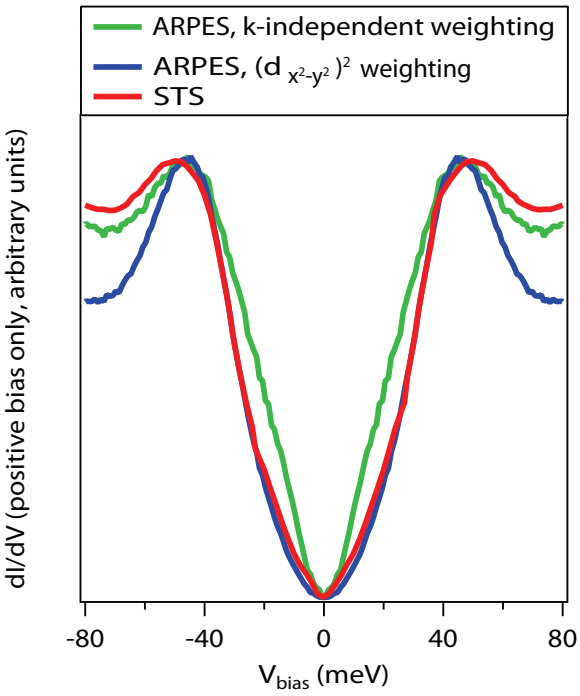

Figure 4.3: Comparison of momentum-integrated ARPES and area-averaged STS for underdoped samples with similar T_c, measured T≈10K. The two different momentum-integrated ARPES curves reflect different weighting of momentum points. In the green curve, all momenta are weighted equally. The blue curve involves a weighting $(\cos(k_x a)-\cos(k_y a))^2$. ARPES data are symmetrized. Characteristic STS spectra and their relative weights are taken from Ref. [106]. STS spectra show asymmetry between positive and negative bias, and only the positive bias side is compared to ARPES, because the background signal is smaller there. Spectra are normalized to have equal heights.

4.4 Upper Bogoliubov quasiparticles

A superconducting gap of magnitude Δ_{SC} opens symmetrically at k_F, and an EDC at k_F would have peaks at both $\omega=+\Delta_{SC}$ and $\omega=-\Delta_{SC}$ in the absence of a Fermi-Dirac cutoff. At higher temperature, there is a small thermal population of states above E_F, and upper Bogoliubov quasiparticles can be discerned [32, 107]. The enhanced photon flux of laser ARPES together with the lack beamline diffraction artifacts allows us to collect data with sufficient statistics to discern these upper Bogoliubov peaks over a wider doping, momentum, and temperature regime. The presence of the

upper Bogoliubov peak is the clearest signature of superconductivity seen by ARPES in the cuprates, because much of the Fermi surface remains gapped above T_c (the pseudogap) so a gap by itself does not signal superconductivity. The upper Bogoliubov peak is less pronounced in more underdoped samples, because the T_c is lower, and the quasiparticle intensity tends to decrease with underdoping. EDCs at k_F are shown below and above T_c in Fig. 4.4 for four samples, and the peak/shoulder feature attributed to the upper Bogoliubov quasiparticle is marked by an arrow and shown to be absent above T_c. A finer sampling of temperatures for OD80 and UD92 (Fig. 4.4(e)-(f)) further illustrates the difference between superconducting spectra and non-superconducting spectra. Notably, these data appear outside of the arc region of the pseudogap phase, defined as momenta where symmetrized EDCs imply zero gap, so if an upper Bogoliubov peak is present above T_c, we should be able to observe it at those momenta. The absence of upper Bogoliubov peaks above T_c, together with the doping-dependence of normal state gaps, suggests that superconducting fluctuations to not have strong spectroscopic signatures in ARPES, suggesting that the spectra above T_c reflect primarily pseudogap physics.

4.5 Conclusions

Because of robust superconductivity and sharp spectra, Bi-2212 provides an opportunity to study features of superconducting quasiparticles in the cuprates. Quasiparticles are observed over the entire Fermi surface for $p>0.08$, and their width does not diverge strongly approaching the antinode. Moreover, momentum-averaged ARPES and area-averaged STS yield comparable spectra, giving us confidence that correspondence between the two techniques can be found if equivalent metrics are compared. Near the node at elevated temperatures, upper Bogoliubov peaks are routinely observed, and their disappearance above T_c provides an in-situ confirmation of T_c.

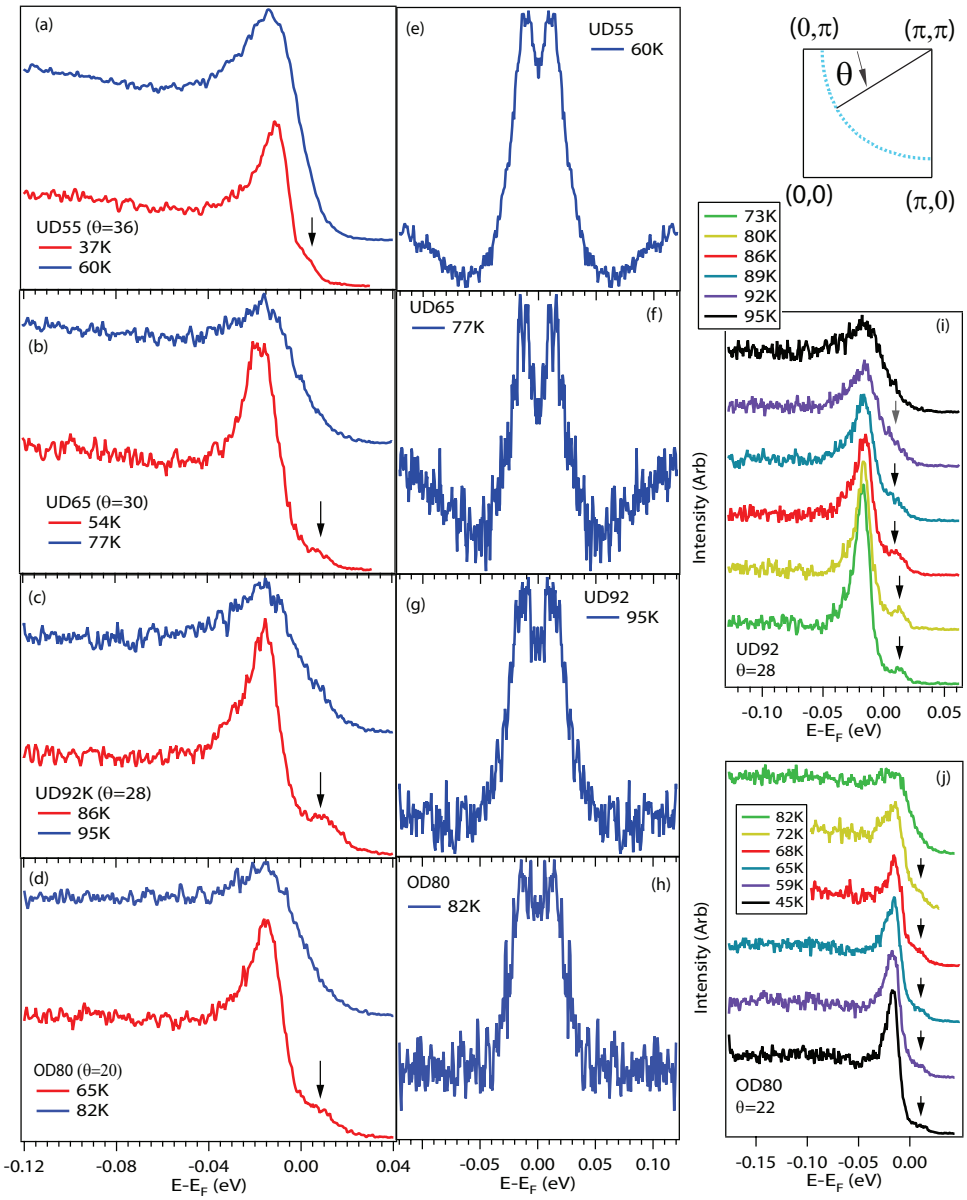

Figure 4.4: Disappearance of upper Bogoliubov peak above T_c. EDCs at k_F, cut chosen to be in the gapped region for T slightly higher than T_c. (a)-(d) EDCs at k_F below (red) and above (blue) T_c for UD55, UD65, UD92, and OD80. Upper Bogoliubov peak is marked by arrow in $T<T_c$ data, but is not visible $T>T_c$. (e)-(h) Symmeterized EDCs for $T>T_c$, showing that spectra are still gapped at these momenta. (i)-(j) Temperature dependence of EDC at k_F for UD92 and OD80. Arrows mark upper Bogoliubov peaks, which disappear across T_c. FS angle θ defined in top right of figure.

Chapter 5

Gaps and arcs above T_C

5.1 Introduction

ARPES data are rich with information, of which three pieces are needed to fully describe the phenomenology of the pseudogap above T_c: EDC width, gap, and spectral weight. These ingredients are all related, and their confluence may be key to understanding the real gap structure above T_c.

All three are illustrated in Fig. 5.1. Above T_c, the gap function features 'Fermi arcs'–loci of zero gap–near the node and gaps near the antinode. Additionally, there is a change in lineshape across T_c, particularly near the antinode, with EDCs becoming considerably broader (panels (c)-(d)). Fermi surface mapping illustrates that the density of states is nonzero in the antinodal region above T_c (Panels (e)-(f)). Even though spectra are determined to be gapped via symmetrization or leading edge midpoint analysis, this gap state does not completely deplete states at E_F.

5.2 Gaps and Fermi arcs

Fermi arcs were discovered in conjunction with the discovery of the pseudogap above T_c [59, 60] and their interpretation has been a topic of debate ever since. The Fermi arcs are curious entities because they do not form a closed contour in momentum

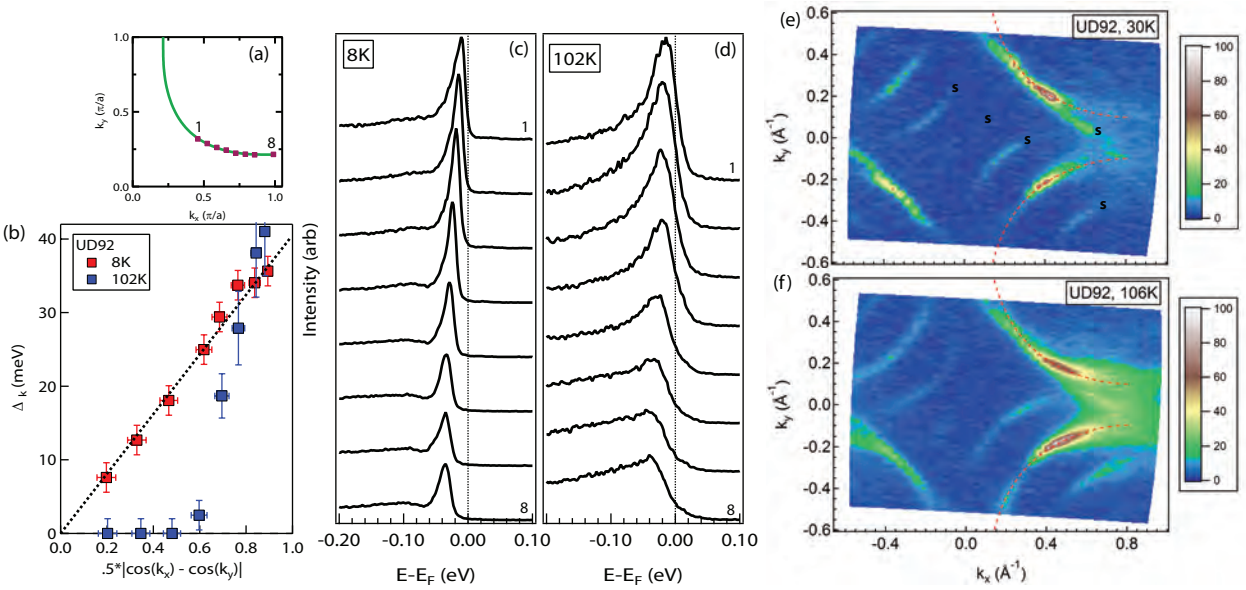

Figure 5.1: (a) Fermi surface (green) and Fermi crossings (purple) used in (b)-(d). (b)-(d) are from the dame data set, taken during a single experiment. (b) Gap at low temperature and above T_c for UD92. (c) EDCs at 8K. Top curve closest to node. (d) EDCs at 102K. (e)-(f) Mapping at 30K and 106K for UD92. Different data set from (a)-(d). Mapping integrates ± 5 meV centered at E_F. Dotted curves are a guide-to-the-eye for the underlying Fermi surface. Features labeled 's' are superstructure.

space. Fermi arcs have been interpreted as part of a closed hole pocket [72], a thermally smeared node [61], or as the momentum region which supports superconductivity [108]. There are two aspects of Fermi arcs which are contentious in the experimental literature: the arc length at T_c and the temperature dependence of arcs. The analysis in this section reports the gap; however, we must keep in mind that the EDC width can affect the ability to resolve a small gap, which is crucial for interpreting Fermi arcs. This will be the topic of the next section.

5.2.1 Fermi arcs at T_c

Because of thermal broadening, the temperature at which Fermi arcs are measured needs to be specified. We have studied Fermi arcs with laser ARPES just above T_c to minimize the effects of thermal broadening, and this is shown in Fig. 5.2.

The measured arc length at T_c ranges from 8° (out of 90°) for deeply underdoped samples to 27° for overdoped samples. The data are consistent either with a very weakly doping-dependent Fermi arc or a step-wise discontinuous doping-independent arc. In the first scenario, the arc length increases by 1.5° for every 1% increase in doping. There is a discontinuity p≈0.22 (not shown) where a large Fermi surface is recovered at T_c. In the second scenario, the arc length is independent of doping (≈11°) in the underdoped regime and suddenly jumps to a larger value or starts to increase monatonically at some important intermediate doping (either p=0.16 or p= 0.19). Previous synchrotron-ARPES experiments reported that the arc length increases with hole doping at a rate of almost 3° per % hole doping [32, 108], often with the implication that the arc length sets an energy scale related to T_c. However, for the underdoped samples we studied, the T_c varied by more than a factor of 2 (40K to 92K) and the arc length varied by a lesser factor. Part of the discrepancy may be that the synchrotron measurements were taken at ≈10K above T_c, and arcs may expand at different rates for different dopings [61]. Additionally, the synchrotron experiments were performed with poorer energy and momentum resolution, as well as a sparser sampling of momentum points. A doping-dependent Fermi arc made sense in the context of a nodal/antinodal dichotomy, where the arc above T_c reflected the portion of the Fermi surface where superconductivity existed below T_c. However, there is evidence that superconductivity suppresses the pseudogap in a momentum-dependent manner below T_c [39], so that interpretation of the Fermi arc is problematic. Furthermore, the doping-independent v_Δ observed in much of the underdoped regime (see Chapter 3) exists far beyond the Fermi arc in Fig. 5.2. This doping independent v_Δ is thought to be a superconducting feature, which argues against superconductivity being confined to the arc region.

There are a number of interpretations for the Fermi arcs at T_c in Fig. 5.2. In the same doping regime where Fermi arcs are independent of doping or weakly doping dependent, the low temperature v_Δ is independent of doping (see Chapter 3). This suggest that the Fermi arc length might reflect physics associated with superconductivity. Just below T_c, superconductivity may be squeezed into the small portion of the Fermi surface where the Fermi arc is observed just above T_c, and it is logical that

this momentum region be independent of doping because near-nodal superconducting gaps are independent of doping. Interestingly, an arc length of 11° (out of 90°) would produce an electron pocket occupying ≈2% of the Brillouin zone, assuming the diamond-shaped pockets described in Ref. [109]. However, this reconstruction has not been observed in ARPES. Potentially, the doping-independent arcs may have a more trivial explanation: on the underdoped side, spectra are broader but measurement temperatures are lower; approaching optimal doping, spectra are sharper, but measurement temperatures are higher. These two factors may conspire to broaden the arc (or whatever the underlying gap structure is) for different reasons at different dopings. Another possibility is that the measurement temperature is too close to T_c and the spectra are strongly influenced by fluctuating superconductivity or filamentary superconductivity.

Notably, away from the arc, gaps follow the doping-dependence of the pseudogap, increasing with underdoping.

5.2.2 Temperature dependence of arc length

Kanigel *et al* performed a comprehensive study of the temperature dependence of the Fermi arc length as a means to gain information about the ground state of the pseudogap [61]. By scaling temperatures with T*, they found that data from all dopings collapsed on one another and the arc length extrapolated to zero–a nodal point–in the limit of zero temperature, a so-called nodal-metal. This implies that the pseudogap is a *d*-wave superconductor which lacks phase coherence. There were a number of problems with this approach. First, T* is not accessible by ARPES in deeply underdoped samples, such that there is a large uncertainty in determining T* self-consistently. Second, this analysis involves extrapolating across the superconducting phase boundary which is not reasonable if the pseudogap and superconducting gap are of identical origin, as was their argument. Finally, the experiments in Ref. [61] were performed at 20meV energy resolution, which is more than twice the standard for modern experiments on Bi-2212. Nevertheless, the temperature evolution of the Fermi arc is a crucial piece of the phenomenology, so we have pursued these experiments with better

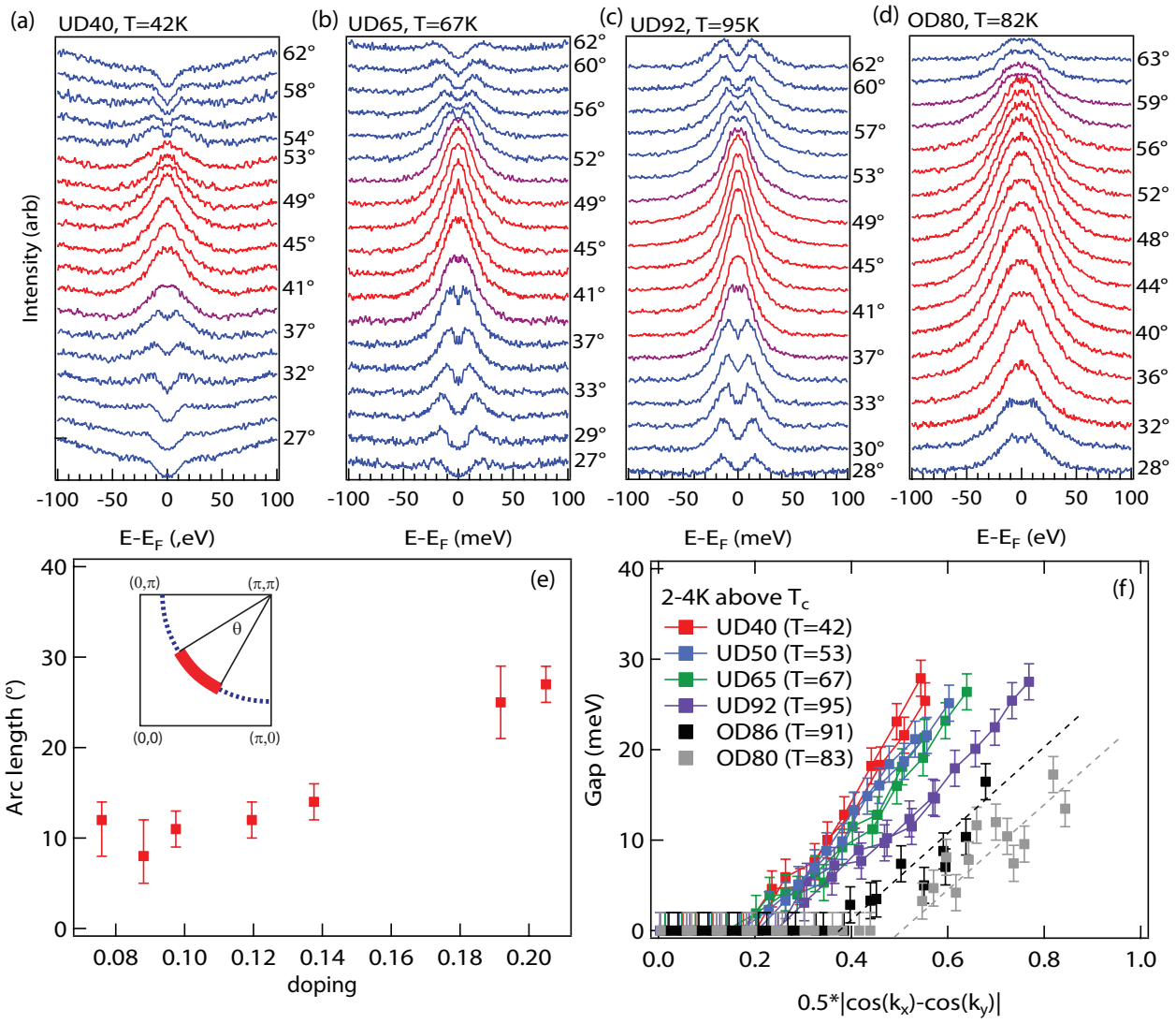

Figure 5.2: (a)-(d) Symmetrized EDCs for selected dopings. EDCs in the arc are red and EDCs in the gapped region are blue. Questionable EDCs are in purple. (e) Fermi arc length just T_c. Arc length units are defined in inset; angle includes both side of node. (f) Gaps just above T_c

resolution (10 meV).

The Fermi arc length as a function of temperature is shown in Fig. 5.3(b) for UD92 and UD75. For both samples the arc length grows linearly with temperature for a limited temperature range, consistent with previous experiments [61]. The

temperature dependence of the Fermi arc in this regime is not consistent with a nodal metal at zero temperature. For all the dopings, extrapolating to zero arc length yields a finite temperature, which may not be physical for the reasons discussed above. This is consistent with analysis in the supplements of Ref. [110]. It is important to emphasize that the arc length measured at any finite temperature is an upper bound of the real Fermi arc, as thermal broadening can obscure a small gap at the edge of the arc. Thus, with a better cleave, statistics, and resolution, one may find that the limit of zero arc length occurs at a higher temperature, but it is impossible to push the curve in the other direction with a better experiment.

Interestingly, above a temperature smaller than T*, labeled T2, the arc length shows no further increase. The Fermi surface momentum where the arc stalls is close to where the antiferromagnetic zone boundary intersects the Fermi surface for both UD75 and UD92. Although the arc is not increasing T2<T<T*, the remaining gap continues to close or fill in such that a complete Fermi surface is recovered above T*. T* can be reached with ARPES for UD92, but likely lies above room temperature for UD75. Two temperature scales above T_c and two distinct momentum regimes were reported in two recent papers from the AMES group [110, 87]. However, the boundary in momentum space that they report is *not* at the antiferromagnetic zone boundary.

Two distinct temperature regimes above T_c might be related to recent reports of charge order in underdoped YBCO [111, 112], which will be discussed later in this chapter. Alternately, a similar temperature dependence of Fermi arcs has also been reproduced within a phase fluctuation picture without invoking two transitions [113]. On the experimental side, we caution that the experiment in Fig. 5.3 should be repeated with Pb-doped samples such that there is no superstructure in the antinodal region and spectral features can be assessed more unambiguously. Nevertheless, the conclusion that the temperature dependence of Fermi arcs above T_c does not support a nodal metal ground state is still robust.

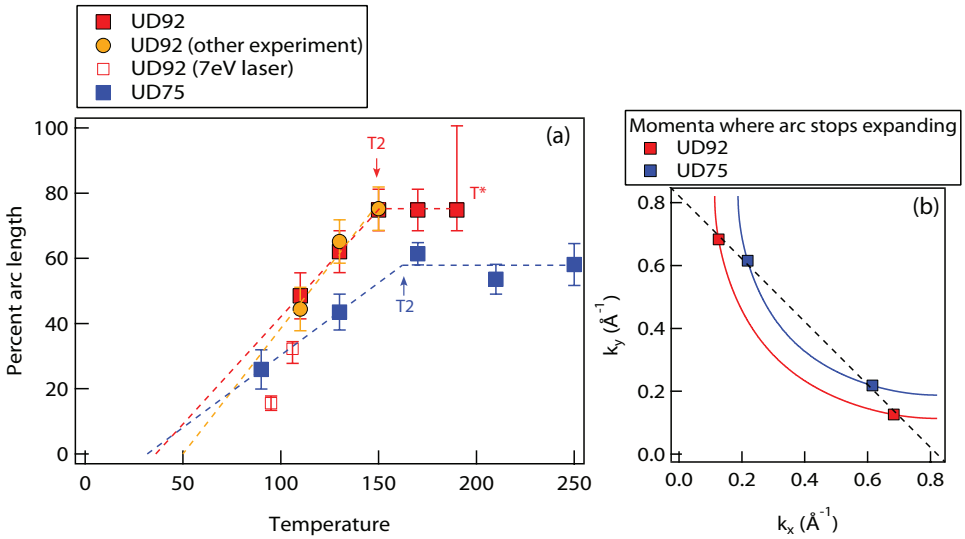

Figure 5.3: (a) Temperature dependence of Fermi arc for UD75 and UD92. Arc length is given as a percentage of the full Fermi surface (0= nodal point, 100= fully ungapped Fermi surface). Dotted lines T<T2 are linear fits extrapolated to zero arc length. Closed symbols: data taken at SSRL with 22.7 eV photons, cuts parallel to ΓM, and 10 meV energy resolution. Open symbols: data taken with 7eV laser, cuts parallel to ΓY, and 3 meV energy resolution. (b) Momenta where Fermi arc stops expanding. Dashed line is antiferromagnetic zone boundary.

5.3 EDC width

This section will discuss the lineshape evolution as a function of doping, temperature, and momentum. This information will be used in conjunction with simulation to clarify the real momentum space structure of the pseudogap. The starting point for this discussion is that thermal broadening can obscure a small gap. Thus, when an 'arc' is observed in ARPES data above T_c, there may potentially be a small gap in the arc region which is not measurable at the temperature of the experiment. ARPES data are in principle consistent with four scenarios (assuming a large pocket starting point) shown in Fig. 5.4: nodes or accidental nodes at the zone diagonal, gap at every Fermi surface momentum, real Fermi arcs, or a U-shaped gap structure with a small v_Δ. These scenarios reflect the gap structures which can be consistent with ARPES data, and the question of whether they can be explained by theory is put aside.

Additionally, while quantum oscillation experiments certainly point to small pockets in the (field induced) normal state, this figure explores the question of gap structure, not Fermi surface topology. In the case of a 'real' arc, the possibility that this is part of a closed pocket should be explored more thoroughly in future experiments.

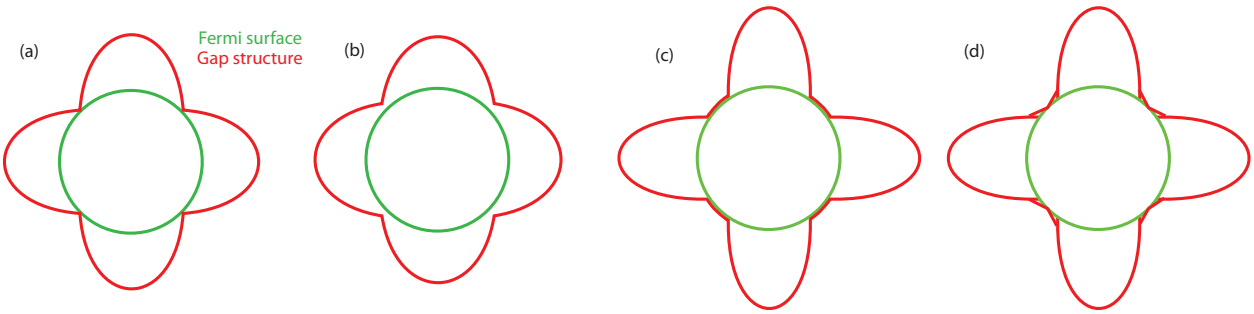

Figure 5.4: Scenarios for momentum-space gap structure T>T_c. (a) Real or accidental nodes (b) Gap at every Fermi surface momentum (c) Real Fermi arcs (d) U-shaped gap structure.

5.3.1 Fitting

Two lineshapes were used to fit spectra in this Thesis. The first is a minimal model proposed by M. Norman [64] (Norman Model). The second is a marginal-Fermi-liquid-like model, particularly, the spectral function explored in Ref. [114] (Kordyuk Model). The former will be discussed in this chapter, and the latter in Appendix A.

The Norman model is given by the following expression:

$$\Sigma(\mathbf{k},\omega) = -i\Gamma_1 + \frac{\Delta^2}{\omega + \epsilon(\mathbf{k}) + i\Gamma_0} \tag{5.1}$$

where Γ_1 is said to be an approximation of the single-particle scattering rate, since the real scattering rate likely depends on energy. Γ_0 is an elastic term that is usually only introduced above T_c. Note that this expression is only valid at k_F.

Figs. 5.5, 5.6, and 5.7 illustrates how each of the parameters in Eqn. 5.1, together with instrument energy resolution (3 meV), affects the symmetrized EDC at k_F. The starting point for each of the three figures (Δ=4 meV, Γ_1=22 meV, Γ_0=0 meV) was

chosen because it agrees well with ARPES data near the node in the superconducting state. When Δ is decreased (Fig. 5.6), the peaks on either side of E_F move towards each other, eventually forming a single peak when Δ=0. Increasing Γ_1 (Fig. 5.5) widens the outer envelope of the EDC, but a dip remains at E_F even for Γ_1 which is quite large. In an experiment, a dip at E_F is interpreted as a finite gap. Increasing Γ_0 (Fig. 5.7) fills in spectral weight at E_F without widening the outer envelope. Notably, when Γ_0 is sufficiently large, there is a single peak in the symmetrized EDC, even though a finite gap was explicitly included in the simulation. The condition for this is is given in Ref. [64] to be $2\Delta^2/{\Gamma_0}^2+\Gamma_1\Delta^2/{\Gamma_0}^3=1$. In an experiment, such a spectrum would be interpreted as having zero gap. Including instrument resolution in the simulations diminishes the depth of the dip at E_F and pushes the value of the smallest resolvable gap even larger. We note that for simplicity, the simulated EDCs assumed particle-hole symmetry which might not be correct in the pseudogap state.

In order to gain correspondence with experiments, simulated spectra in Figs. 5.5(b), 5.6(b), and 5.7(b) were fit to the Norman model convolved with a Gaussian of width 3 meV. Including the convolution with the instrument resolution in the fit diminishes some, but not all, of the spectral weight redistribution caused by instrument resolution. For the starting point in each of Figs. 5.5, 5.6, and 5.7 (Δ=4 meV, Γ_1=22 meV, Γ_0=0 meV), the fits yield Δ=4.6 meV, Γ_1=22 meV, Γ_0=2.8 meV. Including instrument resolution causes the EDC peak position, plotted in panels (c), to shift to slightly higher binding energy, but fitting recovers a Δ which is closer to the input for the model. The fitted Γ_1 is close to the input value for all variations of other parameters because the outer envelope of the EDC is fairly unambiguous. Because convolution introduces extra weight at E_F, the fitted Γ_0 is larger than the input. When the gap becomes smaller than this baseline (Fig. 5.6), the fit yields increasingly large Γ0. We note that in fitting real data, if there is a single peak in the symmetrized EDC, the fitting is unstable if both Δ and Γ_0 are free parameters. In Figs. 5.6 and 5.5, for symmetrized EDCs which only show one peak, we show fits where Γ_0 is fixed to zero. This tends to yield a fitted gap which reflects the peak separation in the symmetrized spectra. In real data, momenta further away from the node, where two peaks are present in the symmetrized EDC, can be used to asses Γ_0,

assuming that it is momentum-independent in the momentum regime of interest.

Fig. 5.7 gets to the heart of the difficulty of assessing small gaps at high temperature. Although the same gap is always input into the model, an increasing elastic scattering term (Γ_0) fills in the spectral weight at E_F, eventually yielding a single peak in the EDC. This is the reason that the temperature dependence of the Fermi arc length may be artificial. Coupling this with instrument resolution makes the EDC peaks move towards E_F, as if the gap were closing. Taken together, the measurement temperature and instrument resolution must be considered when comparing reported arc lengths from given experiments.

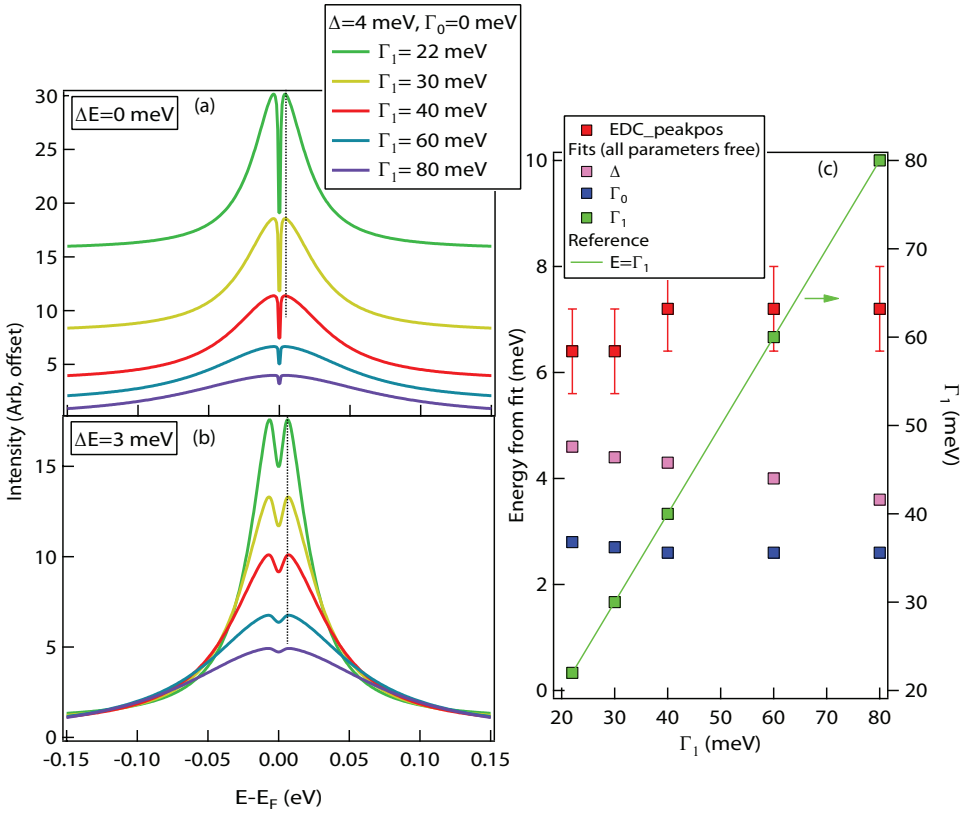

Figure 5.5: Simulated symmetrized EDCs at k_F, varying only Γ_1. (a) EDCs with varying Γ_1. Vertical dotted line is guide-to-the-eye for peak position of top trace. (b) EDCs in (a) convolved with Gaussian of width 3 meV. (c) fits of simulated data in (b). Γ_1 plotted on right axis.

The insight that a sufficiently large elastic scattering rate can obscure a small gap

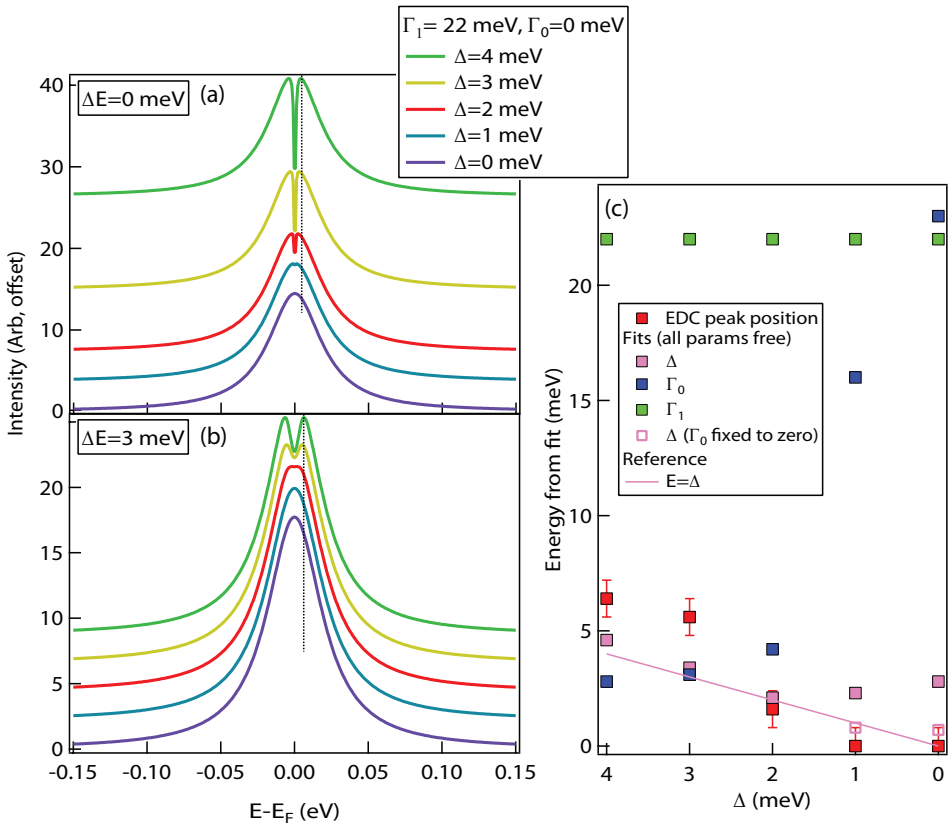

Figure 5.6: Simulated symmetrized EDCs at k_F, varying only Δ. (a) EDCs with varying Δ. Vertical dotted line is guide-to-the-eye for peak position of top trace. (b) EDCs in (a) convolved with Gaussian of width 3 meV. (c) fits of simulated data in (b). When a single peak is seen in the EDCs, a separate fitting where Γ_0 is fixed to zero is shown with open symbols.

and make it difficult to assess the veracity of Fermi arcs is appreciated by a number of ARPES groups. Thus, several alternate analysis techniques have emerged to address this deficiency of symmetrization [72, 110, 115]. The most promising proposal is to study properly normalized MDCs [110], because this gives information about spectral weight at E_F, which may be obscured by symmetrization while still studying raw or almost raw spectra. However, other proposed analysis techniques involve heavy manipulation of ARPES data and should be pursued with care, because the spectra are complicated. In particular, the problems with tDOS and deconvolution analysis is discussed in Appendix A. The advantage of symmetrization analysis is that it involves

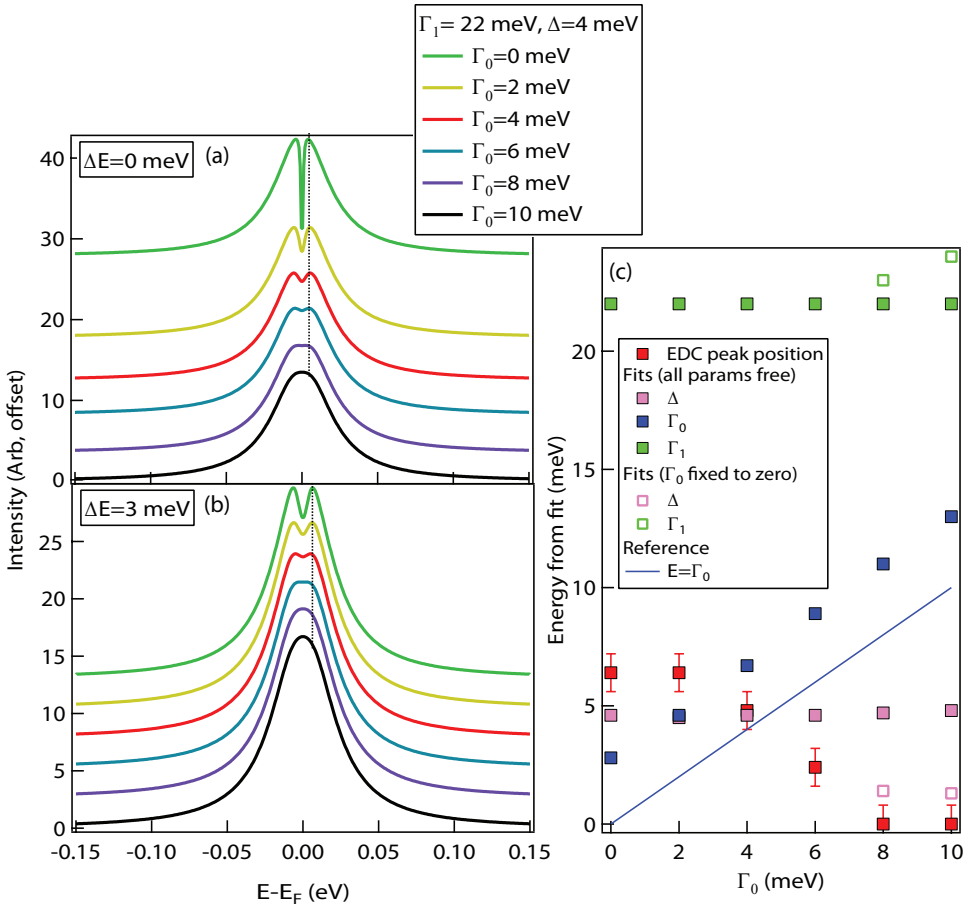

Figure 5.7: Simulated symmetrized EDCs at k_F, varying only Γ_0. (a) EDCs with varying Γ_0. Vertical dotted line is guide-to-the-eye for peak position of top trace. (b) EDCs in (a) convolved with Gaussian of width 3 meV. (c) fits of simulated data in (b). When a single peak is seen in the EDCs, a separate fitting where Γ_0 is fixed to zero is shown with open symbols.

only a mild operation to the data, such that the spectra being studied are almost raw data. Furthermore, the limitations of symmetrization are very straightforward: it only measures the occupied part of the gap and a small gap might be obscured by a large scattering rate. In the next section, we will discuss how the Norman model parameters evolve across T_c in real data.

5.3.2 Temperature and momentum dependence

Fig. 5.8 summarizes fitting below and above T_c for UD92. The raw EDCs (panels (a)-(d)) demonstrate a profound change in lineshape across T_c for antinodal momenta which is absent for momenta close to the node. This is quantified by Γ_1 which describes the width of the outer envelope of symmetrized EDCs. In synchrotron data, this parameter increases by a factor of 4 near the antinode across T_c, but only by a factor of < 2 at near-nodal or intermediate momenta.

Below T_c, Γ_1 is weakly momentum dependent, but above T_c the momentum dependence is more pronounced. Laser and synchrotron data are consistent when differences in the resolution and cut geometries of the experiments are considered. In the near-nodal region, synchrotron ARPES overshoots the real EDC width because momentum resolution effects are most pronounced when v_F is larger. Additionally, synchrotron data were taken with cuts parallel to ΓM with a larger entrance slit, and this further broadens nodal spectra. Γ_0 was fit in the portion of the Fermi surface where two peaks were visible in symmetrized EDCs. This parameter appears to be momentum-independent within error bars and increases with temperature. With a momentum-independent Γ_0, we can estimate the maximum observable gap, which is approximately 1/2 of Γ_0, as indicated in the simulation in Fig. 5.7. Thus, under the assumption of particle-hole symmetry near the node for UD92, the maximum measurable gap at 95K is 2 meV and the maximum measurable gap at 106K is approximately 4 meV.

The temperature evolution of near-nodal lineshapes is very different in Bi-2212 as compared to BCS superconductors, as shown in Fig. 5.9. In the latter, the scattering rate diverges approaching T_c [116]. In Bi-2212, Γ_1 increases only moderately across T_c. Γ_0 may have a steeper temperature dependence than Γ_1 across T_c, but approaching T_c, it does not appear to diverge. We note that in the original paper, Γ_0 in the Norman model was described as an inverse pair lifetime in a fluctuating superconductor. In this analysis, we are using Γ_0 purely phenomenologically to describe the DOS enhancement at E_F.

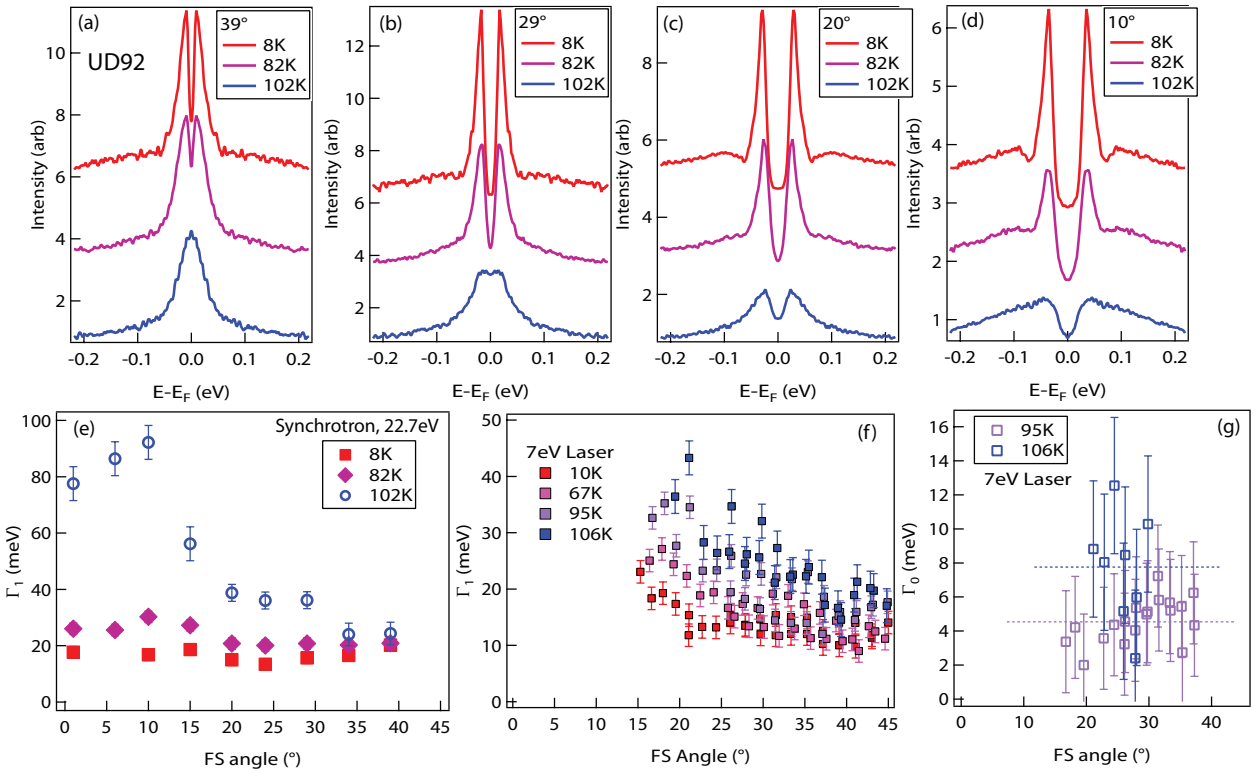

Figure 5.8: EDCs and Norman model fit parameters, UD92. (a)-(d) Symmetrized EDCs at selected momenta and temperatures, taken at SSRL with 22.7eV photons and cuts parallel to ΓM. (e) Γ_1 fit from same synchrotron data (f) Γ_1 fit from laser data, 7eV, cuts parallel to ΓY. (g) Γ_0 from laser data. Horizontal dashed lines are guide-to-the-eye.

5.3.3 Simulation: limits of real Fermi arc

Fig. 5.8 suggests lineshape parameters for UD92 in the near-nodal region which are given in Table 5.1. These are used with ansatzes for the gap function to construct what the experimentally measured gap function, particularly the length of the Fermi arc, would be. This is then compared to experimental values. One constraint is that the arc length is set to be the same at both temperatures. Away from the arc, the gap was assumed to have a temperature dependence, and for simplicity, the temperature dependence at each momentum was assumed to be the same. The test gap function at 95K was found by fitting data away from the arc. It was found that multiplying this gap function by 0.55 produced the best agreement with gap data at 106K. Both

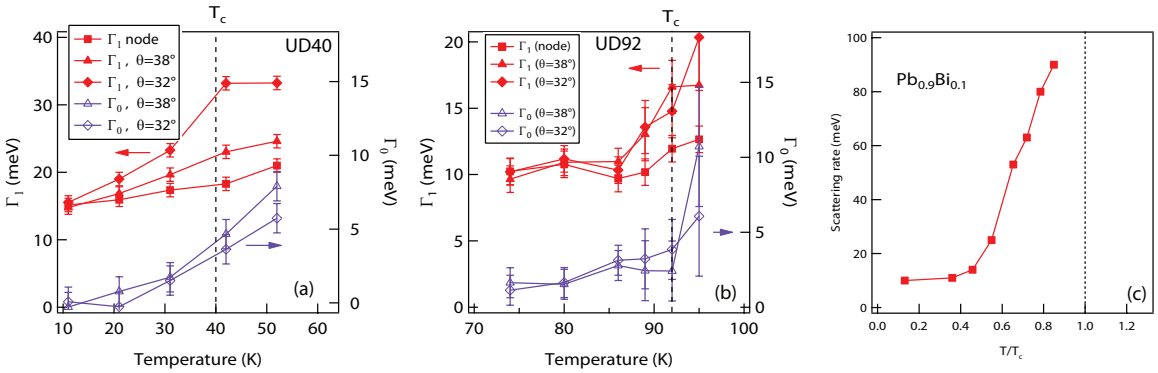

Figure 5.9: (a)-(b)Temperature dependence of fitted Γ_1 (left axis) and Γ_0 (right axis) at select momenta for UD40 (a) and UD92 (b). For comparison: scattering rates in $Pb_{0.9}Bi_{0.1}$ measured using SIS tunnel junction [116].

test gap functions are shown in Fig. 5.10(a).

Table 5.1: Norman model lineshape parameters from UD92 used in simulation.

Temperature	Γ_1 (meV)	Γ_1 (meV)
95	18	4
106	23	8

This simulation found that a real arc extending to $0.5 * |\cos(k_x) - \cos(k_y)| = 0.1$, is consistent with experimental data. This corresponds to an angular extent of 6° (out of 90°) or 7% of the length of a large Fermi surface. Note that these data are for the antibonding band, and the bonding band might give a slightly different result, depending on the origin of the arc. This sets a strong constraint on the length of a real Fermi arc.

The experimental data are also consistent with a 'nodal' gap function T>T_c with a single point where the magnitude of the gap is zero along the zone diagonal (Fig. 5.10(c)). This does not necessarily mean that it originates from superconducting fluctuations. Some proposals for the pseudogap, such as d-density wave order also feature nodes (but only at a certain value of the chemical potential) [117]. Notably, the nodal gap structure which agrees with data is smaller in magnitude than the gap in the superconducting state, indicating real temperature dependence approaching T_c.

One argument for the veracity of Fermi arcs is that quantum oscillation data are consistent with a pocket derived from short segments of near-nodal states and the reconstruction is caused by the recently reported charge ordering [109]. The correspondence between quantum oscillation and ARPES experiments relies on the field-induced resistive state being identical to the normal state above T_c. Sound velocity measurements suggest that a magnetic field stabilizes static charge order only at low temperatures [118], so there might be important differences between the $T>T_c$ normal state and the high-field resistive state. At this point, the ARPES data cannot distinguish between a nodal gap structure or small Fermi arcs, but it can set the upper limit of the arc length.

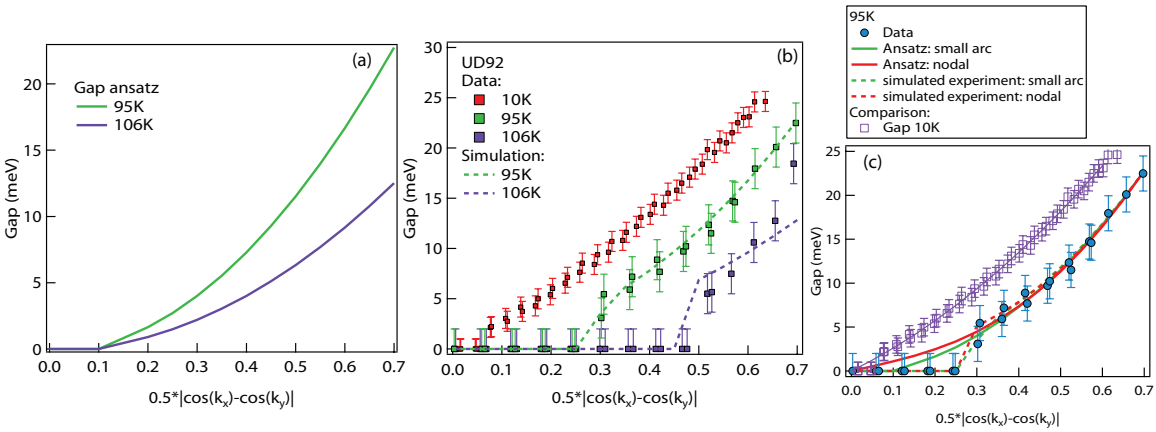

Figure 5.10: (a) input gap functions for simulation using lineshape parameters in Table 5.1 (b) UD92 data and simulated gaps and arcs. Zero gap is defined by a single peak in the symmetrized EDC, as in experiments. (c) Simulation at 95K: comparison of small arc and nodal gap function. Low temperature gap is plotted for reference.

5.4 Density of states at E_F

Fig. 5.11 shows the spectral loss function at the antinode, defined as $1\text{-}I_0/I_\Delta$, where I_0 is the intensity at E_F and I_Δ is the intensity at the EDC peak energy. This function is equal to 1 for a full gap and zero for no gap. It was introduced in Ref. [61], and we use it here to quantify the density of states at E_f. As with the Fermi arc length, there

appears to be two temperature regimes in the spectral loss function at the antinode. It decreases rapidly $T_c<T<T2$ and decreases less rapidly $T>T2$. Two temperature regimes of the antinodal DOS at E_F were discussed in Ref. [87], though the authors normalized to the total integrated spectral weight rather than the peak intensity.

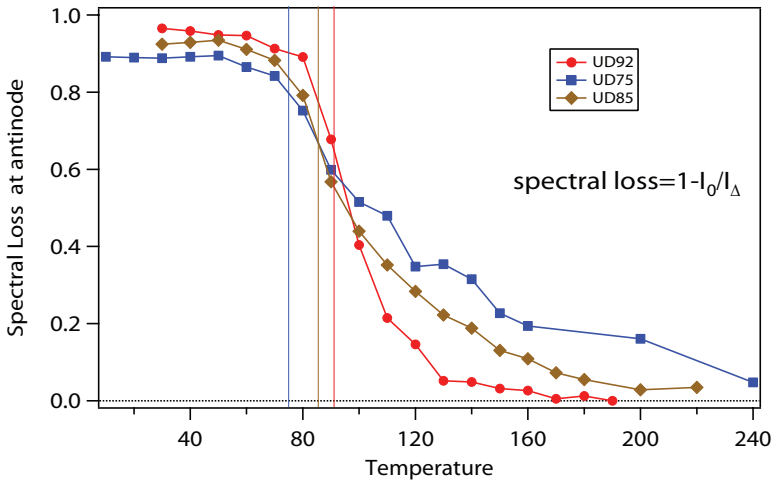

Figure 5.11: Spectral loss function at antinode for 3 dopings. Vertical lines mark T_cs.

5.5 Discussion: Relationship between pseudogap and charge order

Although it has long been speculated that short-range charge order may be the origin of the pseudogap, recent results were puzzling in that the charge order appeared to onset at temperatures lower than T* indicated by other experiments [112]. There appear to be two relevant temperatures. Below T_{CDW}, there is observable (but short range) charge order, T^2 resistivity [119], and a finite Kerr rotation [29]. Additionally, high field hall effect measurements show a signature at that temperature [76]. Below, T^*, a magnetic Q=0 neutron diffraction signal is observed [28] and the nernst coefficient becomes negative [31]. This is also the temperature where the antinodal gap opens in ARPES experiments on Bi-2212. Interestingly, some experiments such as resonant ultrasound [120] and possibly ARPES [110] show signatures at both T*

and T_{CDW}.

The relationship between the observed charge order and the pseudogap is an important and timely question [121]. One possibility is that the former represents fluctuations of the latter, as CDW fluctuations are observed above T_{CDW} even in more conventional charge density wave systems [122]. This is supported by the fact that the two phase boundaries seem to be rigidly offset from one another. Another possibility is that the pseudogap 'incubates' the charge order, creating an electronic condition where it can thrive. Finally, a somewhat less accepted proposal is that charge order and pseudogap are distinct and unrelated phases. The distinctness of the pseudogap and charge order has some empirical support. First, the pseudogap is a general phenomenon observed over a wide doping range, whereas charge order has only been seen near 1/8 hole dopings, and has explicitly not been observed far from this doping regime [111]. Additionally, recent STS experiments show that in Bi2201, a signature in the QPI pattern which is associated with charge order disappears at a doping far smaller than the doping where the pseudogap vanishes [123]. On the other hand, if the CDW ends in a quantum critical point, its fluctuations would appear over a broad

What does ARPES have to say about this? It appears that T* represents the gapping of the antinodal region, and T2 or T_{CDW} represents the gapping of most of the rest of the Fermi surface. However, as Ref. [87] and Fig. 5.11 showed, the density of states at E_F at the antinode starts to decrease more rapidly below T2, suggesting that these states are involved in the possible electronic reorganization which takes place below T2. However, the connection between T2 and T_{CDW} is still tentative, and additional data are needed to understand whether CDW and pseudogap are the same or different based on ARPES data in Bi-2212. Is there any significance to the temperature-dependent Fermi arcs terminating at the antiferromagnetic zone boundary at a temperature similar to T_{CDW}? Recent Hartree-Fock calculations for a metal with antiferromagnetic exchange indicated a susceptibility towards bond directional charge order as observed in scattering experiments [124] and pointed towards similar gap structure $T>T_c$ as seen in ARPES experiments.

5.6 Conclusions

In order to construct a theory based on ARPES experiments, every aspect of the pseudogap spectra must be considered: gaps, lineshapes, and DOS at E_F. Considering all three allows us to place the upper bound on the arc length at T_c as 7% of a large Fermi surface for UD92. At higher temperatures, the apparent 'growth' of the Fermi arc is at least partially an artifact from the increasing DOS at E_F. Our data are not consistent with a nodal metal ground state, as the arc length does not extrapolate to zero in the limit of zero temperature. There may be two temperature regimes visible in ARPES $T_c<Tleq T^*$, but this issue requires further investigation. If proven true, this may indicate that distinct spectroscopic signatures mark T^* and T_{CDW}.

Chapter 6

Low Energy Kink

One of the first discoveries made by laser ARPES was a kink at very low energy ($\omega \approx 10$ meV) in the nodal dispersion. This was reported by several groups in Bi-2212 [125, 126, 127, 128] and Bi-2201 [129]. Notably, the energy of this kink is smaller than the antinodal gap energy, indicating that its energy scale does not reflect a gap shifting. Most of the experiments discussed in this chapter were published in Refs. [126] and [130].

6.1 Introduction

In a d-wave superconductor like the high-T_c cuprates, the electronic component of thermodynamic quantities in the limit of zero temperature is dictated by the nodes, where arbitrarily small excitations are permitted by the gapless nature of these points. An intriguing aspect of cuprate phenomenology is the so-called universal nodal Fermi velocity (v_F) [131]. Along the nodal direction ((0,0)-(π,π)) the velocity measured by ARPES within 50 meV of E_F appears to be independent of cuprate-family or the number of CuO_2 layers in the compound, and is also nearly constant across the phase diagram – from the undoped insulator, across the superconducting dome, and in the non-superconducting metallic state at a doping p>0.25 – even though other electronic properties vary significantly with doping [20, 132, 133]. In addition, this universal v_F, if combined with ARPES measurement of the near-nodal superconducting gap

(see Chapter 3), leads to apparent contradiction with thermal conductivity observed directly in transport measurements [134, 135], suggesting that crucial information about the nodal quasiparticles is still missing.

ARPES data can be represented as a convolution between the single-particle spectral function and the momentum and energy resolution of the experiment. Naturally, with the improved resolution of laser-based ARPES, the measured spectrum begins to approach the intrinsic spectral function, and finer structure can be revealed. The first two sections of this chapter presents the systematics of the low-energy kink by means of a doping-dependent study of underdoped Bi-2212. Afterwards, the momentum and temperature dependence of the low-energy kink is investigated in UD55.

A list of the samples studied is shown in table 6.1. Samples were cleaved in-situ at a pressure $<4\times10^{-11}$ torr to obtain a clean surface, and measured at 10K. Energy and momentum resolution were 3 meV and better than 0.005 Å^{-1}, respectively. All data are 7eV laser ARPES taken with cuts parallel to ΓY.

Table 6.1: Summary of samples studied for this chapter with their composition. Dopings determined from T_c via an empirical curve, $T_c=T_{c,max}*[1\text{-}82.6(p\text{-}0.16)^2]$, taking 96K as the optimum T_c for Bi-2212 [63].

Sample	Composition
UD40	$Bi_2Sr_2(Ca,Dy)Cu_2O_{8+\delta}$
UD55	$Bi_2Sr_2(Ca,Dy)Cu_2O_{8+\delta}$
UD65	$Bi_{2+x}Sr_{2-x}CaCu_2O_{8+\delta}$
UD75	$Bi_2Sr_2CaCu_2O_{8+\delta}$
UD85	$Bi_2Sr_2CaCu_2O_{8+\delta}$
UD92	$Bi_2Sr_2CaCu_2O_{8+\delta}$
OD80	$(Bi,Pb)_2Sr_2CaCu_2O_{8+\delta}$
OD65	$(Bi,Pb)_2Sr_2CaCu_2O_{8+\delta}$

6.2 Doping dependence

Doping dependence of v_F

Fig. 6.1(a)-(c) show ARPES image plots for nodal cuts at three dopings: UD55 (underdoped, T_c=55K), UD65, and UD92, corresponding to hole-dopings of approximately 0.088, 0.10, and 0.14. Standard momentum distribution curve (MDC) analysis–Lorentzian fits at fixed energy– is used to extract the band dispersions [136]. The energy distribution curves (EDCs)–intensity as a function of energy at fixed momentum– at k_F in Fig. 6.1(d) indicate that these spectra are ungapped, as the symmetrized EDCs [64] have a single peak at E_F.

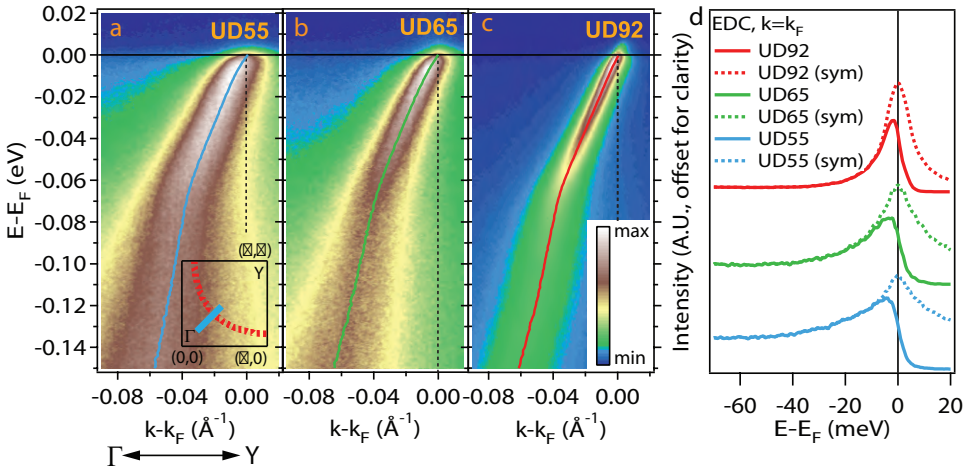

Figure 6.1: (a)-(c) False-color image plots of the nodal dispersion of UD55, UD65, and UD92, measured at 10K. Solid curves indicate band dispersions derived from MDC peak positions. Inset of (a): Brillouin zone schematic with Fermi surface indicated in red. The x-axes in (a)-(c) correspond to momentum along diagonal blue line ('nodal cut') in inset. (d) EDCs (solid) and symmetrized EDCs (dashed) at k_F. A single peak at E_F in the latter confirms that spectra in (a)-(c) are ungapped. k_F determined from Fermi crossing of dispersion (vertical dashed lines in (a)-(c)).

The systematics of the low-energy kink are studied via the MDC-derived nodal dispersion, which are plotted for three dopings in Fig. 6.2(a). In addition to the large, ubiquitous kink near 70 meV, a smaller kink is also evident: the dispersion within 10 meV of E_F deviates from the velocity fit between 30-40 meV. This deviation appears

more pronounced for more underdoped samples. The velocity (slope of the MDC dispersion) within 7 meV of E_F is *smaller* than the velocity at higher binding energy, notably opposite to the expected effects of instrument and thermal broadening [128]. We also note that the low-energy kink cannot be identified as an artifact due to a gap, because measurements are performed at the node where the superconducting gap is zero.

Another way to visualize the low-energy kink is via the real part of the electronic self-energy, ReΣ, plotted in Fig. 6.2(b)-(c). The low-energy kink is marked by a deviation of the slope of ReΣ at 6-10 meV from the slope established at E_F. For the sample closest to optimal doping, UD92, there is a single 'knee' in ReΣ. Meanwhile, the slope of ReΣ for UD55 and UD65 continues to evolve until 20-30 meV, possibly suggesting an additional kink, reminiscent of the 70meV kink, which may have several components [137, 138, 139]. From the Kramers-Kronig relation between ReΣ and ImΣ, a signature of the low-energy kink is expected in ImΣ, which is proportional to the MDC FWHM. In Fig. 6.2(d) we show that all dopings exhibit a downturn in ImΣ near E_F, though this is most pronounced for UD92. For more underdoped samples, the larger linewidth and possible additional kink make it more difficult to get quantitative information from ImΣ, but the observation that ImΣ decreases more rapidly close to E_F remains robust. The appearance of a low-energy feature in both ReΣ and ImΣ strongly argues against a trivial origin for the low-energy kink, and the phenomenology reported in Fig. 6.2 is reproduced in the other samples in our study. Thus, the systematics of a new energy scale can be added to the hierarchy of multiple energy scales in the cuprates [140].

The ubiquity of the low-energy kink in UD Bi-2212 leads us to reexamine previous measurements of v_F, as there is now compelling evidence that quasiparticles very close to E_F experience a heretofore unconsidered mass renormalization. The nodal v_F is plotted in Fig. 6.3, and our key finding is that v_F is not universal, but rather, has a pronounced doping dependence in the regime of this study. To characterize our data, at least two velocities are needed: v_{mid}, the linear fit between 30-40 meV, and v_F, the velocity fit between 0-7 meV, as defined in Fig. 6.2(a). These energy ranges are chosen to get sufficient data points while avoiding the low-energy kink

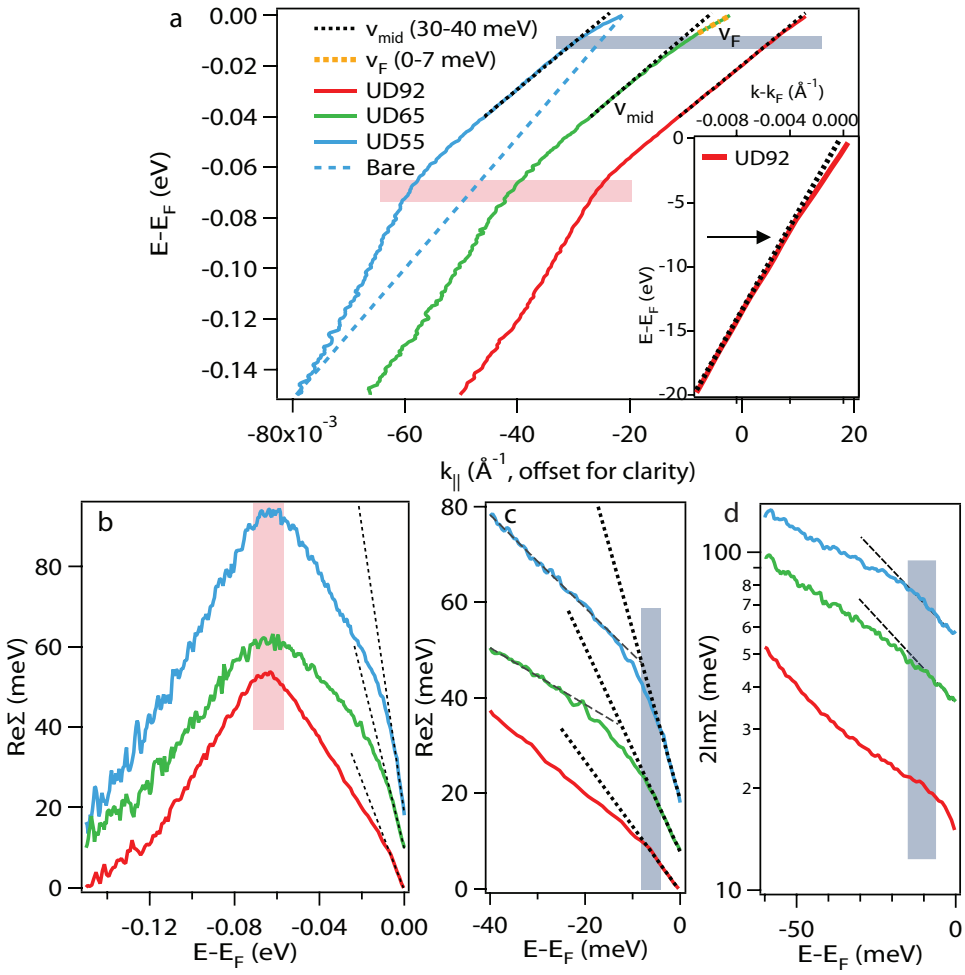

Figure 6.2: Systematics of low-energy kink. (a) Band dispersions from Fig 6.1, offset for clarity. Dashed line accompanying UD55 denotes assumed linear bare band. Black dotted lines are linear fits 30-40 meV (v_{mid}), extrapolated to E_F. This differs from v_F (fit 0-7 meV), indicated on UD65 dispersion by orange dashed line. Pink bar marks 70 meV kink, and grey bar marks low-energy kink. Inset: UD92 dispersion below 20 meV. (b) ReΣ, approximated by subtracting a linear bare band from dispersions in (a). (c) Detail of the low-energy portion of ReΣ. Thick dotted lines are fits near E_F. (d) 2ImΣ, with dotted lines as guides-to-the-eye.

and 70 meV kink. v_{mid} is found to be approximately 1.8 eVÅ, without a distinct doping dependence, consistent with the previously reported 'universal' value [131]. Meanwhile, *v_F decreases monotonically with underdoping*. The coupling strength of this low-energy renormalization can be roughly assessed by the velocity ratio v_{mid}/v_F,

which is plotted in Fig. 6.3(b), and indicating that coupling strength increases with underdoping. Notably, the ratio of velocities on either side of the 70meV kink exhibits the same doping dependence, though with the 70 meV kink, it is the higher energy velocity (ω>70meV) which is doping-dependent [131]. Although a doping-dependent v_F presents a significant shift from previous understanding of cuprate nodal physics, new results are not inconsistent with previous measurements: v_{mid} is indeed doping-independent, and inferior energy resolution can easily obscure subtle low-energy kinks near E_F. This finding underscores the importance of very low energy scales in these systems and revises cuprate phenomenology by linking nodal v_F to doping and T_c, previously suggested by the temperature dependence of the low-energy kink [128]. Further, this doping dependence constrains the origin of the low-energy kink, and may aid interpretation of bulk thermodynamic measurements, particularly thermal conductivity.

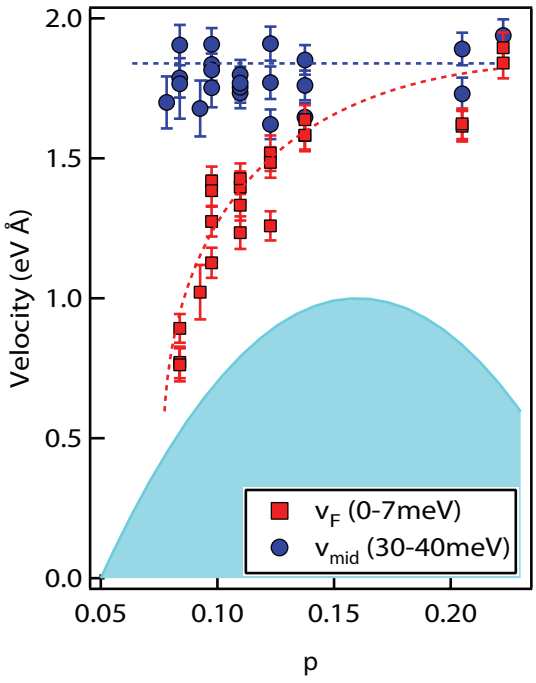

Figure 6.3: Doping dependence of v_F and v_{mid}. Boundary of shaded region denotes doping dependence of T_c.

Connection to thermal conductivity

For the cuprates, thermal conductivity near T=0 can be expressed in terms of two components of the Fermi velocity: the velocity perpendicular to (v_F) and tangential to (v_2) the Fermi surface (FS) at the node (Fig. 6.4(a)-(c)) [141, 142, 143]. v_2 is equivalent to v_Δ (Chapter 3), but is expressed in units of eV·Å instead of energy. For a two-dimensional *d*-wave superconductor in the clean limit, the residual linear term (T=0 extrapolation) of thermal conductivity, κ_0/T, is independent of the quasiparticle scattering rate, interaction energy, or other sample-dependent parameters [142, 144].

In this regime, κ_0/T is related to v_F and v_2 by a simple formula [141, 142, 144]:

$$\kappa_0/T = \frac{k_B^2}{3\hbar}\frac{n}{d}[\frac{v_F}{v_2} + \frac{v_2}{v_F}], \tag{6.1}$$

where n is the number of CuO_2 planes per unit cell, and d is the c-axis unit cell length. The second term is usually negligible, as $v_2 \ll v_F$. Thus, by measuring bulk thermal conductivity, one can extract a microscopic parameter, v_2/v_F, which fully determines the ground state nodal electronic structure of cuprates [143]. Thermal conductivity measurements on $La_{2-x}Sr_xCuO_4$ [145, 146], $YBa_2Cu_3O_7$ [146], $Bi_2Sr_{2-x}La_xCuO_{6+\delta}$,[147] and Bi-2212[134] have all shown that κ_0/T decreases with underdoping, implying that v_F/v_2 also decreases. However, using v_2 reported in Ref. [148] and a universal v_F, Sun *et al* argued that ARPES suggested a different doping dependence of v_F/v_2 [134]. Such contradictions have been attributed to disorder effects, such as electronic inhomogeneity [134] or disorder-induced magnetism [135], but previous analysis lacked a crucial component: a doping-dependent v_F.

We plot the ratio v_F/v_2 in Fig 6.4(e) alongside the thermal conductivity values reported by Sun *et al* [134]. The ARPES v_F/v_2 decrease strongly with underdoping, exhibiting a consistent trend with the thermal conductivity results for Bi-2212 as well as other cuprates. The ratio v_F/v_2 is approximately linear with doping until p≈0.20, but the most overdoped sample in our study, OD65, deviates strongly from this trend, which is an interesting topic for a future study. The v_F/v_2 derived from ARPES and thermal conductivity differ in absolute value.

The difference in absolute value in Fig. 6.4(e) is explored in Table 6.2. Although

the low-energy kink has not been reported for all of the compounds listed, the low-energy kink in Bi-2212 is weak near optimal doping, so the 'universal' value of v_F can be taken as a good approximation for all samples shown here. Thus, the ratio v_F/v_2 should be substantially determined by v_2, or equivalently, Δ_0. The ARPES value of v_F/v_2 in Bi-2212 compares well to the YBCO value derived from thermal conductivity. Bi-2212 and YBCO have similar T_c and v_2, and YBCO is a clean cuprate, so perhaps comparing to thermal conductivity measurements in YBCO is more valid [1]. The ARPES value of v_F/v_2 in Bi-2212 is about half of the values derived from thermal conductivity for LSCO and Bi2201. This is expected, because the superconducting gap in Bi-2212 is about twice as big. Compared to other compounds, the Bi-2212 a-axis thermal-conductivity value of v_F/v_2 is anomalously large. A potentially important consideration is that in-plane anisotropy of thermal conductivity has been reported in Bi-2212 ($\kappa_a \neq \kappa_b$) [134, 149]. The doping-dependent data in Ref. [134] were along the a-axis, which has a larger κ_0/T, but the discrepancy in absolute value of v_F/v_2 shown in Fig. 6.4 (e) may indicate that the b-axis may be the correct one to compare to ARPES. However, ARPES does not observe in-plane anisotropy of nodal single particle parameters (v_F and v_2), so the anisotropy in thermal conductivity must have a different origin, such as coexisting density-wave order [150]. Alternately, the difference in absolute value of v_F/v_2 may suggest that Bi-2212 deviates from the clean limit, at least as far as transport measurements are concerned.

Table 6.2: Compilation of v_F/v_2 from heat transport and Δ_0 (extrapolation of near-nodal gap to the antinode) from ARPES for different compounds, near optimal doping.

Compound	v_F/v_2	Δ_0 (meV)	Reference
Bi-2201	31	13.5	[147, 151]
LSCO	20	15	[145, 152]
YBCO	12	38	[146, 153]
Bi-2212	64 (κ_a)	35	[134]
Bi-2212	28 (κ_b)	35	[134]
Bi-2212 (ARPES)	15.5	35	[39, 126]

[1] Private communications with the group of L. Taillefer indicate quantitative agreement between κ_0/T from thermal conductivity in YBCO at v_F/v_2 from ARPES studied on Bi-2212

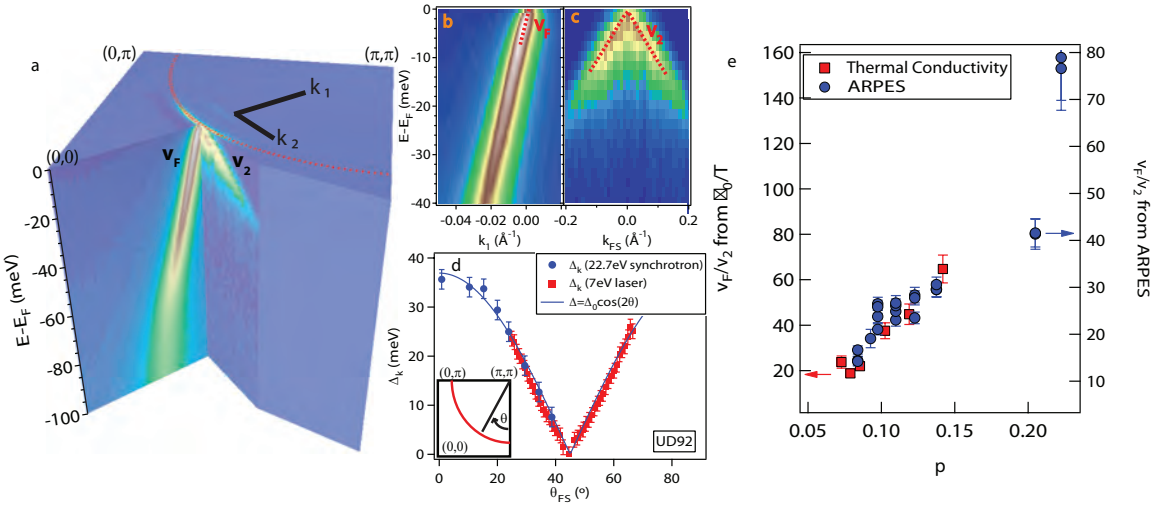

Figure 6.4: (a) Cutout showing FS (top) and dispersion perpendicular (v_F, left) and tangential (v_2, right) to FS at node, from measurement on UD92 at 10K. (b)-(c) Image plots showing measured v_F and v_2 directly. The latter image consists of EDCs at k_F from many parallel cuts near the node. (d) Comparison of synchrotron- and laser-based ARPES measurements of the superconducting gap of UD92 around the FS. When the data in (d) is fit to a simple d-wave form, $\Delta(\theta)=\Delta_0\cos(2\theta)$ close to the node, $v_2 \approx 2\Delta_0/k_F$, where k_F is the distance from the node to (π,π). (e) Comparison between v_F/v_2 from laser ARPES and thermal conductivity from Ref. [134]. Doping dependence is consistent, though absolute values differ.

6.3 Momentum dependence

The momentum dependence of the low-energy kink was explored in Ref. [130] as a collaboration between theory and experiment. This section follows that paper closely. Fig. 6.5 shows the nodal low energy kink in UD55. This sample was chosen to characterize the momentum dependence of the low energy kink because the renormalization is very pronounced. Away from the node, the superconducting gap will have signatures in the MDC dispersion, so a strong kink is necessary to distinguish renormalization effect from the gap. The nodal low energy kink is visible by eye in Fig. 6.5(a), along with the renormalization at 70meV.

The momentum dependence of the low energy kink is shown in Fig. 6.6. The energy where the MDC dispersion deviates from v_{mid} gets monotonically larger away

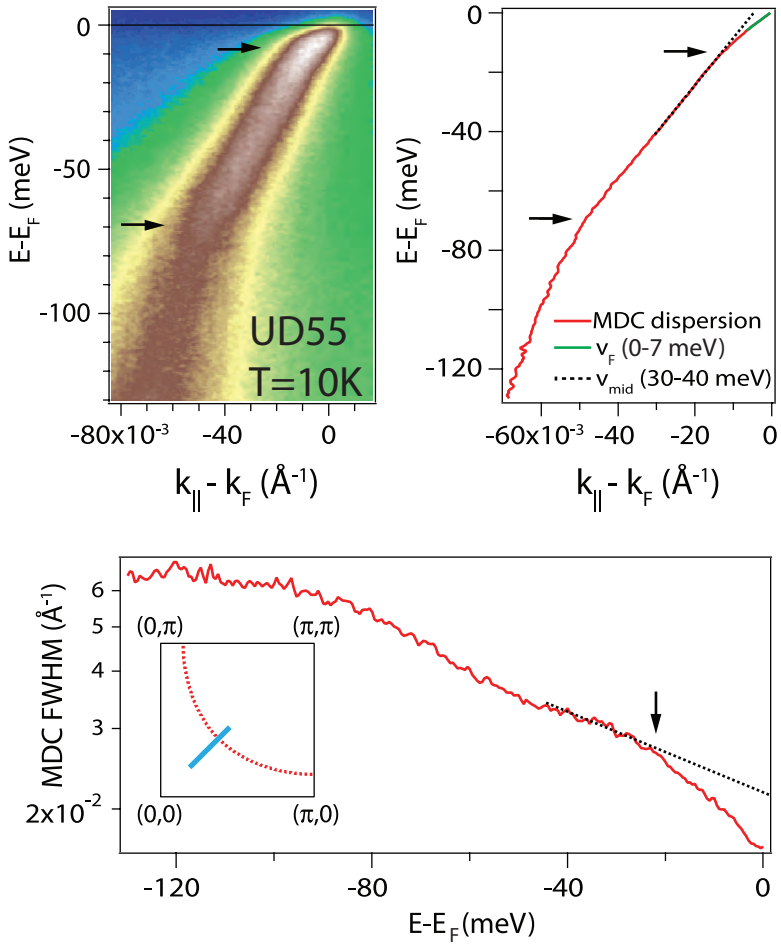

Figure 6.5: Low energy kink in UD55, 11K. (a) Color image plot of the raw data with both the low-energy and 70 meV renormalizations marked by arrows. (b) The band dispersion derived by fitting the momentum distribution curves (MDC) at each energy in (a) with a Lorentzian line shape. The low-energy renormalization is defined by the deviation of the dispersion from v_{mid}, the velocity fit between 3040 meV (dotted line). (c) The MDC FWHM which shows a more rapid decrease close to E_F.

from the node, following parallel to the momentum dependence of the superconducting gap. Thus, it appears that the low-energy kink only 'sees' the local gap at each momentum, and does not reflect the much larger gap at the antinode.

The hamiltonian for electron-phonon coupling in a single band can be expressed

as

$$H_{el-ph} = \frac{1}{\sqrt{N}} \sum_{\mathbf{k},\mathbf{q},\sigma} |g(\mathbf{k},\mathbf{q})|^2 c^{\dagger}_{\mathbf{k-q},\sigma} c_{\mathbf{k},\sigma} [b^{\dagger}_{\mathbf{q}} + b_{\mathbf{-q}}] \tag{6.2}$$

where $c^{\dagger}_{\mathbf{k},\sigma}(c_{\mathbf{k},\sigma})$ creates (annihilates) an electron with momentum $\mathbf{k}$ and spin σ and $b^{\dagger}_{\mathbf{q}}(b_{\mathbf{q}})$ creates (annihilates) a phonon of wavevector $\mathbf{q}$ and energy $\Omega_{\mathbf{q}}$. $|g(\mathbf{k},\mathbf{q})|^2$ is the electron-phonon coupling vertex which describes the momentum and wavevector dependence of electron phonon coupling, and its functional form depends on which phonon is being considered.

The vertex is related to the dimensionless electron-phonon coupling at each momentum, $\lambda(\mathbf{k})$ via

$$\lambda(\mathbf{k}) = \frac{2}{N} \langle \frac{|g(\mathbf{k},\mathbf{q})|^2 \delta(\xi_{\mathbf{p}})}{\Omega_{\mathbf{q}}} \rangle_{\mathbf{p},FS} \tag{6.3}$$

where $\delta(\xi_{\mathbf{p}})$ is the density of states at each momentum $\mathbf{p}$ on the Fermi surface.

Ref. [130] considered electrons coupled to acoustic phonon modes for which the electron-phonon coupling vertex reduces to a function of only momentum transfer

$$g(\mathbf{q}) = \frac{1}{V_{cell}} \sqrt{\frac{\hbar}{2M\Omega_{\mathbf{q}}}} \hat{e}_{\mathbf{q}} \cdot \mathbf{q} V(\mathbf{q}) / \epsilon(\mathbf{q}) = \frac{1}{v_{cell}} \sqrt{\frac{\hbar}{2M\Omega_{\mathbf{q}}}} \hat{e}_{\mathbf{q}} \cdot \mathbf{q} \frac{4\pi e^2}{\epsilon q^2} \frac{q^2}{1 + q^2_{TF}} \tag{6.4}$$

where V_{cell} is the unit cell volume, $\hat{e}_{\mathbf{q}}$ is the polarization of the phonon, $V(\mathbf{q})$ is the bare coulomb potential, and ϵ is the static dielectric constant. The momentum-dependent dielectric constant, $\epsilon(\mathbf{q})$ has been approximated by a Thomas-Fermi form, where q_{TF} is the Thomas-Fermi wavevector and expresses the screening length in momentum space. Neglecting the phonon dispersion, this expression for $g(\mathbf{q})$ is zero for $\mathbf{q}$=0, peaked at $\mathbf{q} \approx q_{TF}$, and is small for large $\mathbf{q}$. Metallic screening is poor in underdoped cuprates [154] which leads to a small q_{TF}, and thus, $g(\mathbf{q})$ is peaked at small $\mathbf{q}$ such that the low energy kink is gap shifted only by the local value of the gap at each momentum. Experimental results agree with calculations as shown in Fig. 6.6. These calculations also reproduce the doping dependence of the low-energy kink by considering doping dependence of q_{TF}.

Forward (small **q**) scattering can enhance $d_{x^2-y^2}$ superconductivity [155], so coupling to acoustic modes may increase T_c beyond the value set by the primary mechanism.

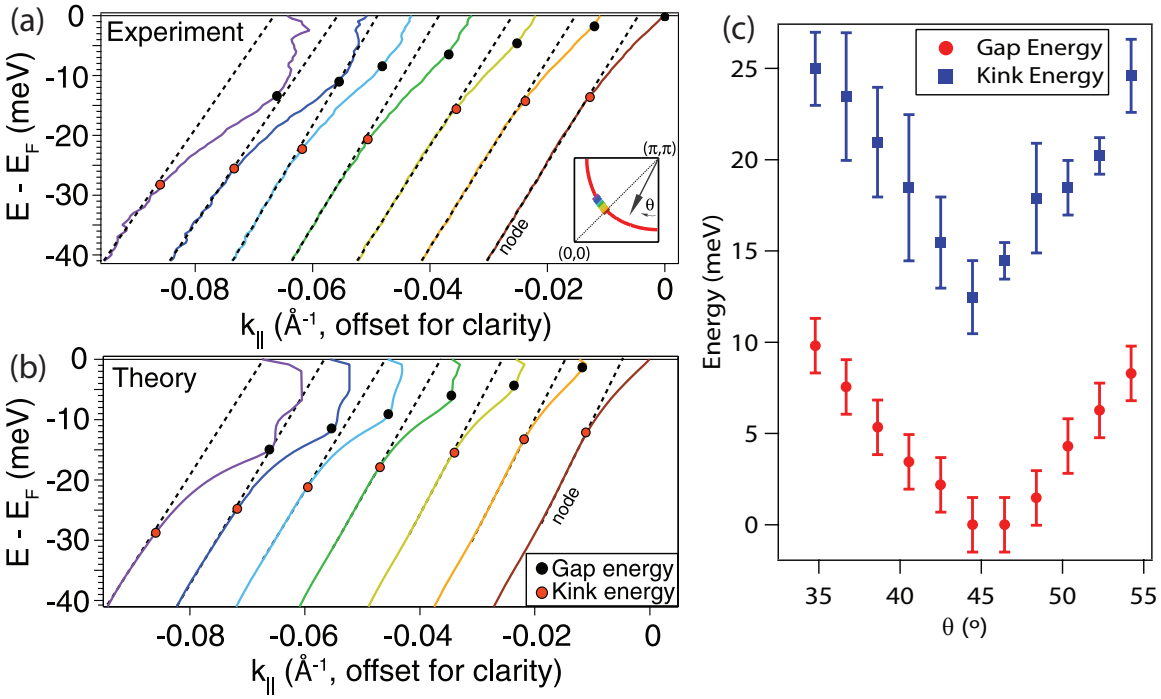

Figure 6.6: (a) MDC dispersions at the node (rightmost) and away from the node, offset horizontally for clarity. The black circles indicate the gap energy, determined by fitting symmetrized data to a minimal model [64]. The red circles indicate energy of the low-energy renormalization, determined from the deviation from v_{mid}. (b) MDC dispersions obtained from calculations in ref. [130]. (c) The momentum dependence of the gap and renormalization energies.

6.4 Temperature dependence

Experiments at optimal doping showed that the low-energy kink is substantially reduced above T_c [128]. We have studied the temperature dependence of the nodal kink in UD55 because T_c is 33% lower than the optimally doped sample and thermal broadening above T_c is proportionally reduced. Additionally, the kink is very robust at this doping. Fig. 6.7 shows the temperature dependence of ReΣ at the node for

UD55, with potential kink energy scales marked with vertical dashed lines. The 70 meV kink maintains its energy position across T_c which is well known. At low temperature, the low energy kink exhibits additional curvature which may be interpreted as two energy scales, but above T_c only a single kink energy of the low-energy kink is seen. Additionally, the low-energy kink weakens substantially across T_c These results are illustrated by defining velocities at strategic energy intervals, 0-5meV, 10-15meV, and 30-40meV, from the slope of the MDC dispersion at these energy intervals. The velocities between 10-15meV and 30-40meV become identical above T_c, indicating an absence of a kink in the energy range 10-40meV. The velocity 0-5meV remains smaller than higher energy velocities above T_c, indicating that the low-energy kink persists, although weakened.

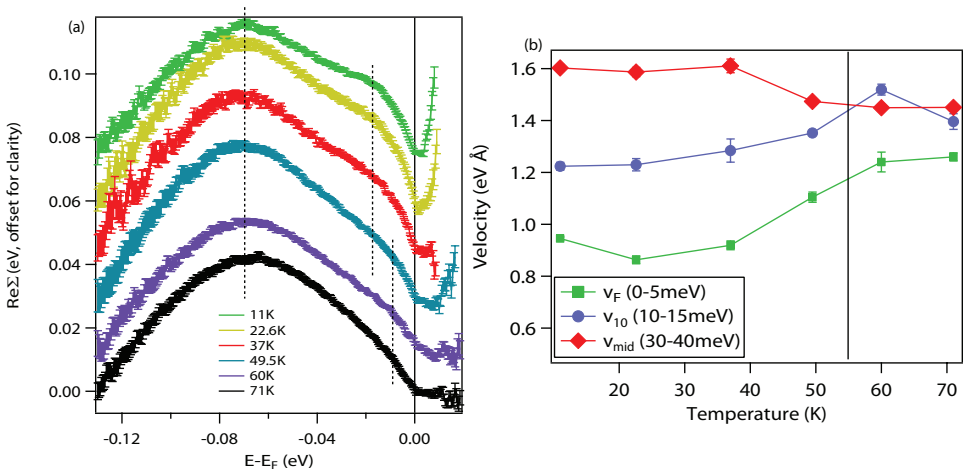

Figure 6.7: UD55: Temperature dependence of low-energy kink. (a) Temperature dependence of ReΣ determined from subtracting assumed linear bare band from MDC dispersion. Error bars are 95% confidence intervals from the fitting. Dashed vertical lines are guides-to-the-eye. (b) Slope of MDC dispersion at various energy intervals.

6.5 Conclusions

Laser ARPES has given unprecedented access to the node, and new physics was revealed in the Fermi velocity both orthogonal to (v_F) and parallel to (V_Δ) the Fermi surface at the node. The latter was the focus of the previous chapter, where

three distinct ground states were revealed, via distinct phenomenology of near-nodal gaps. The former was the focus of this chapter, where a new kink was revealed at very low energies, producing Fermi velocities which decrease with underdoping. Taken together, v_F and v_Δ can be used to make connections to bulk thermodynamic measurements in the superconducting state. The observation that the low-energy kink gap shifts by the *local* gap instead of the maximum gap indicates that it has distinct origin from the renormalization at 70 meV. Coupling to acoustic phonons can reproduce experimentally observed doping and momentum dependence.

Chapter 7

$HgBa_2CuO_{4+\delta}$ (Hg1201)

This chapter focuses on ARPES studies on $HgBa_2CuO_{4+\delta}$ (Hg1201), a cuprate whose structural simplicity and cleanliness makes it a model compound for certain types of experiments including charge transport and neutron scattering. In fact, it is becoming a model cuprate on par with YBCO for experiments where cleanliness is of utmost importance, such as observing quantum oscillations and gaining quantitative information from transport measurements [119]. The highest T_c ever was reported in a triple-layer cousin of Hg1201 [11], so in addition to offering general insight on the cuprates, Hg1201 may provide a materials-dependent perspective on how to maximize T_c.

However, the lack of a neutral cleavage plane makes it a difficult material to study with ARPES. This chapter summarizes the progress we have made in ascertaining the optimal experimental conditions to study Hg1201 with ARPES as well as our progress in understanding the near-nodal electronic structure of this material. A great body of ARPES studies exists for LSCO and Bi-2201, the 'low T_c' single-layer cuprates. Performing comparable studies on Hg1201 and $Tl_2Ba_2CuO_{6+\delta}$ (Tl2201), the 'high T_c' single layer cuprates, is crucial for discerning the electronic ingredients for higher T_c.

7.1 Experimental conditions

Hg1201 is considered a model cuprate because it has a simple tetragonal single-layer crystal structure (P4/mmm), and additionally, oxygen dopants are believed to be predominant in the HgO layer, far from the CuO_2 planes, minimizing disorder effects [156]. The crystal structure of Hg1201 is shown in Fig. 7.1. Notably, the crystal structure lacks a neutral cleavage plane, as there is nowhere to slice the crystal structure and achieve identical atomic planes on both sides at the cleave. Cleaving Hg1201 breaks the Hg-O bond, and the exposed surface includes both Hg and O termination.

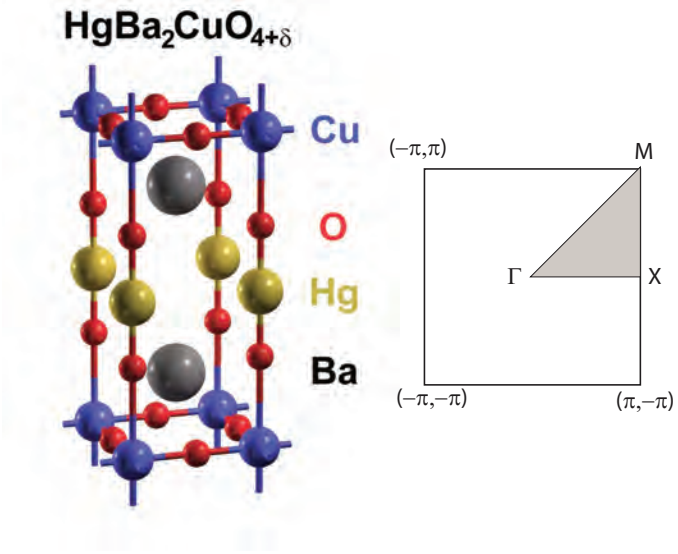

Figure 7.1: Crystal structure of Hg1201 (left). Image from Ref. [119]. 2D projection of tetragonal Brilliouin zone with high symmetry points labeled (right).

In preparing Hg1201 samples for ARPES experiments, care was taken to ensure conductance between the sample and the copper post. Samples were glued onto the copper post using EPO-TEK H21D silver epoxy (Epoxy technology Inc). While this silver epoxy provides adequate conduction between the copper post and most cuprates, Hg1201 samples were not found to be properly grounded to the post after this step. This may be due to the epoxy reacting with the Hg1201 surface. Thus, the silver epoxy provides only mechanical adhesion in our experiments. For conduction, a silver paint (Dupont) was applied to the side of the sample and the copper post

and cured at room temperature. Conduction between the top of the sample and the copper post was confirmed. Care was also taken to maximize the probability of a good cleaved surface. A pre-cut was made on the side samples using a wire saw, parallel to the a-b face. This was to ensure cleaving at a designated location, rather than at inclusions and imperfections as would be the tendency without a pre-cut.

Experiments were attempted with the 7eV laser, near 55 eV at beamline 10.0.1 of the Advanced Light Source (ALS), and near 19 eV at beamline 5-4 at SSRL. The latter experimental condition was found to yield the best spectra, and the quality of the measured spectra depended sensitively on the experimental conditions. Fig. 7.2 shows EDCs at k_F at the node taken with several photon energies between 18.6 and 19.6 eV. The amplitude of the quasiparticle peak relative to the background was found to vary sensitive with the choice of photon energy, even within this narrow range. Quasiparticle peaks were clear for 19-19.4 eV photon energy and very weak for 18.6, 18.8, and 19.6 eV photon energies. The nodal quasiparticle peak was found to be most pronounced for 19.4 eV photon energy and Γ-M cut geometry, so this experimental configuration was used for all data presented in this chapter. Note that because Hg-1201 is tetragonal, the M point is the Brillouin zone corner, and Γ-M cuts are along the (0,0)-(π,π) line.

Using this experimental configuration, electron states near the node are accessible, and cross section disappears approximately 25° away from the node. This is likely a matrix elements effect, and further exploration is needed to find an experimental configuration where the antinode has adequate cross section. Because, quasiparticles near the node are pronounced only within a limited range of photon energies, optimizing the experiment for the antinode may require ergodic exploration over parameter space. Fig. 7.3 shows momentum dependence of spectra on either side of the node. The band is most pronounced near the node in this experimental configuration, and spectral intensity diminishes moving away from the node. By 21°, a quasiparticle is no longer observed. EDCs at k_F are shown in Fig. 7.3(i). All spectra feature a strong energy dependent background, shown in Fig. 7.3(h), which is identical for all cuts in the Figure. Subtracting this background yields more pronounced quasiparticle peaks, as shown in Fig. 7.3(j). Similar methods have been used to discern spectral features

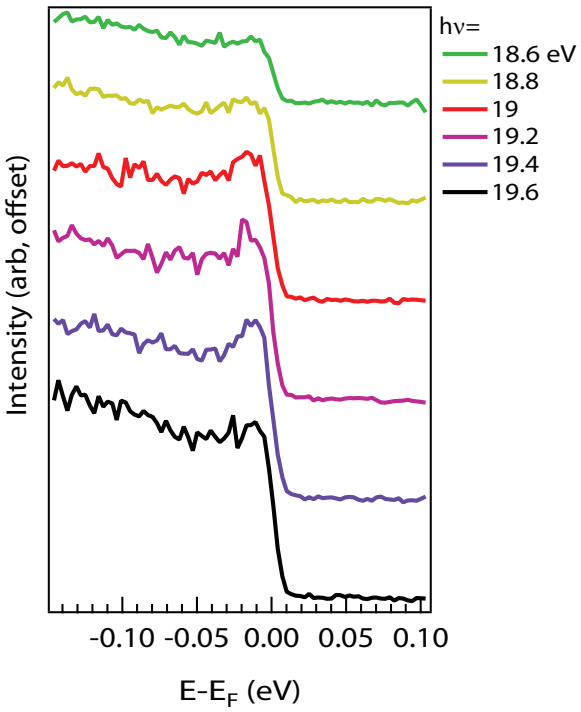

Figure 7.2: Photon energy dependence of nodal EDC at k_F. Data taken at SSRL with cuts parallel to Γ-M ((0,0)-(π,π) line) on a single cleave.

buried beneath a large background in other cuprates [157].

7.2 Momentum dependence

Fig. 7.4 shows a Fermi surface mapping and Fermi crossings for optimally doped Hg1201 taken with 19eV photons. Another experiment taken at 19.4eV yielded a similar Fermi surface. Data were taken on two opposite sides of the Γ point on either side of the node. Four-fold rotational symmetry was assumed in order to assess the positions of all near-nodal Fermi crossings in the Brillouin zone. Fig. 7.4 also shows

a tight binding Fermi surface

$$E_k = \mu + \frac{t}{2}(\cos(k_x a) + \cos(k_y a)) + t' \cos(k_x a)\cos(k_y a) + \frac{t''}{2}(\cos(2k_x a) + cos(2k_y a)) + \frac{t'''}{2}(\cos(2k_x a)\cos(k_y a) + cos(k_x a)cos(2k_y a)) \tag{7.1}$$

using the hopping parameters [158]

$$(t, t', t'', t''') = (0.46, -0.105, 0.08, -0.02) \tag{7.2}$$

The chemical potential μ was adjusted to fit the Fermi-crossings data (red and blue symbols in Fig. 7.4. This Fermi surface encloses a volume of $1.53\mathring{A}^{-1}$, which amounts to 13% hole doping, using 1+p=$2A_{FS}/A_{FS}$, where A_{FS} (A_{BZ}) is the area of the Fermi surface (Brillouin zone). This result is consistent with earlier reports [159]. The discrepancy between the nominal hole concentration (16%, optimal doping) and the Fermi surface volume may stem from the lack of observed Fermi crossings in the antinodal region. The exact shape of the Fermi surface is not known because the antinodal segments have not been accessed experimentally. Additionally, the lack of a neutral cleavage plane may play a role, making the hole concentration in the surface different from the bulk. However, it should be noted that the agreement between Fermi surface volume and nominal doping in the literature is mixed. In LSCO, the Fermi surface volume follows Luttinger's theorem within the accuracy of the experiment, while in Na-CCOC and Bi-2201 the FS volume increases with doping more rapidly [16, 160]. This has been associated with differences in how doping occurs in different cuprates. In LSCO, the chemical potential appears to be pinned inside the charge transfer gap, while in Na-CCOC and Bi-2201, the chemical potential shifts with doping. Additionally, recent x-ray absorption and Compton scattering experiments have indicated the breakdown of the single-band Hubbard model in LSCO with sufficient doping, suggesting that not all doped holes reside in the CuO_2 planes [161, 162]. Future doping-dependent ARPES studies of the FS volume in Hg1201 can clarify the interpretation of the FS volume observed in this

experiment.

With a favorable experimental configuration and a good cleave, we were able to measure the momentum dependence of the superconducting gap in Hg1201 using ARPES for the first time, as shown in Fig. 7.5. Background EDCs were subtracted in order to emphasize the quasiparticle for accurate extraction of the gap. Spectra were symmetrized and EDCs at k_f were fit to the Norman model convolved with the instrument resolution of the experiment (10.6 meV) [64]. Fitted gaps are plotted as a function of the simple d-wave form, $0.5|\cos(k_x)-\cos(k_y)|$, in Fig. 7.5. Extrapolating to the antinode, assuming the gap function obeys a simple d-wave form, gives an antinodal gap of 39±2 meV. This is similar to the antinodal gap observed in Bi-2212 by ARPES at optimal doping [32, 39]. For Hg1201, Raman shows a peak in the B_{1G} channel corresponding to a 31 meV antinodal gap [38], and tunneling experiments have reported a d-wave gap with a maximum of 33 meV [163].

7.3 Nodal dispersion analysis

Fig. 7.6 analyzes the MDC lineshape. Selected MDCs are shown in panel (a), and they have certain peculiarities which were observed in every experiment. First, the MDCs near E_F show deviation from a Lorentzian lineshape, with extra weight in the tails, such that the peak height and width cannot be simultaneously captured in a Lorentzian fit. Moving to higher binding energy, the MDCs become increasingly asymmetric, with extra weight on the side of the peak further from the Gamma point. Every sample studied showed the same asymmetry. Because of this MDC lineshape, using the usual fitting procedure of a Lorentzian peak on top of a constant background does not yield the correct peak position at higher binding energy when asymmetry is strong (Fig. 7.6(b)). Using a linear background for each MDC better reproduces the peak position. (Fig. 7.6(c)).

Fig. 7.7 shows MDC analysis at the node using both a constant (red) and constant+linear (blue) background. Both methods indicate dispersion anomalies near 50 meV and 200 meV, and they yield comparable low-energy dispersions (<50 meV). Using a constant background yields steeper dispersions at higher binding energy,

which is not physically correct because this fitting does not capture the maximum of each MDC. The dispersion slopes in three different energy regimes are summarized in table 7.1. The Fermi velocity (v_F) is found to be similar to but slightly larger than other cuprates at optimal doping [131]. The velocity at higher energy (v_{HE}, 80-180 meV) is strongly dependent on the fitting scheme, with a constant background giving a slope which is 25% larger. This discrepancy can lead to an overestimation of the mass renormalization at the ≈50meV kink. A linear background yields a mass enhancement factor $1 + \lambda \approx v_F/v_{HE}$=1.97. This is comparable to other cuprates near optimal doping [131].

Table 7.1: Slopes of portion of MDC dispersion, as defined in Fig. 7.7, in units of eV$\mathring{A}$. Error bars represent 2σ confidence interval of fitting.

	Linear Background	Constant Background
v_F (0-40 meV)	2.008 ± 0.0024	2.076 ± 0.023
v_{HE} (80-180 meV)	3.956 ± 0.064	5.612 ± 0.061
v_{HE2} (230-330 meV)	8.994 ± 0.623	16.890 ± 1.26
v_F/v_{HE}	1.97	2.70

The MDC asymmetry might reflect interesting physics, such as a momentum-*dependent* self energy, contrary to the usual assumption. This can arise from correlation effects, as recently investigated in sodium cobaltate [164]. However, given the lack of a neutral cleavage plane, surface electric fields might be responsible. In photoemission, the interaction between a photon and an electron of momentum $\mathbf{p}$ is given by $\hat{H}_{int} = -\frac{e}{2mc}(\mathbf{A}\cdot\mathbf{p}+\mathbf{p}\cdot\mathbf{A}) = -\frac{e}{mc}\mathbf{A}\cdot\mathbf{p}+\frac{ie\hbar}{2mc}\nabla\cdot\mathbf{A}$ where the latter expression makes use of the commutation relation $[\mathbf{p},\mathbf{A}] = -i\hbar\nabla\cdot\mathbf{A}$. Usually, $\mathbf{A}$ is assumed to be constant, and thus $\nabla\cdot\mathbf{A} = 0$, but if this assumption does not hold, asymmetric lineshapes can result [165].

Fig. 7.8(a) shows the real part of the self energy at the node, approximated by subtracting an assumed linear bare band, as indicated in Fig. 7.7(b). The peak of ReΣ is at 51meV. The MDC FWHM shows an inflection point at a similar energy, affirming data quality and confirming a mode-coupling feature at that energy. There is a small upturn in the FWHM approaching E_F, but this is within the error bars, and likely not significant. There was some sample-to-sample variation in the kink energy,

with another good cleave showing a kink energy up to 58 meV. Comparisons are made to Bi-2212 with a similar T_c (UD92). The magnitude of ReΣ is about half as small in Bi-2212, suggesting stronger electron-boson coupling in Hg1201. Additionally, the dominant kink energy is larger in Bi-2212, with ReΣ peaking at 66 meV. Fig. 7.5 indicates that the superconducting gap in Hg1201 is comparable to that in Bi-2212, which suggests that a bosonic modes of different energy are responsible for the kinks in the two compounds. For further comparison, optimally doped Bi2201 (T_c=33K, Δ=15 meV) has a multiple distinct contributions to the nodal kink, and the most prominent features appear at 70 meV and 41 meV [129].

The origin 50-80 meV nodal kink in cuprates is debated with some explanations favoring a phononic origin [139, 166] and others favoring a magnetic origin [167, 168]. We will consider the former first. For optical phonons, the kink will appear at an energy $\Omega+\Delta_0$, where Ω is the phonon energy and Δ_0 is the magnitude of the antinodal gap [169]. Thus, given a 39 meV extrapolated antinodal superconducting gap, the kink observed in Hg1201 between 50-58 meV would imply an optical phonon between 11-19 meV. Ref. [170] shows in-plane optical phonon branches with maxima at 14 meV and an enhanced calculated phonon density of states at a similar energy.

In neutron scattering, a magnetic collective mode has been observed $T<T^*$, whose energy range varies from 52 meV and 56 meV between $\mathbf{q}$=(0,0) and $\mathbf{q}$=(0.5,0.5) [171]. This energy is almost identical to the energy position of thekink observed with ARPES, and the presence of the mode above T_c agrees with literature on other cuprates that the nodal kink persists above T_c [172]. Additionally, analysis of optical conductivity data in Hg1201 yielded a bosonic "glue" energy between 50 and 60 meV [173]. However, dispersion kinks normally show up at the mode energy gap shifted by the maximum superconducting gap, except for special cases such as acoustic phonons. Studying the momentum dependence of the kink in Hg1201 indicates that the kink energy does not disperse away from the node (Fig. 7.9). The kink energy appears similar for all momenta, suggesting that at every momentum, the maximum of the *d*-wave gap–not its local value–is the relevant quantity.

7.4 Conclusions

Despite its lack of a neutral cleavage plane, Hg1201 is a crucial compound to explore with ARPES because of the wealth of high quality neutron and x-ray scattering and transport data on this compound. This chapter outlined our technical experimental progress (sample preparation procedure, cleaving procedure, ideal experimental conditions for taking near-nodal data) and measurement of basic electronic properties available in ARPES (superconducting gap, nodal kink energy and renormalization strength).

Experiments can be further improved by using a more controlled method to cleave the samples [174, 175], and by finding experimental conditions where the antinode has cross section. Higher photon energy experiments (hν>100 eV) may be promising for the latter goal. As an example, $PdCoO_2$ also lacks a neutral cleavage plane, and yields sharp spectra as expected from the low residual resistivity when measured with 120 eV photons [176] (see also Appendix C).

Ultimately, studies of Hg1201 may be very fruitful in addressing the question of 'what causes a high T_c?' via comparisons to other single layer cuprates. LSCO and Bi2201, the low-T_c single layer compounds have received substantial ARPES study, while Hg1201 and Tl2201 have been less studied by the technique, but notably, the latter has a neutral cleavage plane. All four of these compounds are accessible and practical for ARPES. With a comprehensive study, new and non-trivial features may be found in the electronic structure which distinguish the low T_c compounds from the high T_c ones.

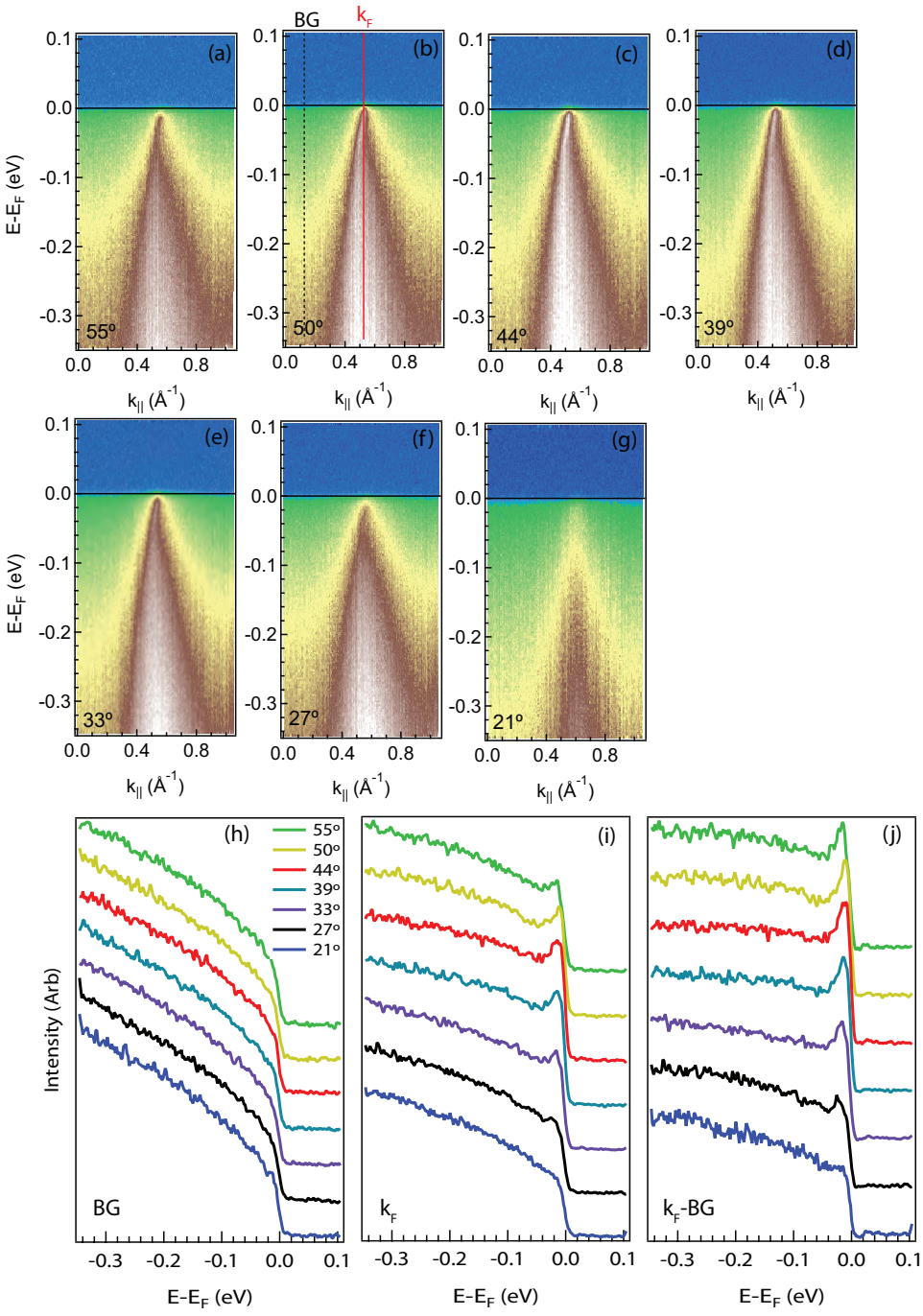

Figure 7.3: (a)-(g) Image plots of near-nodal cuts, with Fermi surface angle indicated in lower left of each panel. Data taken with 19eV photons, cuts parallel to ΓM, and T=10K. Red vertical line in (b) marks Fermi momentum (k_F) and black dashed line marks momentum where background EDC is taken for all cuts. (h) Background EDCs for all cuts. (i) EDC at k_F for all cuts. (j) EDC at k_F with background EDC subtracted for all cuts.

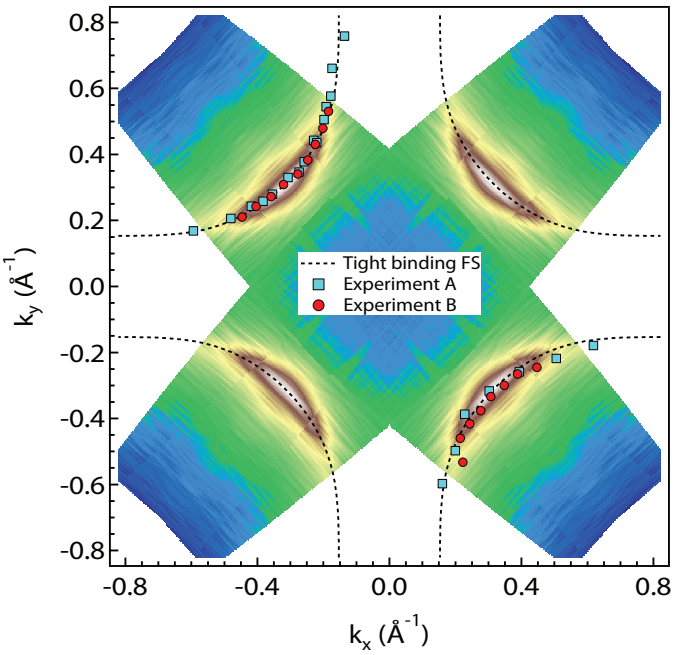

Figure 7.4: Fermi surface mapping from cuts in Fig. 7.3 constructed from integrated spectra within a 20 meV window centered at E_F. 4-fold symmetrization is applied. Red and blue symbols are Fermi crossings for two different experiments on two different batches of crystals. Fermi crossing is the peak position of the MDC at E_F. Experiment A taken with 19eV photons and experiment B taken with 19.4 eV photons. Dashed line is tight binding Fermi surface using hopping parameters in Ref. [158]

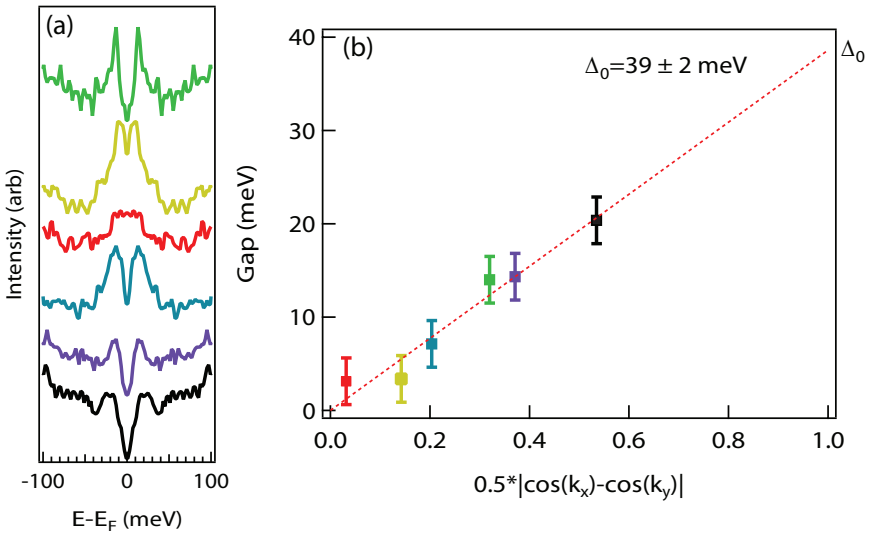

Figure 7.5: Gap measurements, 10K. (a) Symmetrized EDCs at k_F, using cuts in Fig. 7.3. Background EDCs has been subtracted. (b) Fitted gap at each momentum, plotted as a function of the simple d-wave form. Colors of EDCs in (a) correspond to colors of data points in (b). Dotted line is linear fit, fixing y-intercept to zero. Data were taken with 10 meV energy resolution

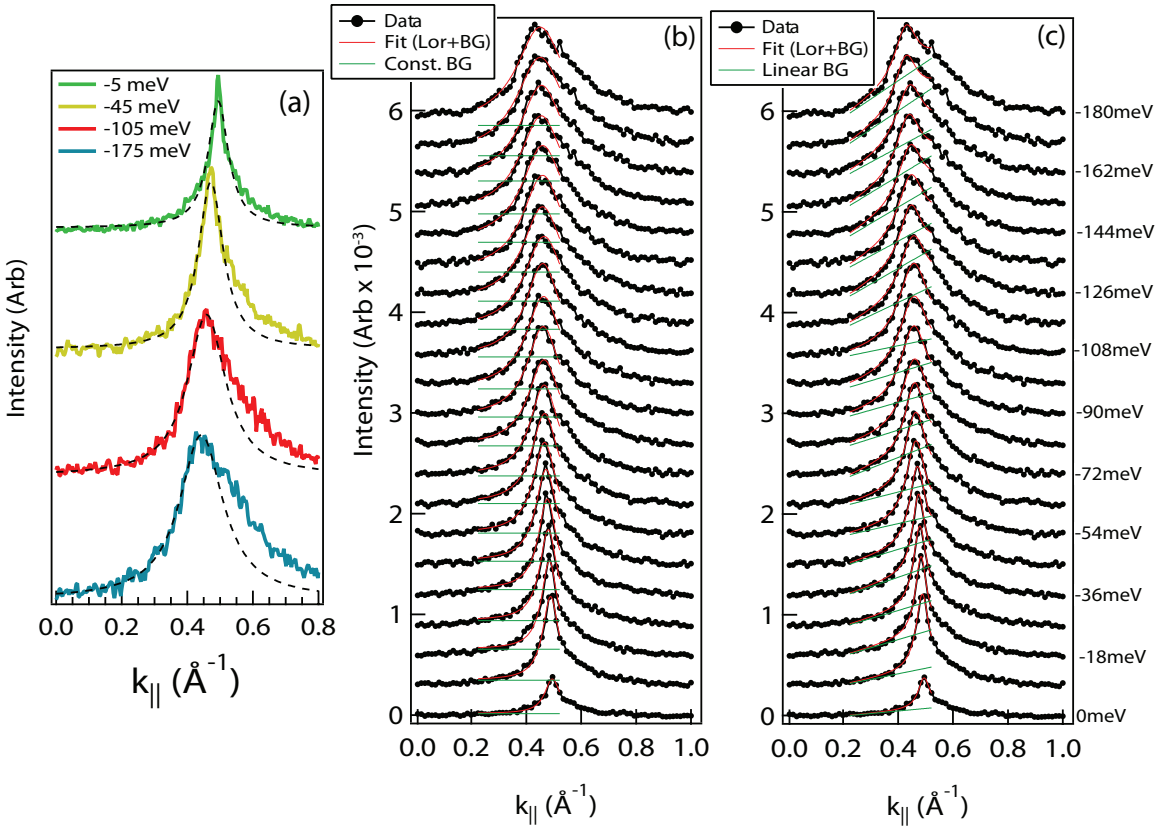

Figure 7.6: MDCs at node, 11K. Data taken with 19.4eV photon energy and 10 meV energy resolution.(a) Selected MDCs at indicated energies. Black dashed lines are lorentzian fits to the *left*-hand side of each peak. (b)-(c) Fitting of MDCs separated by 9 meV in energy to a lorentzian plus background (red curves). Green curves correspond to background, which is constant for (b) and linear (a+b$\mathbf{k}$) for (c). The left and right limits of the red and green curves indicate the momentum range of the fitting. Each MDC (black) is offset from the previous by 0.0003 (arbitrary units).

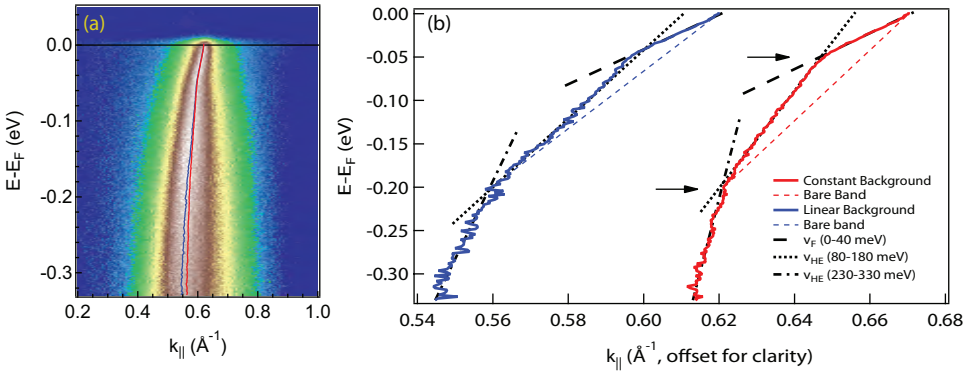

Figure 7.7: MDC analysis using constant (red) and linear (blue) background. (a) Image plot with MDC peak position from both fitting schemes. (b) MDC peak position dispersions, offset horizontally for clarity. Arrows mark key dispersion anomalies.

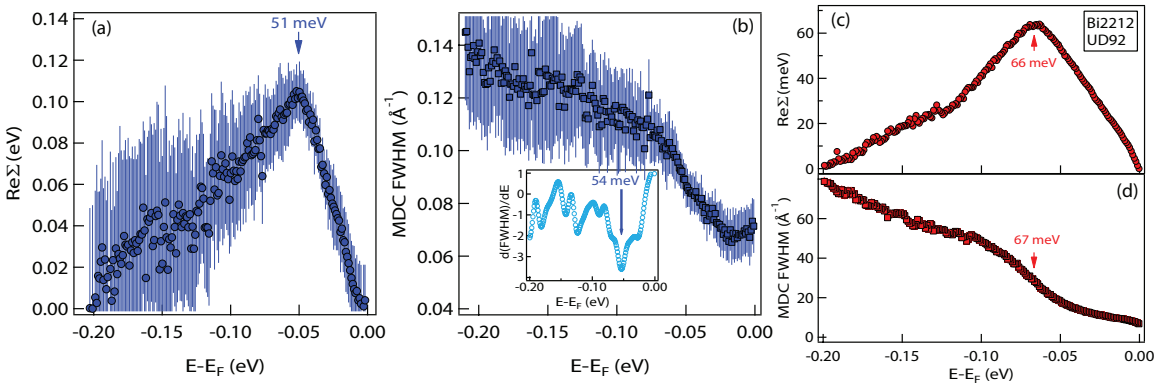

Figure 7.8: (a) Real part of self energy, using bare band indicated in 7.7. Arrow marks peak position. (b) MDC FWHM. Inset: derivative MDC FWHM (smoothed) with respect to energy. Arrow marks extremum. (c)-(d) Bi-2212 UD92 nodal kink analysis. Error bars smaller than marker size. (c) ReΣ. (d) MDC FWHM. Arrow marks minimum of first derivative.

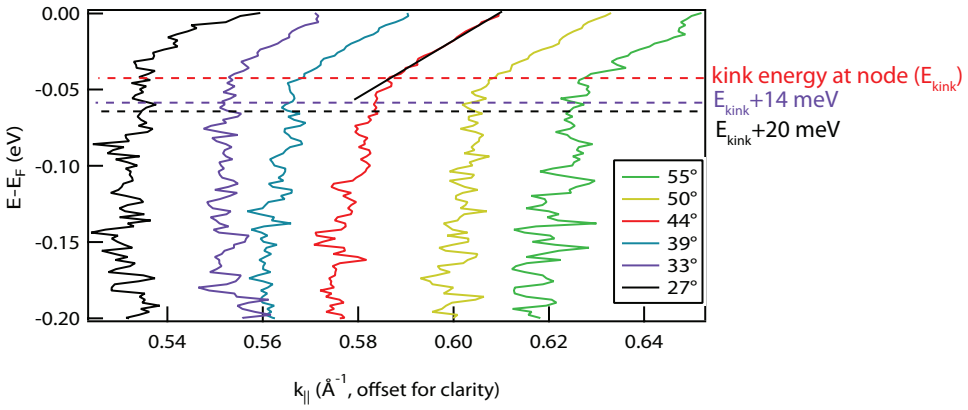

Figure 7.9: MDC analysis for data in Fig. 7.3. Dispersions offset horizontally for clarity. Red horizontal dashed line is approximate kink energy, as quantified by the energy where dispersion deviates from low energy linear dispersion. Purple and Black dashed lines are offset from red by 14 meV and 20 meV, respectively, reflecting the measured gaps at 33° and 27°, respectively.

Chapter 8

Conclusions and outlook

The 7eV laser has proved to be a tremendously useful tool, especially when it is used to study the model cuprate for the ARPES technique, Bi-2212. Although each of the parameters where the 7eV laser offers improvement over the synchrotron–energy resolution, momentum resolution, and photon flux–improves by less than an order of magnitude, their totality underscores the paradigm that new experimental technology leads to new discoveries.

One of the first discoveries made with the 7eV laser was the low-energy kink, and this is an important spectral feature for two reasons. First, its doping dependence allows to make correspondence between ARPES, a surface spectroscopy, and thermal conductivity, a bulk thermodynamics/transport experiment. There are often doubts about whether ARPES gives information about bulk properties of cuprates, and agreements like this help validate the technique. Secondly, a potential origin of the low energy kink, electrons coupled to acoustic phonons, may be a mechanism of enhancing T_c.

The resolution of the 7eV laser also afforded more careful study of gaps in the near-nodal region, a momentum regime which was previously neglected because of poorer resolution of earlier experiments. The lowest lying excitations near the node are relevant to ground state properties, and these experiments revealed three distinct phase regions inside the superconducting dome, separated by two phase boundaries which might be quantum critical points. With the laser, we could also resolve subtle

temperature dependence of gaps which showed that the pseudogap is not static below T_c, but rather, it is suppressed by superconductivity in a portion of the Fermi surface at low temperature. This is a crucial piece of information with which we can revisit conclusions drawn from earlier data.

The 7eV laser is supplemented by synchrotron experiments which allow access to the antinode and fine-tuning of photon energy. The former is generally important for the cuprates because pseudogap physics is strongest at the antinode, and the latter is a crucial prerequisite for studying Hg1201 which only yields acceptable nodal spectra at a precise experimental configuration. Although Hg1201 is not the easiest material to study with ARPES, we should continue to search for an experimental configuration which highlights antinodal states in that compound and also measure other dopings. A related line of inquiry is to study the other single-layer cuprate with a high T_c, Tl-2201. This has the advantage of a neutral cleavage plane, and it has not yet been explored with modern experimental precision. In my mind, this constitutes one of the last low-hanging fruits in ARPES studies of cuprates–even the superconducting gap has not been measured with the energy resolution standard in modern ARPES experiments (10 meV). Tl-2201 has the additional advantage of being naturally overdoped, and recent experiments have emphasized the overdoped side, to the degree that other cuprates can be grown overdoped.

Recently, we have demonstrated an 11eV laser for ARPES experiments, and once this system is optimized new discoveries will undoubtedly be made. The photon energy is sufficient to reach the antinode in the cuprates and the Brillouin zone boundary in other materials of interest such as the iron based superconductors and topological insulators. Other forthcoming upgrades include a new R8000 analyzer and 6-axis sample manipulator. With two bright narrow-bandwidth lightsources and improved resolution and angular acceptance we can find answers to many of the key questions in cuprates including the real momentum space structure (node? pockets? real arc?) of the pseudogap.

Appendix A

Appendix: Other gap analysis

A.1 Kordyuk Model

The spectral function model proposed by A. A. Kordyuk (Kordyuk model) may be more physical for the cuprates, and it is given by [114]:

$$\Sigma(\mathbf{k},\omega) = \lambda\omega + i\sqrt{(\alpha\omega)^2 + (\beta T)^2} \tag{A.1}$$

Where the band dispersion is approximated to be linear and λ is a velocity renormalization parameter. The $(\beta\mathrm{T})^2$ term behaves like Γ_0 in the Norman model in that it is nonzero in the limit that ω goes to zero at k_F. The single particle spectral function for the Kordyuk model, including a gap Δ opening at k_F, can be expressed as:

$$A(\mathbf{k}_F,\omega) \propto \frac{|\Sigma''(\omega,T)|}{(\omega-\Delta)^2 + (\Sigma''(\omega,T))^2} + \frac{|\Sigma''(\omega,T)|}{(\omega+\Delta)^2 + (\Sigma''(\omega,T))^2} \tag{A.2}$$

This is the expression that is examined in Fig. A.1 by varying β while keeping other parameters, including the gap, constant. β modulates the degree of thermal broadening, and when it is sufficiently large, the symmetrized EDC at k_F shows a single peak, analogous to the effect of Γ_0 in the Norman model. If one were to increase α in equation A.1, there would be additional weight at higher energy in the EDCs in Fig. A.1, but it would not contribute to the weight at ω=0, so an apparent gap would persist. In real data analysis, models including an energy-dependent scattering rate

tend to yield more unstable fitting, particularly near the node. For this reason, the Norman model is often a better choice for extracting the gap, which is why it was used in Ref. [39].

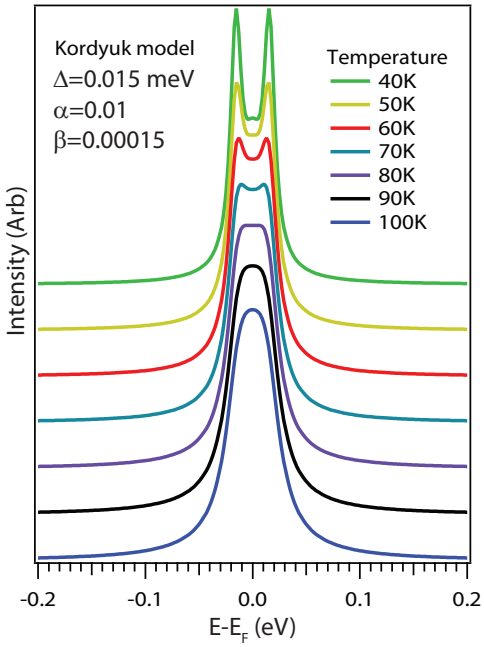

Figure A.1: Kordyuk model [114]: EDCs at k_F as a function of temperatures

A.2 tDOS

A new method of analyzing ARPES data has received attention in recent years [115, 177]. Tomographic density of states (tDOS) is a multistep procedure which aims to mitigate the ambiguities of resolving a small gap buried under a large scattering rate, as described in Chapter 5. The procedure is as follows:

1. Remove incoherent background and correct for detector nonlinearity
2. Integrate nodal cut over momentum in cut
3. Integrate off-nodal cut over momentum

4. Divide off-nodal integrated cut by nodal integrated cut to produce tDOS spectrum

5. fit to Dynes model to extract gap (Δ) and pair-breaking rate (Γ). $\rho_{Dynes} = Re\frac{\omega - i\Gamma}{\sqrt{(\omega - i\Gamma)^2 - \Delta^2}}$

The following two sections will show simulation and data to assess the differences between tDOS and traditional single-EDC ARPES data analysis.

A.2.1 tDOS simulations

Fig. A.2 shows simulation data using the Kordyuk model. The scattering rate ≈ 0.02 meV is more than twice the gap (4.5 meV) so that the EDC at k_F shows a single peak. However, the momentum integrated EDC shows a dip at zero energy indicating that a gap is present. The reason this information shows up in the integrated EDC (considering only E$<E_F$) is because of the backbending of the lower Bogoliubov branch k$>k_F$ which adds extra weight away from E_F.

Further simulation was used to assess the meaning of the 'pair breaking rate', Γ in terms of ImΣ input into different models of the spectral function. For simplicity, instrument resolution was not included in these simulations. Since the real spectral function of the cuprates is still debated, several scenarios are shown in Fig. A.3. The simplest model has $Im\Sigma = \Gamma = constant$, and this is shown in Fig. A.3(a). The gap is systematically overestimated in the tDOS fitting, but the severity is less pronounced when $\Delta > \Gamma$. A variation of this model involves a momentum-dependent Γ. For the values of Γ and Δ chosen, this approach gave poorer agreement between the tDOS fitting and the input, because Γ was always larger than Δ. The fitted Γ also differs from the input by several meV. However, this discrepancy is not as large as the difference between experimental the Γ found from tDOS analysis as compared to the EDC width from symmetrization [115]. Using the Kordyuk model as an input[114], tDOS fitting gives good agreement with the input model parameters (Fig. A.3(b)), except at the smallest gap values. A Fermi-liquid spectral function similarly offers good agreement at sufficiently large gap values.

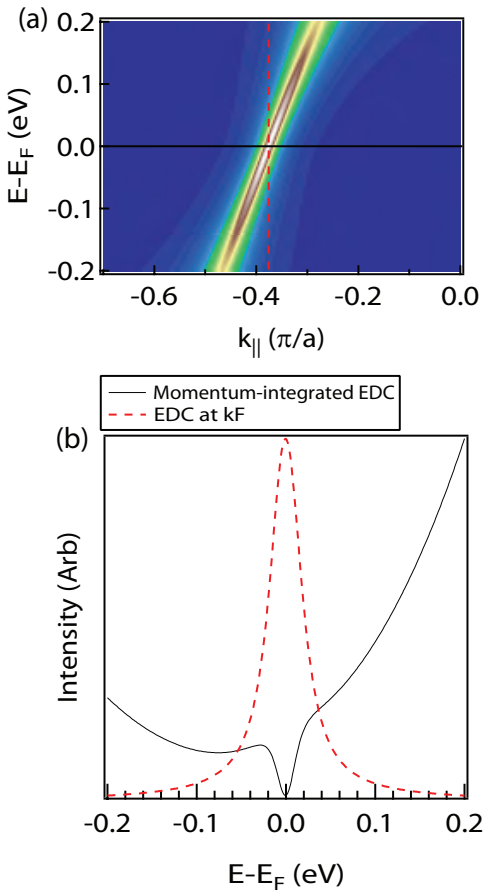

Figure A.2: (a) Simulated off-nodal spectrum, not including Fermi-Dirac cutoff. Kordyuk model parameters: $\alpha = 0.2, \beta = 0.002, T = 10K, \Delta = 0.0045$. Red dashed line marks k_F (b) EDC at k_F (red) and integrated spectrum (black). Integration range is entire k-range of (a).

A.2.2 Data: tDOS vs symmetrization

Figure A.4 shows EDCs at k_F and tDOS spectra at 12K and 77K for a UD65 sample. We note that our spectra were not corrected for detector nonlinearity, and the effect this has on the tDOS spectra is mostly on the unoccupied side as discussed in the supplements of Ref. [177]. At low temperature, both EDC and tDOS show structure by which a gap can easily be defined, though raw spectra have sharper peaks and hence a better defined gap energy. However, at high temperature, tDOS spectra near the node lack structure. For $\theta = 49°$, there is a subtle dip near E_F, but this

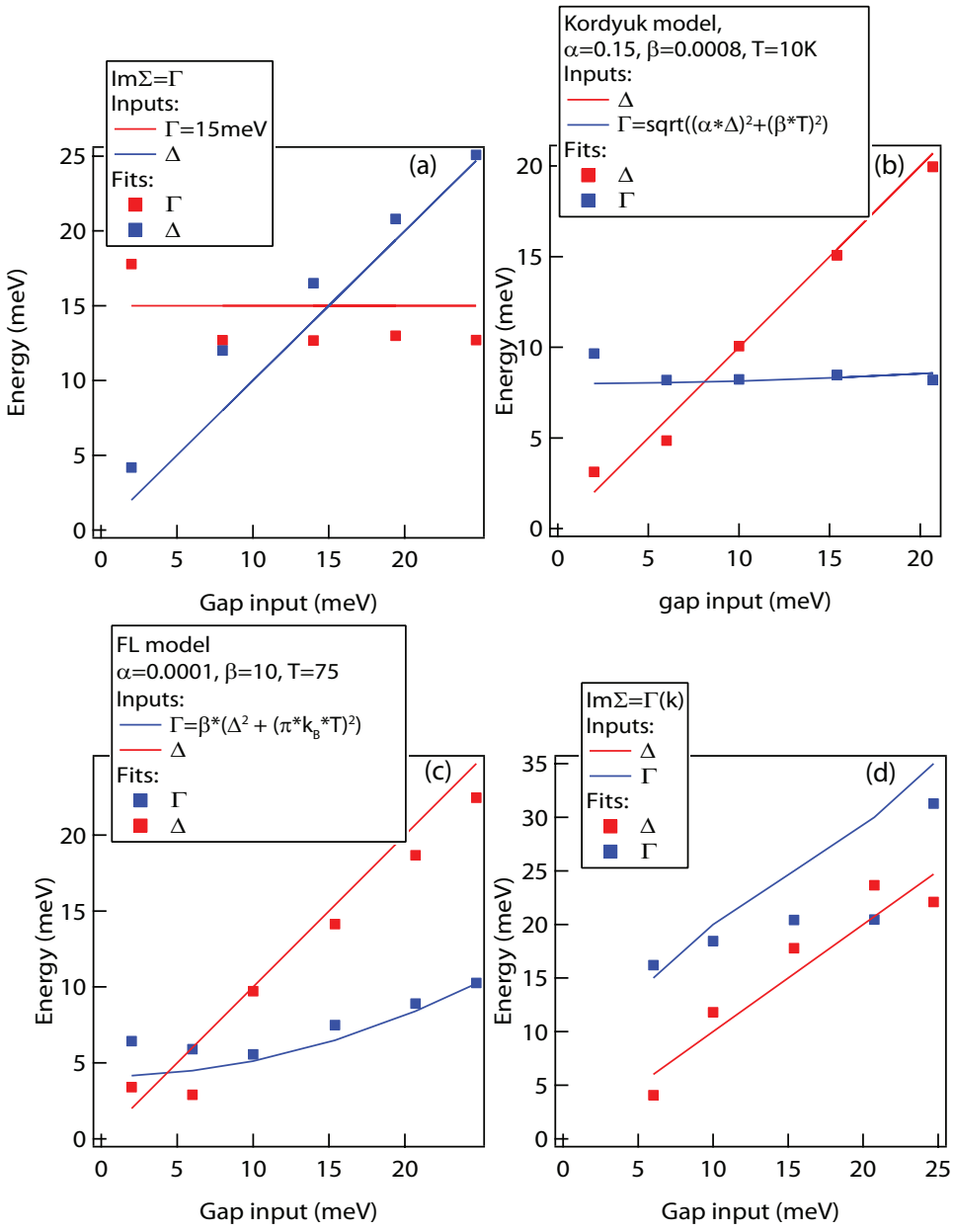

Figure A.3: Simulations of tDOS analysis for different models. Inputs in red and blue lines, fits shown in red and blue squares. Instrument resolution was not included in modeling. Gap (x-axis) is used as proxy for momentum position. (a) Constant $\Gamma = 15meV$. (b) Kordyuk Model. (c) Fermi-liquid spectral function. (c) Γ is constant for each cut, but increases for cuts away from the node.

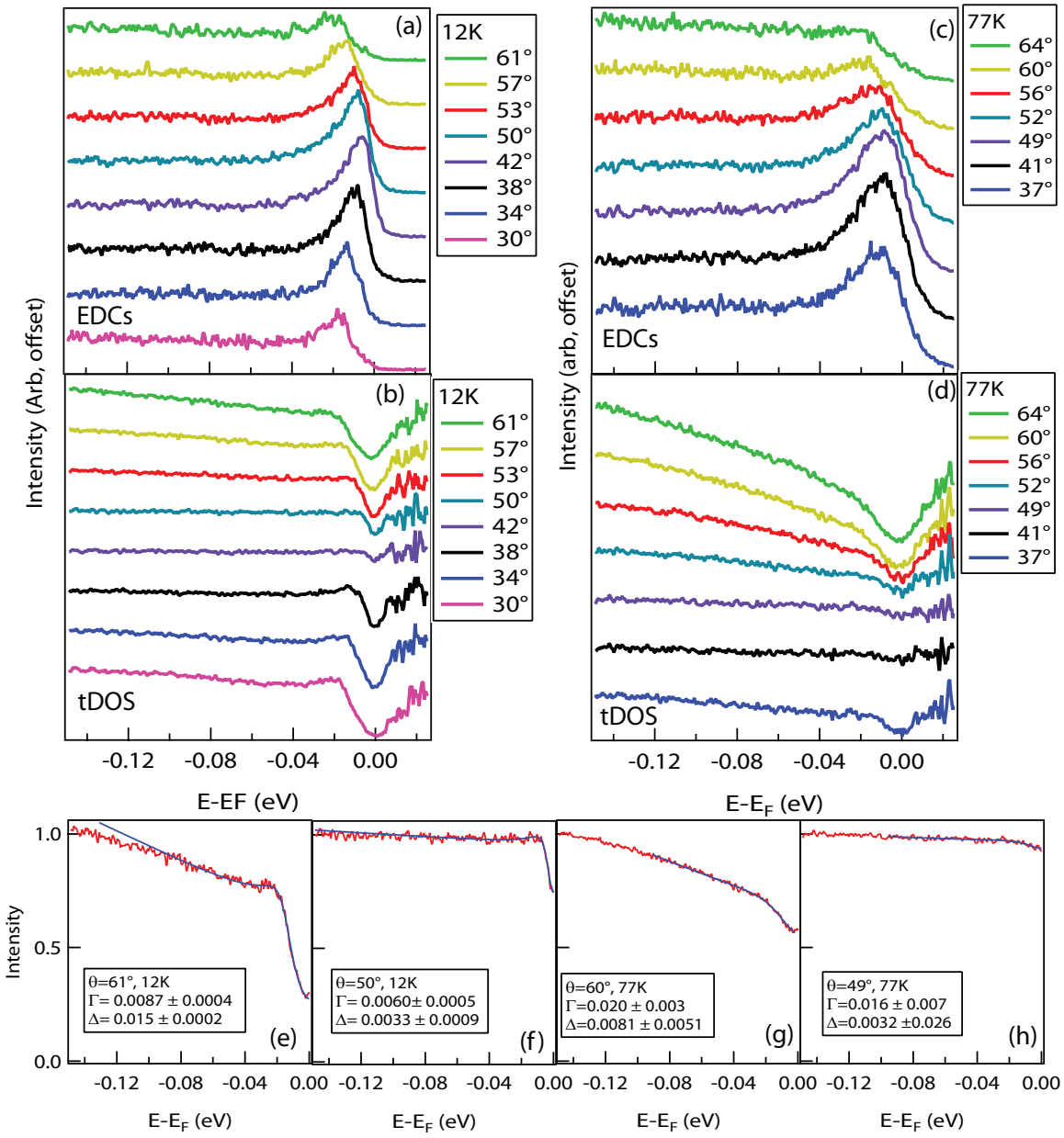

Figure A.4: Raw and tDOS spectra at selected cuts for UD65 samples. At the highest binding energy shown, tDOS intensities are equal to 1. (a)EDCs at k_F, 12K. (b) tDOS spectra, 12K. (c) EDCs at k_F, 77K. (d) tDOS spectra, 77K. (e)-(h) tDOS spectra (red) and Dynes model fits (blue) for selected cuts. (e) 61°, 12K. (f) 50°, 12K. (g) 60°, 77K. (h) 49°, 77K.

constitutes only 6% of the spectral weight. Thus, the fitted Δ and Γ have very large error bars.

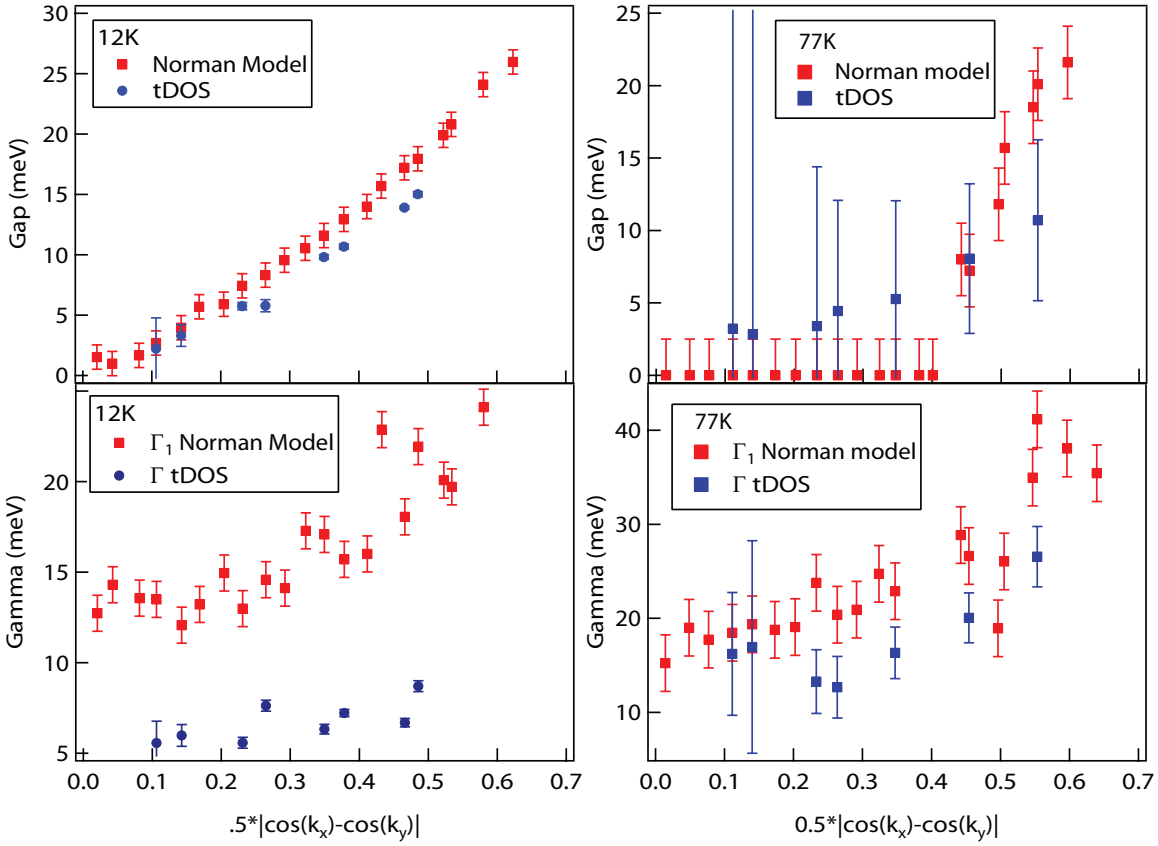

Figure A.5: Fits for UD65 sample. (a)-(b) Δ and Γ fit from Norman model (red) and tDOS (blue) at 12K. (c)-(d) 77K. Error bars for Norman model fitting determined by 3σ from fit ($\approx$ 0.5 meV at 12K, 1 meV at 77K) and uncertainty in fitting of E_F (0.5 meV at 12K, 1 meV at 77K). Error bars for tDOS determined from 3σ confidence interval fitting to Dynes model.

Figure A.5 compares Δ and Γ for Normal model fitting and tDOS spectra fit to the Dynes model. At low temperature, fitted gaps are comparable, though tDOS analysis yields consistently smaller gaps away from the node. The Γ from tDOS analysis is consistently smaller than Γ_1 from fitting symmetrized EDCs to the Norman model. At high temperature, particularly near the node, tDOS analysis yields giant error bars, because the spectra are so featureless. Thus, analysis method offers the

least quantitative utility in the regime where its necessity was motivated: when temperature is high and gaps are small. tDOS analysis very close to the node can suggest that a gap is still present, but it is more difficult to quantify the gap. In raw data, EDCs retain peaks from which gaps can be assessed less ambiguously. In that way, tDOS is similar to recent analysis of MDC integrated spectral weight at E_F [110]: they suggest that the Fermi arcs may be shorter than suggested by symmetrization analysis (or absent altogether), but cannot quantify the magnitude of the gap.

Because the high temperature tDOS spectra do not have well defined structure, choosing an energy range for the fitting can be ambiguous. Fig. A.6 explores how the fitted Δ and Γ vary with upper bound of the fitting for tDOS spectra in Fig. A.4(g)-(h). For the tDOS spectrum at $\theta = 49°$, the fitting range had little effect on the extracted parameters, and the statistical errors were always large. For the spectrum at $\theta = 60°$, there was an effect, with error bars being minimized for a fitting range of 50-70 meV.

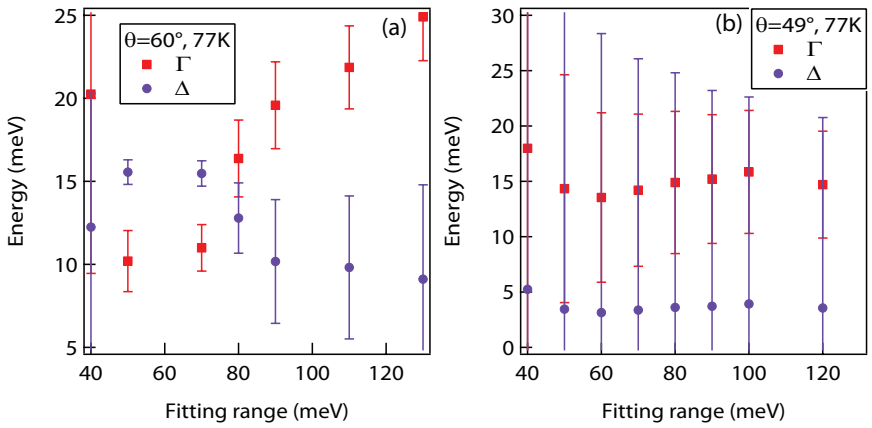

Figure A.6: Fitting range dependence for tDOS spectra in Fig. A.4(g)-(h). All fitting done only on occupied side with upper bound being E_F. (a) 60°, 77K. (b) 49°, 77K.

Figure A.7 compares temperature dependence across T_c between published tDOS analysis (Ref. [177]) and independent symmetrization analysis using laser ARPES. The T_cs are 85K and 83K, respectively. For $\theta \approx 62°$, the gap magnitude and temperature dependence are very similar. The gap decreases by $\approx 20\%$ approaching T_c. For For $\theta \approx 58°$ $(0.5^*|\cos(k_x) - \cos(k_y)| \approx 0.4)$ tDOS analysis yield a slightly smaller

gap. Symmetrization analysis yields a gap closing by $\approx 40\%$ across T_c while tDOS analysis yields a gap closing by $\approx 30\%$ across T_c.

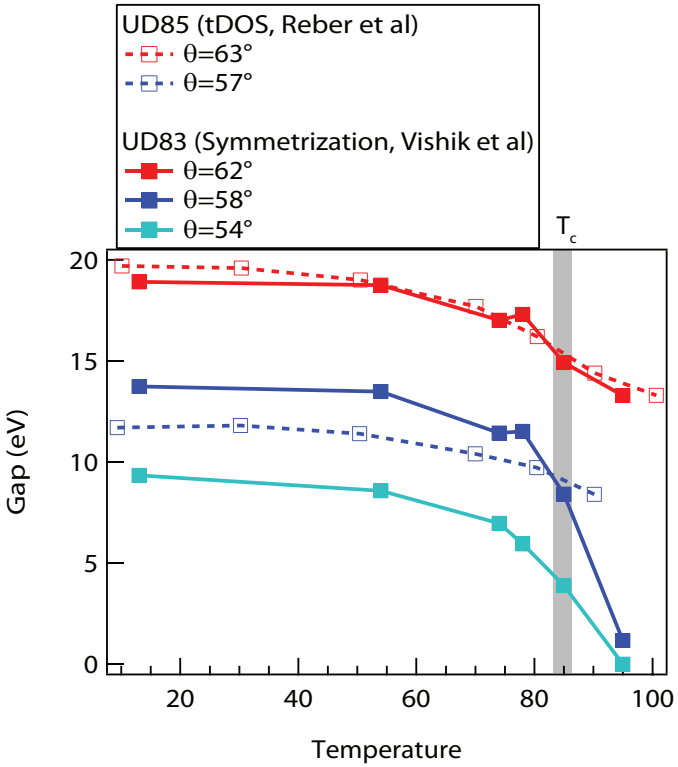

Figure A.7: Comparison of temperature dependence of gaps from symmetrization analysis and tDOS. tDOS analysis from Ref. [177] and data for symmetrization analysis are used in Chap. 3.

To summarize this section, tDOS appears to be useful for gaining qualitative information which is absent in symmetrization analysis: that a small gap is buried underneath a large scattering rate. This is similar to the information gained by analyzing the integrated MDC at E_F [110], though tDOS analysis can be done at a single temperature. However, in the regime where symmetrization fails–small gaps at high temperature–tDOS analysis is not useful for gaining quantitative information as the fitting has large statistical errors. In simulation for a variety of lineshapes, tDOS-analyzed gaps begin to differ from input values when the scattering rate is large relative to the gap.

A.3 Alternate analysis: Deconvolution

[1] A series of papers from the Brookhaven group used Lucy-Richardson deconvolution to analyze ARPES spectra, and the result was a nodal hole pocket whose volume decreased with underdoping and whose size was unchanged with temperature above T_c [178, 72]. Pockets are an attractive explanation for the pseudogap Fermiology because many theories can produce pockets without fine tuning. Refs. [178] and [72] discussed the analysis within a Yang-Rice-Zhang picture, but density waves would also produce pockets. It is difficult to get arcs or nodes without fine-tuning.

In principle, ARPES has some access to unoccupied states at elevated temperature, but in practice, this information is difficult to quantify as well as the occupied states. Above E_F, one needs to contend with detector nonlinearity, higher order reflections from the beamline grating and other accounted beamline light, and detector noise. The latter two are problems particular to the unoccupied side because the photoemission intensity is smaller there, and they both enhance the ARPES intensity on the unoccupied side. It is because of these factors that the photoemission intensity on the unoccupied side in Ref. [34] appears larger than on the occupied side after dividing by E_F. The authors of Ref. [34] are aware of this issue and did not attempt to quantify the intensity on the unoccupied side. Detector nonlinearity becomes an issue when one wants to compare signals over a wide dynamical range: depending how the experiment is done, either the low-intensity portion is undercounted relative to the high-intensity portion or vis versa. This can be corrected for by properly characterizing the detector in the experiment, as discussed in Ref. [179] for an earlier Scienta detector. Correcting for detector nonlinearity not a routine procedure for all ARPES groups because a correction is usually not needed if one only studies occupied states. The authors of Ref. [178] emphasize that they performed experiments in pulse-counting mode in order to better quantify the unoccupied states, but it is clear that the unoccupied states are being overcounted (supplements, Fig. S1(b)-(c)). In the superconducting state at k_F, the upper Bogoliubov peak appears to have a larger

[1] some of the information in this section comes from a presentation Makoto Hashimoto gave in a Superconductivity Subgroup meeting and discussions with Jonathan Sobota

amplitude than the lower Bogoliubov peak, which would not be the case if beamline noise and detector nonlinearity were corrected for. The deconvolution procedure seems to mitigate most of this, but it is not clear why, because this is not the purpose of deconvolution.

The main problem with Ref. [178] is that the argument relies on the truncation of intensity above E_F, which is a delicate issue to quantify. More clarity might be gained by analyzing raw data taken with superior energy resolution (1 meV, as afforded by a 7eV laser system and R4000 analyzer).

A.4 Future experiments

The conclusion one can draw from analysis from the Stanford, Colorado, and Brookhaven groups is that all analysis methods are limited in the regime where the gap is small and the scattering rate is large. One obvious way to mitigate issues of thermal broadening is to study cuprates where the pseudogap is accessible at low temperature. In Bi-2201, the pseudogap phase boundary extends beyond the superconducting dome and nonsuperconducting overdoped samples can be grown. Studying the pseudogap on the strongly overdoped side at low temperature can set limits on whether there are Fermi arcs (or pockets) and how large they are. One possible complication is that charge order appears to disappear much sooner than the pseudogap in Bi-2201 [123], so it might not perfectly reflect the physics of Bi-2212 and YBCO.

Additionally, experiments should continue to search for bending at the end of the Fermi arc, which would indicate a pocket. Analysis of quantum oscillation experiments suggest that the Fermi arcs might in fact be portions of electron pockets [109]. This requires taking cuts orthogonal to the usual direction (i.e. cuts parallel to ΓX when measuring in ΓY quadrant), and probably exploring a wider regime of matrix elements. With future upgrades to our analyzer and manipulator in the basement lab, it will be easier to explore this parameter space.

Appendix B

Appendix: Mode coupling, future directions

One of the difficulties in analyzing kinks in Bi-2212 is that there are six different entities existing at a similar energy scale (≈35 meV) near optimal doping: The superconducting gap, pseudogap, B_{1g} phonon, magnetic resonance mode, bilayer splitting, and the van hove singularity. In light of this complexity, there are two potentially fruitful approaches to assessing the origin of the prominent kink in the nodal dispersion:
1) Study the kink on the strongly overdoped side (p>0.22) where the pseudogap is absent at all temperatures
2) Systematically study the doping dependence of the kink, as the doping dependence of near-nodal gaps and antinodal gaps has been carefully characterized [39].
This appendix will first assess the cleave-to-cleave variation of the nodal kink and then show preliminary studies of the temperature and momentum dependence of the kink in OD65 where the gap closes across T_c. Finally, the doping dependence of the nodal kink and antinodal dip will be assessed in terms of recent studies of spectral gaps.
For most forms of electron-boson coupling, the dispersion kink appears at energy $\Omega+\Delta_0$, where Ω is the boson energy and Δ_0 is the antinodal gap energy. For example, in Eqn. 6.3 the electron-phonon coupling parameter (λ) at a given $\mathbf{k}$ is related to

the electron-phonon coupling vertex, $|g(\mathbf{k},\mathbf{q})|^2$, averaged over the *entire* Fermi surface. The discussion here will assume that the kink energy reflects gap shifting by the antinodal gap, rather than the local gap. For this appendix, ReΣ is approximated by subtracting an assumed linear band from the dispersion. While this procedure is only an approximation, it is extremely useful for assessing the energy position of mode-coupling features and tracking their momentum and temperature dependence, provided the same bare band is used for all data within the comparison. If not stated explicitly, the endpoints of the assumed linear graph are given by the range of the x-axis. The peak of ReΣ will be taken as "the kink energy".

B.1 Cleave-to-cleave nodal kink variation

There are two dopings that we studied frequently at low temperature: UD92 and OD65. For reference for future investigations, Fig. B.1 summarizes the kink energies observed in multiple experiments on OD65 and UD92 at low temperature. The energy position of the peak of ReΣ varies by about 8 meV for both dopings (4 meV if outlier is removed), and the kink energy for OD65 is consistently higher than UD92. This suggests that either a different mode dominates the kink in OD65 vs UD92 or there is a doping-dependence to the mode energy, because within a simple gap-shifting picture, OD65 is expected to show a kink at a *lower* energy for the same mode.

Several variables were investigated to understand the cause of the outliers in Fig. B.1: 1) v_F, 2) nodal renormalization, 3) MDC FWHM at E_F, 4) MDC FWHM at 100 meV, 5) ratio of MDC FWHM at E_F to MDC FWHM at 100 meV, and 6) maximum binding energy of cut. The first two were meant to account for the possibility that the cut was slightly off-node or did not intersect the node perpendicular to the Fermi surface. The third, fourth, and fifth variables were used to quantify cleave quality. In particular, a poorer cleave will yield broader low-energy spectra. The final criterion accounts for boundary condition problems that may arise in the data analysis. Preliminary analysis could not find links between most of these variables and an outlier kink energy. The only one which appeared problematic is the maximum binding energy of the cut. Future experiments should measure nodal spectra to at least 180

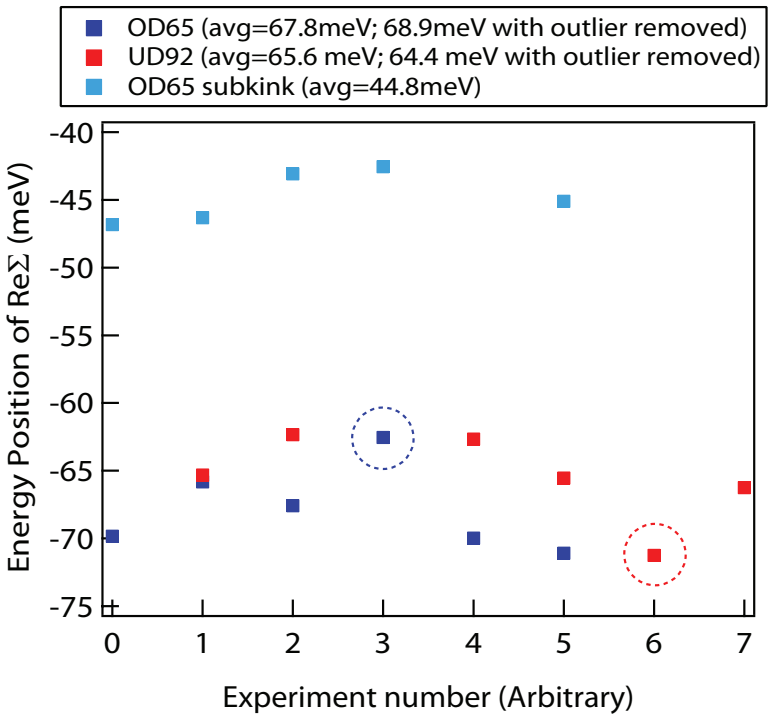

Figure B.1: Peak energy of ReΣ for all experiments on OD65 and UD92. Outlier is circled for each doping. For all experiments, temperature is well below T_c.

meV binding energy to permit reliable data analysis.

B.2 Kink in OD65

Recently, the overdoped regime has emerged as a promising venue for understanding near-nodal band renormalization [180, 181]. For data in this section, OD65 samples from two different batches were studied. The first batch were older samples stored in desiccant for 5 years. The newer batch were annealed in 2012. All OD65 samples contain Pb-doping on the Bi site, which is required to attain heavily OD samples which are stable.

Fig. B.2 shows the temperature dependence of gaps and ReΣ across T_c for OD65. At low temperature, the *d*-wave gap has a maximum of 17 meV at the antinode. The gap appears to close everywhere across T_c for this doping, indicating no pseudogap

above T_c. This reduces one variable when analyzing the temperature dependence of the kink. Below T_c, a kink is observed near 71 meV (peak of ReΣ) and another one is observed near 43 meV (shoulder of ReΣ). This is different from samples with smaller dopings (UD92, Fig. B.2(c)) where a clear shoulder is not visible at low temperature. Assuming gap shifting by the full antinodal gap, the kink and shoulder imply modes at ≈54 meV and ≈26 meV, respectively. Above T_c, there appears to be a single peak in ReΣ at 61 meV. This may correspond to the same mode giving rise to the main kink at low temperature, though higher-statistics studies are needed to verify the energy of the kink at each temperature. UD92 does not show a pronounced shift of the energy position of the main kink across T_c, as shown in Fig. B.2(c). Previously, the temperature dependence of the nodal kink and subkink in optimally doped Bi-2212 was interpreted in terms of a closing superconducting gap [137], but that analysis was complicated by the presence of the pseudogap above T_c. A similar approach can be applied to deeply overdoped samples, and it should be more rigorously correct in the doping regime where the gap closes over the entire Fermi surface at T_c.

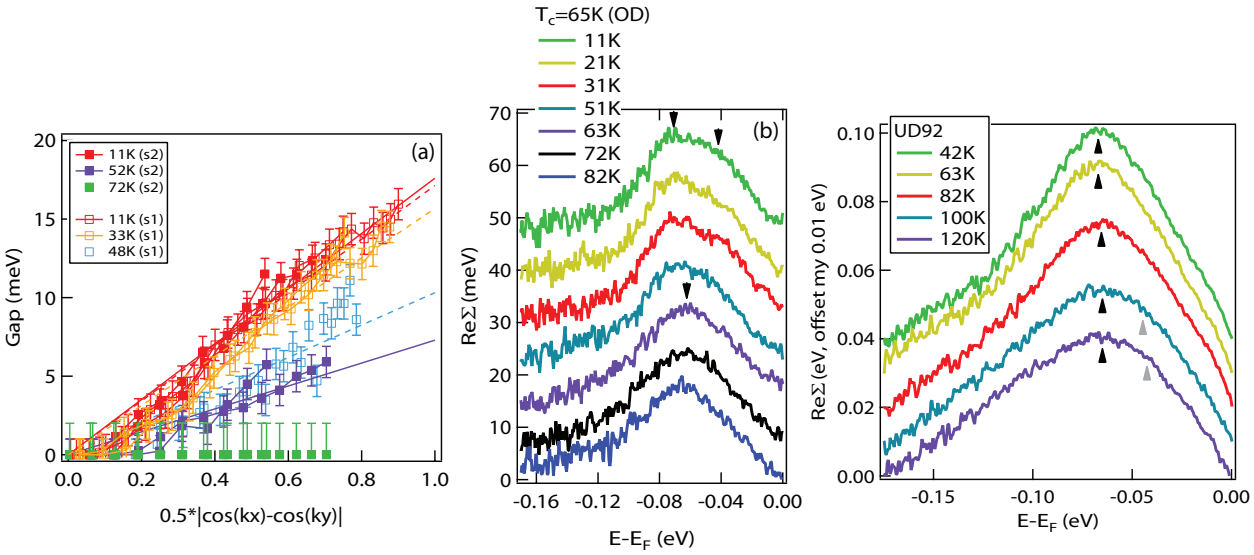

Figure B.2: (a) Gaps measured at several temperatures below and above T_c for two different OD65 samples (s1 and s2), from older batch. (b) Temperature dependence of ReΣ for OD65. Arrows mark kink and subkink. (c) Temperature dependence of ReΣ for UD92.

Fig. B.3 shows the momentum dependence of the kink and subkink in OD65. As in Fig. B.2, a main kink and subkink are observed. Additionally, these data show a low energy kink at ≈10 meV. This is not expected because the low energy kink was previously found to weaken substantially with doping [126, 127]. One explanation is that the OD65 sample is Pb doped, whereas samples in previous studies were not. It is possible that Pb may alter the dielectric properties of Bi-2212. Another possibility is that we do not understand the doping dependence of matrix elements sufficiently, and what looks like the low energy kink might just be the bonding band. This can be rigorously investigated at the beamline by varying the photon energy away from 7 eV. The spectra in Fig. B.2 were much broader than the spectra in Fig. B.3 such that the low energy kink, if present, may not be observable in Fig. B.2. In Fig. B.3, the relative weight of the subkink gets larger away from the node such that 16 degrees away from the node, the peak of ReΣ is near 40 meV instead of 70 meV. Two other dopings are shown for comparison: UD92 and OD80. Both of these samples show an apparent shift in ReΣ away from the node. However, there is no "two-mode" structure, and the magnitude of the shift between 45 degrees (node) and 29 degrees is 10 meV and 6 meV for OD80 and UD92, respectively. Approaching the antinode, the break between the quasiparticle portion of the spectrum ($|E|<|E_{kink}|$) and the incoherent portion of the spectrum ($|E|>|E_{kink}|$) becomes more pronounced and MDC analysis becomes less reliable [182]. Thus, the modest momentum-shift of the kink for OD80 and UD92 should be investigated further, employing both EDC and MDC analysis. Because two structures are clearly seen at each momentum in ReΣ for OD65, separated by 30 meV, this observation is probably robust. We note that a recent preprint has reported two distinct modes for an OD82 sample, near 40 meV and 80 meV with the lower energy one dispersing to lower energy approaching the antinode [180]. This was not observed in the OD80 data in Fig. B.3.

B.3 Doping dependence of kink

At the antinode, the dip energy is associated with mode coupling, gap-shifted by the antinodal gap. Two leading candidates to explain dispersion anomalies are the

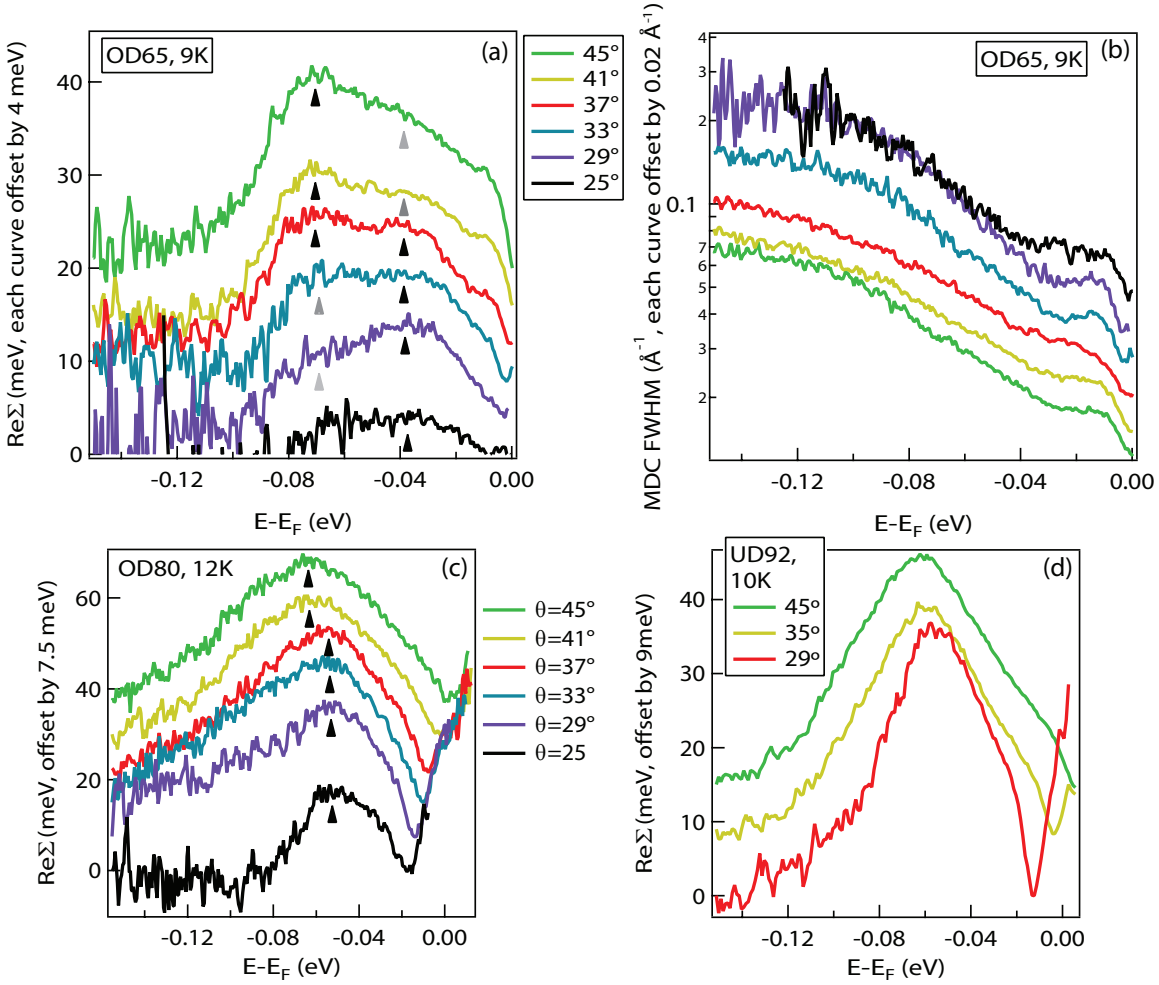

Figure B.3: (a) Momentum dependence of ReΣ for several cuts at specified FS angles, OD65. Arrows are guides to the eye for energies of kinks and subkinks. Samples are from newer batch. (b) MDC FWHM at the same cuts. (C) Momentum dependence of ReΣ for OD80. (d) momentum dependence of ReΣ for UD92.

B_{1g} phonon and the magnetic resonance mode. The B_{1g} phonon appears in Raman spectra at 38 meV in optimally-doped Bi-2212 [183]. The energy of the resonance mode (the one odd under exchange of CuO_2 planes) at $\mathbf{Q}_{||}=(\pi,\pi)$ ranges from 43 meV at optimal doping to 34 meV at p≈0.21 [184]. Following a comprehensive, high-resolution study of the spectral gap in the superconducting state [39], dispersion anomalies were analyzed in terms of gap shifting, and the results are shown in Fig.

B.5. This is similar to analysis done in [185], except with newer data (generally with higher statistics and resolution) and more dopings.

Two unanticipated results are seen. First, simple gap-shifting analysis implies a higher energy mode giving rise to the dip near the antinode as compared to the kink near the node. In Fig. B.5(b), the mode at the antinode has an average value of 36±3 meV and the mode at the node (E_{kink}-v_Δ) has an average value of 29±5 meV. The difference might be explained by considering the pseudogap at the antinode, as recent analysis has indicated that superconductivity, pseudogap (as modeled by a charge order with finite correlation length), and mode coupling are all required to reproduce the temperature dependence of spectral features and spectral weight [186]. Additionally, when considering coupling to the B_{1g} phonon, the dispersion of the phonon can produce a momentum-dependent kink energy, both with a Holstein coupling and with a momentum-dependent coupling[1]. The second surprising result in Fig. B.5 is that in order to imply a mode whose energy is independent of doping (i.e. the B_{1g} phonon), the near-nodal energy scale v_Δ must be used instead of the antinodal gap energy, Δ_{AN}. Thus, the kink energy does not reflect a gap shift by the full antinodal gap. This suggests that there is a strongly reduced density of states at the antinode in the doping regime where the low temperature gap deviates strongly from a simple *d*-wave form, such that the contributions of the antinode to the nodal kink are suppressed. Photoemission matrix elements make it difficult to quantitatively assess relative quasiparticle weight between different cuts, but it has been shown the the quasiparticle spectral weight at the antinode is suppressed with underdoping [67].

B.4 Temperature dependence of nodal spectrum across T*

This section explores the temperature dependence of the nodal kink above T* in UD92. There are a number of motivations for this project, particularly extending

[1] private communication with Steve Johnston

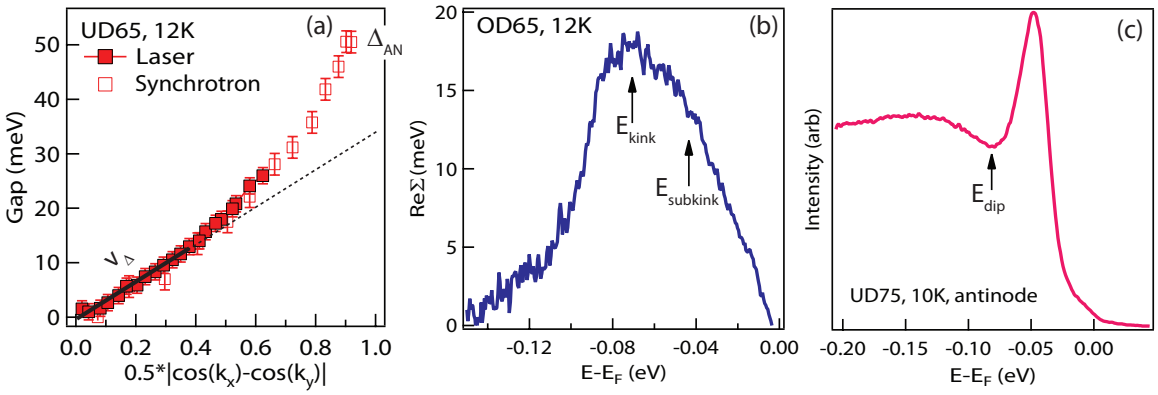

Figure B.4: (a) Δ_{AN} and v_Δ found from measuring gap at antinode and near-node, respectively. (b)E_{kink} is the peak energy of ReΣ and $E_{subkink}$ is a subkink energy defined by deviation from linearity at lower energy. (c) E_{dip} is defined from antinodal EDC.

the study to more dopings. First, if there is a boson mediating the pseudogap phase, there may be a signature in the kink across T*. Alternately, gap-shifting of the kink energy might be visible across T* as the pseudogap closes. Second, new pump-probe ARPES experiments have unprecedented access to nodal dynamics [187, 188], and it is important to have high-quality equilibrium data in order to distinguish interesting effects from trivial ones. Finally, though the temperature dependence of the nodal kink has been studied in the past, it is important to revisit it with new tools (high resolution laser ARPES) and new insights (pseudogap is distinct phase from T_c, competing phases manifest near node too).

Fig. B.6 shows the temperature dependence of ReΣ in UD92. The data are quantified by two metrics: the kink energy and the integrated area of ReΣ. The kink energy is found by smoothing ReΣ and taking the first derivative to find the peak. In the case that the peak energy depends on the number of smoothing iterations, the kink energy is measured as a function of the number of smoothing iterations, and extrapolated to zero. Fig. B.6(b) shows that the dominant kink energy in UD92 is unchanged across T_c, and weakly temperature dependent at higher temperatures, though always within error bars. The latter may be an artifact of thermal broadening which is more pronounced at low binding energy. The integrated area of ReΣ is one

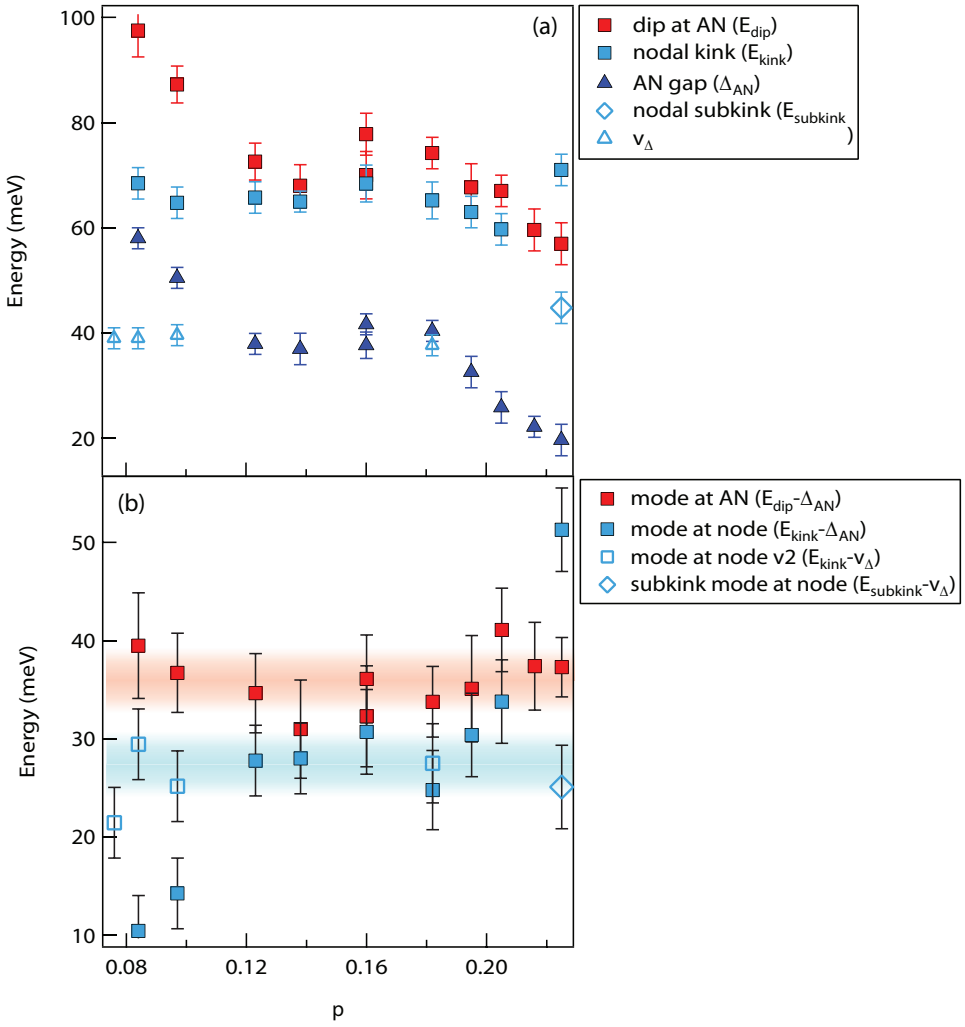

Figure B.5: (a) Energy scales from doping dependent data. Definitions in Fig. B.4. (b) Mode energies as defined in key. Horizontal bands are guides-to-the-eye for mode energy scales implied from nodal and antinodal energy scales.

way of quantifying the strength of the electron-boson coupling within a temperature-dependence study, though it must be stressed that the ReΣ plotted in the figure is only approximate, given our crude estimation for the bare band. The integrated ReΣ gets smaller across T_c, and continues to diminish with increasing temperature. The analysis suggests that it might level out at 200K, which is approximately T* for this doping, but further studies are needed to confirm this. Prior experiments indicated that mode coupling weakened across T_c [189, 190, 172]. However, the data shown

here extend to even higher temperature with more accuracy and suggest that the change at T_c might not be as singular as previously thought.

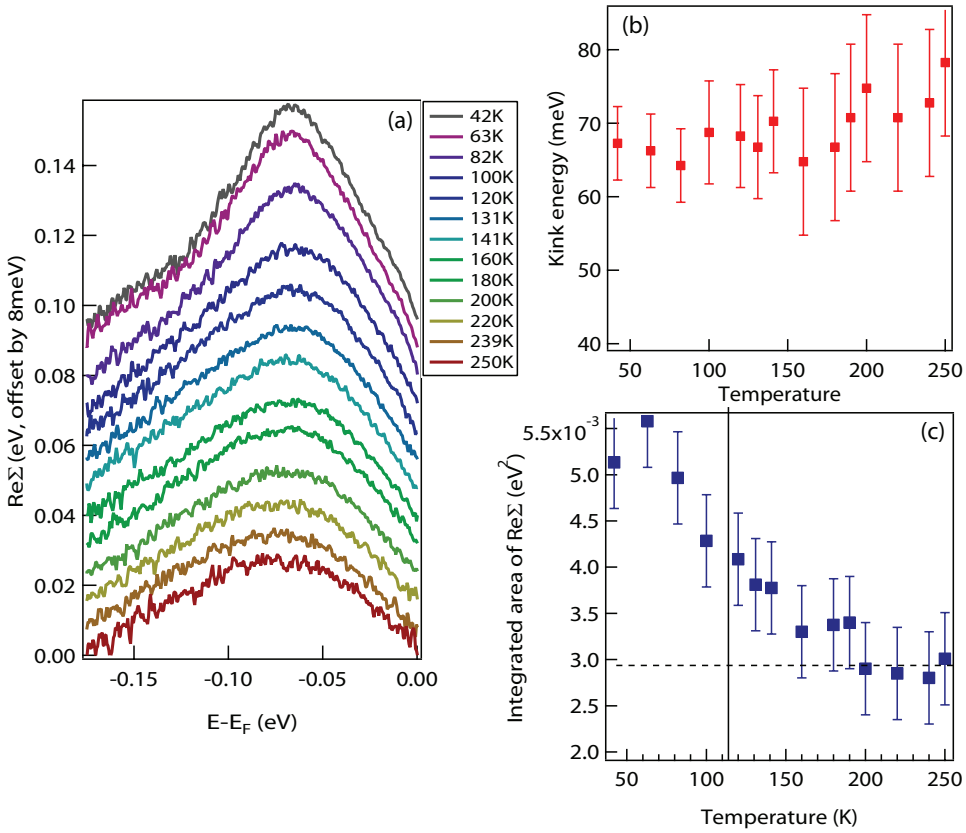

Figure B.6: (a) Temperature dependence of ReΣ. (b) Temperature dependence of energy position of peaks in (a). (c) Temperature dependence of integrated area of ReΣ curves in (a). Horizontal dotted line is a possibly obfuscating guide-to-the-eye.

Fig. B.7 studies the temperature dependence of MDCs at all energies and EDCs at k_F. Below T_c, the MDC width shows a pronounced anomaly at an energy close to the kink energy (Fig. B.7(a)). Above T_c, the MDC FWHM evolves smoothly with energy, even though the kink is still present in the dispersion. Note: data were not corrected for detector nonlinearity, so MDC widths above E_F are not to be taken seriously, especially at low temperature. The data in Fig. B.7(a) are shown in a different way in Fig. B.7(b), via the temperature evolution of the MDC FWHM at selected energies. At E_F, the MDC width is constant across T_c and increases linearly with temperature

above T_c. No anomaly is observed at T*. At higher binding energy, the sudden change at T_c is less pronounced, and the linear increase of the MDC width with temperature above T_c is less rapid. Fig. B.7(c) shows the temperature evolution of the EDC width at k_F. The EDC width is quantified by fitting symmetrized EDCs at k_F to the Norman model ($\Sigma(\mathbf{k}, \omega)$=-$i\Gamma_1$+ $\Delta^2/[(\omega+i0^+) + \epsilon(\mathbf{k})]$), with the gap fixed to zero [64]. Above T_c, the Norman model usually includes an additional scattering parameter Γ_0, but it is omitted in this fitting because the fitting is unstable and underconstrained for gapless spectra if both terms are used. It would be very interesting to repeat the analysis of Fig. B.7(b)-(c) with a deeply overdoped sample to assess if the temperature evolution of the MDC remains linear with temperature or becomes quadratic. Earlier experiments reported a T^2 dependence of the MDC width [191], but high resolution ARPES experiments often promote revisions of previous results.

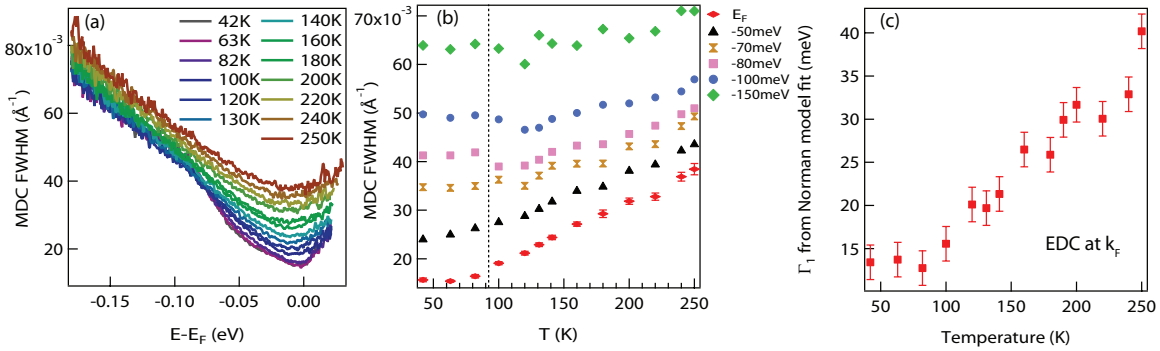

Figure B.7: (a) Energy and temperature dependence MDC FWHM for UD92 nodal cuts. (b) Temperature dependence of MDC FWHM at selected energies. (c) EDC width at k_F as fit by Norman model.

B.5 Conclusions

This appendix discussed a few experiments related to near-nodal mode coupling, with a focus on questions which can be addressed most readily with laser ARPES. Ascertaining which bosonic modes give rise to dispersion anomalies in the cuprates is a deep issue with implications for the mechanism of cuprate superconductivity. These excitations may be involved in Cooper pairing, or they may reflect elementary

excitations of the pseudogap. Even if these modes are found to be unrelated to superconductivity, it is highly non-trivial that superconductivity can exist amidst such strong, non-pairing electron boson coupling.

Appendix C

Appendix: $PdCoO_2$

C.1 Motivation

The first ARPES project I pursued was studying $PdCoO_2$, a triangular lattice oxide. Whereas the building blocks of cuprates are corner sharing CuO_6 octahedra, the building blocks of the cobaltates are CoO_6 edge-sharing octahedra. $PdCoO_2$ is well known for having an exceedingly high conductivity at low temperature [192].

The motivations for this were two-fold. First, it was pursued in the context of Na_xCoO_2 which has a similar crystal structure with identical building blocks of CoO_6 edge-sharing octahedra. Na_xCoO_2 becomes superconducting when intercalated with water [193], has large thermopower [194], and features antiferromagnetic exchange on a triangular lattice [195]. In that context, $PdCoO_2$ represents a clean, stoichiometric model system for Na_xCoO_2.

Second, understanding the conditions under which superb metallic conductivity–$\rho_{ab} = 0.03\mu\Omega cm$ at 1.6K in $PdCoO_2$–can develop in oxides is interesting from an applications standpoint. Many potentially technologically important materials are oxides with a perovskite crystal structure. This includeshigh temperature superconductors, giant magnetoresistant manganites, piezoelectrics, and solid oxide fuel cells are oxides[196]. Interfacing these materials with metallic components is easier if the latter have the same crystal structure.

C.2 Data and discussion

$PdCoO_2$ data were taken at SSRL. Figure C.1 shows photon energy dependence along a high symmetry cut (ΓM). Two features are observed, labeled A and B. It is now known that feature A is a bulk feature derived from Pd *s*-*d* hybridized states, while feature B is a surface feature consistent with Co *d* states [176]. The Fermi surface from feature B agrees with band structure calculations [197]. For the photon energies sampled in Fig. C.1, 19-22 eV yields the largest intensity near E_F for EDCs at both points A and B. We note that the hump observed near 0.3 eV at point A is likely from the surface state. In the MDCs, the highest intensity for both the bulk and surface bands is achieved at 22 eV.

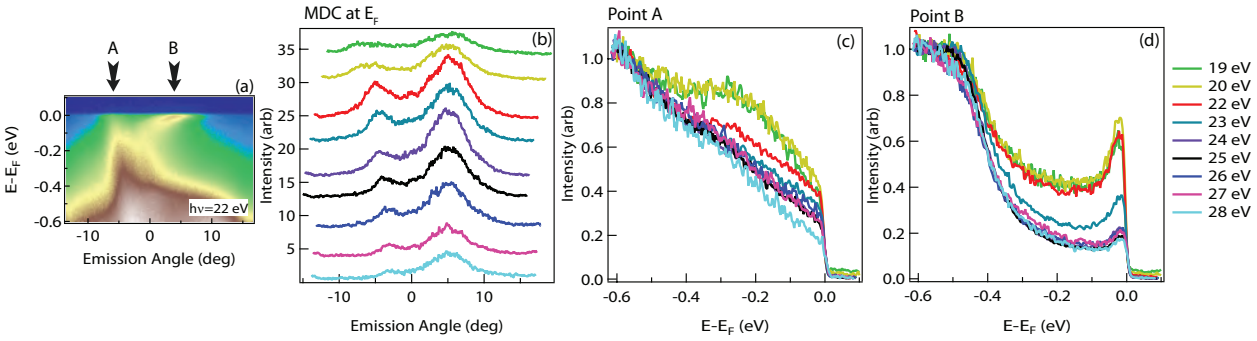

Figure C.1: Photon energy dependence, 10K. Conventions for labeling high symmetry points in Brilliouin zone given in Ref. [176]. (a) image plot taken with hν =22 eV, cut along ΓM. (b) MDCs at E_F for different photon energies, offset for clarity. MDCs are normalized at 12 degrees emission angle and offset horizontally such that feature B lines up for all photon energies. (c) EDCs at point A for different photon energies, normalized at 0.6 eV. (d) MDCs at point B for different photon energies, normalized at 0.6 eV.

Figure C.2 shows a high symmetry cut along M-Γ-M with 4 features visible, labeled A, B, C, D. Features C and D are also seen in Fig. C.1 and are robust at low temperature. The feature at the Γ point (A) is of unknown origin, and it fades away within 30 minutes at 10K. Feature B was not reported in Ref. [176], and it also has a finite lifetime, disappearing within 2 hours. Experiments on $PdCrO_2$ (Ref. [198]), reported a similar feature which was shown to be a surface reconstruction on a Pd-terminated surface. Thus, during cleaving, $PdCoO_2$ likely has mixed Pd and

O terminations, with the former aging more quickly. The Pd terminated portions give rise to surface feature B in Fig. C.2 and the O terminated portions give rise to surface feature C. The Fermi velocity of the bulk feature (D) is measured to be 5.15 eV$\mathring{A}$, which is consistent with the value reported in Ref. [176]. k_F was found to be 0.92 $\mathring{A}$, giving a cyclotron effective mass m*= $0.55m_e$.

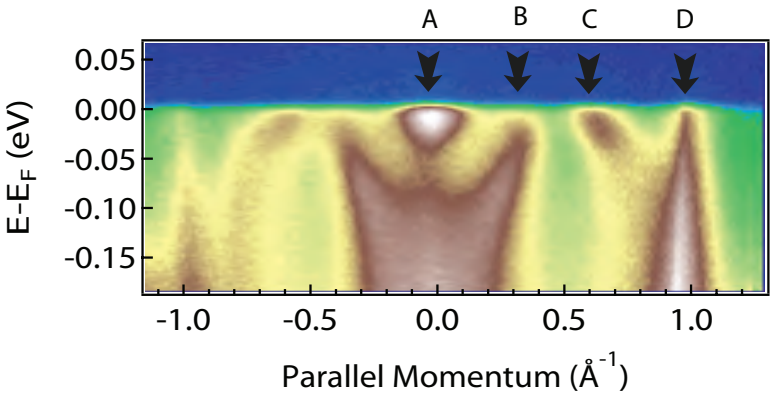

Figure C.2: Cut along M-Γ-M, taken with 21 eV photons at 10K.

Interestingly, ARPES data taken at 120 eV and 60 meV energy resolution were able to yield a resolution-limited bulk band and also observe two spin-orbit split bands constituting the surface band [176] while ARPES data at 21-22 eV and 10 meV energy resolution yielded much poorer bulk spectra. Though the 'universal curve' for the electron mean-free path does not suggest a tremendous enhancement of bulk sensitivity at 120 eV as compared to 21 eV [199], these results certainly suggests that this is the case for $PdCoO_2$ in particular. This lesson may be useful for studying other compounds which lack a neutral cleavage plane such as Hg-1201: sacrificing resolution at hν > 100eV may be worthwhile in terms of gaining cross section. Both $PdCoO_2$ and Hg-1201 were attempted with the 7eV laser, and both yielded no dispersions at all.

Appendix D

Appendix: 11eV laser

The 7eV laser has revolutionized ARPES experiments on Bi-2212, permitting faster data collection with better statistic, momentum resolution, and energy resolution. However, there are some key limitations, notably the difficulty in accessing the Brillouin zone boundary. Unfortunately, the mechanism of producing 7eV light–second harmonic generation in a KBBF crystal–is not applicable above ≈150nm (8.27 eV) because the phase matching angle approaches 90° and CaF_2 (used in the prism coupling) becomes opaque.

Recently, a laser system based on frequency up-conversion in a gas cell was demonstrated to produce 10.5 eV light with intensity, bandwidth, and repetition rate useable for equilibrium ARPES experiments [200].

We have purchased a 114nm (10.876 eV) laser (colloquially dubbed the '11eV laser') from Lumeras, and have worked with Lumeras to develop the optics system to interface with the ARPES chamber. In July 2013, we succeeded in taking the first spectra (Fig. D.1), and we are working to optimize the operation of this laser. The new lightsource has been demonstrated to work on other materials besides Bi-2212, and we are also continuing to explore which compounds show good cross section.

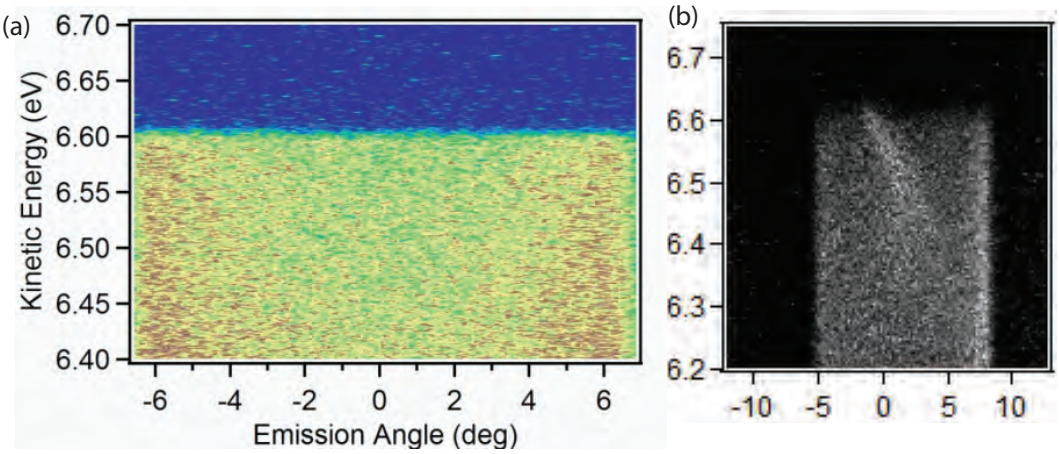

Figure D.1: (a) Au Fermi edge, taken at 6K, 5eV pass energy, and 0.3mm straight slit with SES2002 analyzer. Resolution was measured to be 8 meV. (b) Bi-2212, UD92, near node. Spectra taken before maximizing the 11eV intensity, hence the low photoemission counts.

Bibliography

[1] J. Bardeen, L. N. Cooper, and J. R. Schrieffer, "Theory of superconductivity," *Phys. Rev.*, vol. 108, pp. 1175–1204, Dec 1957.

[2] J. F. Annett, *Superconductivity Superfluids and Condensates*. Oxford University Press, 2004.

[3] M. R. Norman, "The challenge of unconventional superconductivity," *Science*, vol. 332, no. 6026, pp. 196–200, 2011.

[4] F. Steglich, J. Aarts, C. Bredl, W. Lieke, D. Meschede, W. Franz, and H. Schäfer, "Superconductivity in the presence of strong pauli paramagnetism: $CeCu_2Si_2$," *Physical Review Letters*, vol. 43, no. 25, p. 1892, 1979.

[5] F. Steglich, C. Bredl, W. Lieke, U. Rauchschwalbe, and G. Sparn, "Heavy fermion superconductivity," *Physica B+C*, vol. 126, no. 13, pp. 82 – 91, 1984.

[6] M. R. Norman, "Unconventional superconductivity," in *Novel Superfluids* (K. H. Bennemann and J. B. Ketterson, eds.), vol. 2, Oxford University Press, 2013.

[7] Y. Kamihara, H. Hiramatsu, M. Hirano, R. Kawamura, H. Yanagi, T. Kamiya, and H. Hosono, "Iron-based layered superconductor: LaOFeP," *Journal of the American Chemical Society*, vol. 128, no. 31, pp. 10012–10013, 2006.

[8] S. Nandi, M. G. Kim, A. Kreyssig, R. M. Fernandes, D. K. Pratt, A. Thaler, N. Ni, S. L. Bud'ko, P. C. Canfield, J. Schmalian, R. J. McQueeney, and A. I. Goldman, "Anomalous suppression of the orthorhombic lattice distortion in

superconducting $Ba(Fe_{1-x}Co_x)_2As_2$ single crystals," *Phys. Rev. Lett.*, vol. 104, p. 057006, Feb 2010.

[9] G. R. Stewart, "Superconductivity in iron compounds," *Rev. Mod. Phys.*, vol. 83, pp. 1589–1652, Dec 2011.

[10] J. G. Bednorz and K. A. Mller, "Possible high T_c superconductivity in the Ba-La-Cu-O system," *Zeitschrift fr Physik B Condensed Matter*, vol. 64, pp. 189–193, 1986.

[11] M. Monteverde, M. Nez-Regueiro, C. Acha, K. Lokshin, D. Pavlov, S. Putilin, and E. Antipov, "Fluorinated hg-1223 under pressure: the ultimate T_c of the cuprates?," *Physica C: Superconductivity*, vol. 408410, no. 0, pp. 23 – 24, 2004.

[12] H. Eisaki, N. Kaneko, D. L. Feng, A. Damascelli, P. K. Mang, K. M. Shen, Z.-X. Shen, and M. Greven, "Effect of chemical inhomogeneity in bismuth-based copper oxide superconductors," *Phys. Rev. B*, vol. 69, p. 064512, Feb 2004.

[13] S. Raghu, R. Thomale, and T. H. Geballe, "Optimal T_c of cuprates: The role of screening and reservoir layers," *Phys. Rev. B*, vol. 86, p. 094506, Sep 2012.

[14] P. Fulde, *Electron Correlations in molecules and solids*. Springer-V erlag Berlin Heidelberg GmbH, 1995.

[15] K. Tanaka, T. Yoshida, K. M. Shen, D. H. Lu, W. S. Lee, H. Yagi, A. Fujimori, Z.-X. Shen, Risdiana, T. Fujii, and I. Terasaki, "Evolution of electronic structure from insulator to superconductor in $Bi_2Sr_{2-x}La_x(Ca,Y)Cu_2O_{8+\delta}$," *Phys. Rev. B.*, vol. 81, p. 125115, 2010.

[16] M. Hashimoto, T. Yoshida, H. Yagi, M. Takizawa, A. Fujimori, M. Kubota, K. Ono, K. Tanaka, D. H. Lu, Z.-X. Shen, S. Ono, and Y. Ando, "Doping evolution of the electronic structure in the single-layer cuprate $Bi_2Sr_{2-x}La_xCuO_{6+\delta}$: Comparison with other single-layer cuprates," *Phys. Rev. B*, vol. 77, p. 094516, 2008.

[17] R. J. Birgeneau, C. Stock, J. M. Tranquada, and K. Yamada, "Magnetic neutron scattering in hole-doped cuprate superconductors," *J. Phys. Soc. Jpn.*, vol. 75, p. 111003, 2006.

[18] C. Niedermayer, C. Bernhard, T. Blasius, A. Golnik, A. Moodenbaugh, and J. I. Budnick, "Common phase diagram for antiferromagnetism in $La_{2-x}Sr_xCuO_4$ and $Y_{1-x}Ca_xBa_2Cu_3O_6$ as seen by muon spin rotation," *Phys. Rev. Lett.*, vol. 80, pp. 3843–3846, Apr 1998.

[19] D. Haug, V. Hinkov, Y. Sidis, P. Bourges, N. B. Christensen, A. Ivanov, T. Keller, C. T. Lin, and B. Keimer, "Neutron scattering study of the magnetic phase diagram of underdoped $YBa_2Cu_3O_{6+x}$," *New Journal of Physics*, vol. 12, no. 10, p. 105006, 2010.

[20] J. L. Tallon and J. W. Loram, "The doping dependence of t* what is the real high-T_c phase diagram?," *Physica C: Superconductivity*, vol. 349, pp. 53–68, Jan 2001.

[21] L. Taillefer, "Scattering and pairing in cuprate superconductors," *Annual Review of Condensed Matter Physics*, vol. 1, no. 1, pp. 51–70, 2010.

[22] S. Nakamae, K. Behnia, N. Mangkorntong, M. Nohara, H. Takagi, S. J. C. Yates, and N. E. Hussey, "Electronic ground state of heavily overdoped non-superconducting $la_{2-x}sr_xcuo_4$," *Phys. Rev. B*, vol. 68, p. 100502, Sep 2003.

[23] R. A. Cooper, Y. Wang, B. Vignolle, O. J. Lipscombe, S. M. Hayden, Y. Tanabe, T. Adachi, Y. Koike, M. Nohara, H. Takagi, C. Proust, and N. E. Hussey, "Anomalous criticality in the electrical resistivity of $La_{2x}Sr_xCuO_4$," *Science*, vol. 323, no. 5914, pp. 603–607, 2009.

[24] D. A. Wollman, D. J. Van Harlingen, W. C. Lee, D. M. Ginsberg, and A. J. Leggett, "Experimental determination of the superconducting pairing state in YBCO from the phase coherence of YBCO-Pb dc SQUIDs," *Phys. Rev. Lett.*, vol. 71, pp. 2134–2137, Sep 1993.

[25] Z.-X. Shen, D. S. Dessau, B. O. Wells, D. M. King, W. E. Spicer, A. J. Arko, D. Marshall, L. W. Lombardo, A. Kapitulnik, P. Dickinson, S. Doniach, J. DiCarlo, T. Loeser, and C. H. Park, "Anomalously large gap anisotropy in the a-b plane of $Bi_2Sr_2CaCu_2O_{8+\delta}$," *Phys. Rev. Lett.*, vol. 70, pp. 1553–1556, Mar 1993.

[26] J. W. Loram, K. A. Mirza, J. R. Cooper, and J. L. Tallon, "Specific heat evidence on the normal state pseudogap," *J. Phys. Chem. Solids*, vol. 59, p. 2091, 1998.

[27] A. G. Loeser, Z.-X. Shen, D. S. Dessau, D. S. Marshall, C. H. Park, P. Fournier, and A. Kapitulnik, "Excitation gap in the normal state of underdoped $Bi_2Sr_2CaCu_2O_{8+\delta}$," *Science*, vol. 273, pp. 325–329, 1996.

[28] V. Balédent, D. Haug, Y. Sidis, V. Hinkov, C. T. Lin, and P. Bourges, "Evidence for competing magnetic instabilities in underdoped $YBa_2Cu_3O_{6+x}$," *Phys. Rev. B*, vol. 83, p. 104504, Mar 2011.

[29] J. Xia, E. Schemm, G. Deutscher, S. A. Kivelson, D. A. Bonn, W. N. Hardy, R. Liang, W. Siemons, G. Koster, M. M. Fejer, and A. Kapitulnik, "Polar Kerr-effect measurements of the high-temperature $YBa_2Cu_3O_{6+x}$ superconductor: Evidence for broken symmetry near the pseudogap temperature," *Phys. Rev. Lett.*, vol. 100, p. 127002, Mar 2008.

[30] G. Coslovich, C. Giannetti, F. Cilento, S. D. Conte, T. Abebaw, D. Bossini, G. Ferrini, H. Eisaki, M. Greven, A. Damascelli, and F. Parmigiani, "Competition between the pseudogap and superconducting states of $Bi_2Sr_2Ca_{0.92}Y_{0.08}Cu_2O_{8+d}$ single crystals revealed by ultrafast broadband optical reflectivity," *arXiv:1302.0248 [cond-mat.str-el]*, 2013.

[31] R. Daou, J. Chang, D. LeBoeuf, O. Cyr-Choiniere, F. Laliberte, N. Doiron-Leyraud, B. J. Ramshaw, R. Liang, D. A. Bonn, W. N. Hardy, and L. Taillefer, "Broken rotational symmetry in the pseudogap phase of a high-tc superconductor," *Nature*, vol. 463, pp. 519– 522.

[32] W. S. Lee, I. M. Vishik, K. Tanaka, D. H. Lu, T. Sasagawa, N. Nagaosa, T. P. Devereaux, Z. Hussain, and Z.-X. Shen, "Abrupt onset of a second energy gap at the superconducting transition of underdoped Bi2212," *Nature*, vol. 450, pp. 81–84, Nov 2007.

[33] T. Kondo, R. Khasanov, T. Takeuchi, J. Schmalian, and A. Kaminski, "Competition between the pseudogap and superconductivity in the high-T_c copper oxides," *Nature*, vol. 457, p. 296, Jan 2009.

[34] M. Hashimoto, R.-H. He, K. Tanaka, J. P. Testaud, W. Meevasana, R. G. Moore, D. H. Lu, H. Yao, Y. Yoshida, H. Eisaki, T. P. Devereaux, Z. Hussain, and Z.-X. Shen, "Particlehole symmetry breaking in the pseudogap state of Bi2201," *Nat. Phys.*, vol. 6, p. 414, Apr 2010.

[35] K. Tanaka, W. S. Lee, D. H. Lu, A. Fujimori, T. Fujii, Risdiana, I. Terasaki, D. J. Scalapino, T. P. Devereaux, Z. Hussain, and Z.-X. Shen, "Distinct Fermi-Momentum-Dependent Energy Gaps in Deeply Underdoped Bi2212," *Science*, vol. 314, no. 5807, pp. 1910–1913, 2006.

[36] T. Yoshida, M. Hashimoto, S. Ideta, A. Fujimori, K. Tanaka, N. Mannella, Z. Hussain, Z.-X. Shen, M. Kubota, K. Ono, S. Komiya, Y. Ando, H. Eisaki, and S. Uchida, "Universal versus material-dependent two-gap behaviors of the high-T_c cuprate superconductors: Angle-resolved photoemission study of $La_{2-x}Sr_xCuO_4$," *Phys. Rev. Lett.*, vol. 103, p. 037004, July 2009.

[37] T. Kondo, T. Takeuchi, A. Kaminski, S. Tsuda, and S. Shin, "Evidence for two energy scales in the superconducting state of optimally doped $BiPb_2SrLa_2CuO_{6+\delta}$," *Phys. Rev. Lett.*, vol. 98, p. 267004, Jun 2007.

[38] M. Le Tacon, A. Sacuto, A. Georges, G. Kotliar, Y. Gallais, D. Colson, and A. Forget, "Two energy scales and two distinct quasiparticle dynamics in the superconducting state of underdoped cuprates," *Nat Phys*, vol. 2, pp. 537–543, 2006.

[39] I. M. Vishik, M. Hashimoto, R.-H. He, W.-S. Lee, F. Schmitt, D. Lu, R. G. Moore, C. Zhang, W. Meevasana, T. Sasagawa, S. Uchida, K. Fujita, S. Ishida, M. Ishikado, Y. Yoshida, H. Eisaki, Z. Hussain, T. P. Devereaux, and Z.-X. Shen, "Phase competition in trisected superconducting dome," *Proc. Natl. Acad. Sci.*, vol. 109, no. 45, pp. 18332–18337, 2012.

[40] G. Grissonnanche, O. Cyr-Choiniere, F. Laliberte, S. R. de Cotret, A. Juneau-Fecteau, S. Dufour-Beausejour, M.-E. Delage, D. LeBoeuf, J. Chang, B. Ramshaw, *et al.*, "Direct measurement of the upper critical field in a cuprate superconductor," *arXiv preprint arXiv:1303.3856*, 2013.

[41] S. Johnston, F. Vernay, and T. P. Devereaux, "Impact of an oxygen dopant in $Bi_2Sr_2CaCu_2O_{8+\delta}$," *EPL (Europhysics Letters)*, vol. 86, no. 3, p. 37007, 2009.

[42] W. L. McMillan and J. M. Rowell, "Lead phonon spectrum calculated from superconducting density of states," *Phys. Rev. Lett.*, vol. 14, pp. 108–112, Jan 1965.

[43] C. A. Reynolds, B. Serin, W. H. Wright, and L. B. Nesbitt, "Superconductivity of isotopes of mercury," *Phys. Rev.*, vol. 78, pp. 487–487, May 1950.

[44] A. Damascelli, Z. Hussain, and Z.-X. Shen, "Angle-resolved photoemission studies of the cuprate superconductors," *Rev. Mod. Phys.*, vol. 75, p. 473, April 2003.

[45] J. C. Campuzano, M. R. Norman, and M. Randeria, "Photoemission in the high T_c superconductors," in *Physics of Superconductors, Vol. II* (K. H. Bennemann and J. B. Ketterson, eds.), pp. 167–273, Springer-Verlag, 2004.

[46] T. Shimojima, K. Ishizaka, Y. Ishida, N. Katayama, K. Ohgushi, T. Kiss, M. Okawa, T. Togashi, X.-Y. Wang, C.-T. Chen, S. Watanabe, R. Kadota, T. Oguchi, A. Chainani, and S. Shin, "Orbital-dependent modifications of electronic structure across the magnetostructural transition in $BaFe_2As_2$," *Phys. Rev. Lett.*, vol. 104, p. 057002, Feb 2010.

[47] M. Yi, D. Lu, J.-H. Chu, J. G. Analytis, A. P. Sorini, A. F. Kemper, B. Moritz, S.-K. Mo, R. G. Moore, M. Hashimoto, W.-S. Lee, Z. Hussain, T. P. Devereaux, I. R. Fisher, and Z.-X. Shen, "Symmetry-breaking orbital anisotropy observed for detwinned $Ba(Fe_{1-x}Co_x)_2As_2$ above the spin density wave transition," *Proceedings of the National Academy of Sciences*, vol. 108, no. 17, pp. 6878–6883, 2011.

[48] H. Iwasawa, J. F. Douglas, K. Sato, T. Masui, Y. Yoshida, Z. Sun, H. Eisaki, H. Bando, A. Ino, M. Arita, K. Shimada, H. Namatame, M. Taniguchi, S. Tajima, S. Uchida, T. Saitoh, D. S. Dessau, and Y. Aiura, "Isotopic fingerprint of electron-phonon coupling in high-T_c cuprates," *Phys. Rev. Lett.*, vol. 101, p. 157005, Oct 2008.

[49] A. Kaminski and H. M. Fretwell, "On the extraction of the self-energy from angle-resolved photoemission spectroscopy," *New Journal of Physics*, vol. 7, no. 1, p. 98, 2005.

[50] C. Chen, Z. Xu, D. Deng, J. Zhang, G. Wong, B. Wu, N. Ye, and D. Tang, "The vacuum ultraviolet phase-matching characteristics of nonlinear optical $KBe_2Bo_3F_2$ crystal," *Applied Physics Letters*, p. 2930, 1995.

[51] C. Chen, G. Wang, X. Wang, and Z. Xu, "Deep-UV nonlinear optical crystal $KBe_2BO_3F_2$–discovery, growth, optical properties and applications," *Applied Physics B*, vol. 97, no. 1, pp. 9–25, 2009.

[52] T. Kiss, T. Shimojima, K. Ishizaka, A. Chainani, T. Togashi, T. Kanai, X.-Y. Wang, C.-T. Chen, S. Watanabe, and S. Shin, "A versatile system for ultrahigh resolution, low temperature, and polarization dependent laser-angle-resolved photoemission spectroscopy," *Review of Scientific Instruments*, vol. 79, no. 2, 2008.

[53] R. W. Boyd, *Nonlinear Optics, second edition.* Academic Press, 2003.

[54] G. R. Fowles, *Introduction to Modern Optics, second edition.* Dover publications inc., 1989.

[55] C. Chen, Z. Xu, D. Deng, J. Zhang, G. K. L. Wong, B. Wu, N. Ye, and D. Tang, "The vacuum ultraviolet phase-matching characteristics of nonlinear optical $KBe_2Bo_3F_2$ crystal," *Appl. Phys. Lett.*, vol. 68, p. 2930, 1996.

[56] T. Togashi, T. Kanai, T. Sekikawa, S. Watanabe, C. Chen, C. Zhang, Z. Xu, and J. Wang, "Generation of vacuum-ultraviolet light by an optically contacted, prism-coupled kbe2bo3f2 crystal," *Opt. Lett.*, vol. 28, pp. 254–256, Feb 2003.

[57] H. Ding, M. R. Norman, J. C. Campuzano, M. Randeria, A. F. Bellman, T. Yokoya, T. Takahashi, T. Mochiku, and K. Kadowaki, "Angle-resolved photoemission spectroscopy study of the superconducting gap anisotropy in $Bi_2Sr_2CaCu_2O_{8+x}$," *Phys. Rev. B*, vol. 54, pp. R9678–R9681, Oct 1996.

[58] H. Ding, T. Yokoya, J. C. Campuzano, T. Takahashi, M. Randeria, M. R. Norman, T. Mochiku, K. Kadowaki, and J. Giapintzakis, "Spectroscopic evidence for a pseudogap in the normal state of underdoped high-T_c superconductors," *Nature*, vol. 382, pp. 51–54, 1996.

[59] D. S. Marshall, D. S. Dessau, A. G. Loeser, C.-H. Park, A. Y. Matsuura, J. N. Eckstein, I. Bozovic, P. Fournier, A. Kapitulnik, W. E. Spicer, and Z.-X. Shen, "Unconventional electronic structure evolution with hole doping in $Bi_2Sr_2CaCu_2O_{8+\delta}$: Angle-resolved photoemission results," *Phys. Rev. Lett.*, vol. 76, pp. 4841–4844, Jun 1996.

[60] M. R. Norman, H. Ding, M. Randeria, J. C. Campuzano, T. Yokoya, T. Takeuchi, T. Takahashi, T. Mochiku, K. Kadowaki, P. Guptasarma, and D. G. Hinks, "Destruction of the fermi surface in underdoped high-T_c superconductors," *Nature*, vol. 392, pp. 157–160, Mar 1998.

[61] A. Kanigel, M. R. Norman, M. Randeria, U. Chatterjee, S. Souma, A. Kaminski, H. M. Fretwell, S. Rosenkranz, M. Shi, T. Sato, T. Takahashi, Z. Z. Li, H. Raffy, K. Kadowaki, D. Hinks, L. Ozyuzer, and J. C. Campuzano, "Evolution of the pseudogap from Fermi arcs to the nodal liquid," *Nat. Phys.*, vol. 2, pp. 447–451, 2006.

[62] R.-H. He, M. Hashimoto, H. Karapetyan, J. D. Koralek, J. P. Hinton, J. P. Testaud, V. Nathan, Y. Yoshida, H. Yao, K. Tanaka, W. Meevasana, R. G. Moore, D. H. Lu, S.-K. Mo, M. Ishikado, H. Eisaki, Z. Hussain, T. P. Devereaux, S. A. Kivelson, J. Orenstein, A. Kapitulnik, and Z.-X. Shen, "From a single-band metal to a high-temperature superconductor via two thermal phase transitions," *Science*, vol. 331, no. 6024, pp. 1579–1583, 2011.

[63] J. L. Tallon, C. Bernhard, H. Shaked, R. L. Hitterman, and J. D. Jorgensen, "Generic superconducting phase behavior in high-T_c cuprates: T_c variation with hole concentration in $YBa_2Cu_3O_{7-d}$," *Phys. Rev. B*, vol. 51, no. 18, pp. 12911–12914, 1995.

[64] M. R. Norman, M. Randeria, H. Ding, and J. C. Campuzano, "Phenomenology of the low-energy spectral function in high-T_c superconductors," *Phys. Rev. B*, vol. 57, p. R11093, May 1998.

[65] I. M. Vishik, E. A. Nowadnick, W. S. Lee, Z.-X. Shen, B. Moritz, T. P. Devereaux, K. Tanaka, T. Sasagawa, and T. Fujii, "A momentum-dependent perspective on quasiparticle interference in $Bi_2Sr_2CaCu_2O_{8+\delta}$," *Nature Physics*, vol. 5, pp. 718–721, Aug 2009.

[66] I. M. Vishik, W. S. Lee, R.-H. He, M. Hashimoto, Z. Hussain, T. P. Devereaux, and Z.-X. Shen, "ARPES studies of cuprate Fermiology: superconductivity, pseudogap and quasiparticle dynamics," *New Journal of Physics*, vol. 12, no. 10, p. 105008, 2010.

[67] D. L. Feng, D. H. Lu, K. M. Shen, C. Kim, H. Eisaki, A. Damascelli, R. Yoshizaki, J.-i. Shimoyama, K. Kishio, G. D. Gu, S. Oh, A. Andrus, J. O'Donnell, J. N. Eckstein, and Z.-X. Shen, "Signature of superfluid density in the single-particle excitation spectrum of $Bi_2Sr_2CaCu_2O_{8+\delta}$," *Science*, vol. 289, no. 5477, pp. 277–281, 2000.

[68] M. J. Lawler, K. Fujita, J. Lee, A. R. Schmidt, Y. Kohsaka, C. K. Kim, H. Eisaki, S. Uchida, J. C. Davis, J. P. Sethna, and E.-A. Kim, "Intra-unit-cell

electronic nematicity of the high-T_c copper-oxide pseudogap states," *Nature*, vol. 466, p. 347, Jul 2010.

[69] E. Razzoli, G. Drachuck, A. Keren, M. Radovic, N. C. Plumb, J. Chang, Y.-B. Huang, H. Ding, J. Mesot, and M. Shi, "Evolution from a nodeless gap to $d_{x^2-y^2}$-wave in underdoped $La_{2-x}Sr_xCuO_4$," *Phys. Rev. Lett.*, vol. 110, p. 047004, Jan 2013.

[70] U. Chatterjee, D. Ai, J. Zhao, S. Rosenkranz, A. Kaminski, H. Raffy, Z. Li, K. Kadowaki, M. Randeria, M. R. Norman, and J. C. Campuzano, "Electronic phase diagram of high-temperature copper oxide superconductors," *Proceedings of the National Academy of Sciences*, vol. 108, no. 23, pp. 9346–9349, 2011.

[71] U. Chatterjee, M. Shi, D. Ai, J. Zhao, A. Kanigel, S. Rosenkranz, H. Raffy, Z. Z. Li, K. Kadowaki, D. G. Hinks, Z. J. Xu, J. S. Wen, G. Gu, C. T. Lin, H. Claus, M. R. Norman, M. Randeria, and J. C. Campuzano, "Observation of a *d*-wave nodal liquid in highly underdoped $Bi_2Sr_2CaCu_2O_{8+\delta}$," *Nat. Phys.*, vol. 6, no. 2, pp. 99–103, 2010.

[72] H.-B. Yang, J. D. Rameau, Z.-H. Pan, G. D. Gu, P. D. Johnson, H. Claus, D. G. Hinks, and T. E. Kidd, "Reconstructed Fermi surface of underdoped $Bi_2Sr_2CaCu_2O_{8+\delta}$ cuprate superconductors," *Phys. Rev. Lett.*, vol. 107, p. 047003, Jul 2011.

[73] K. M. Shen, T. Yoshida, D. H. Lu, F. Ronning, N. P. Armitage, W. S. Lee, X. J. Zhou, A. Damascelli, D. L. Feng, N. J. C. Ingle, H. Eisaki, Y. Kohsaka, H. Takagi, T. Kakeshita, S. Uchida, P. K. Mang, M. Greven, Y. Onose, Y. Taguchi, Y. Tokura, S. Komiya, Y. Ando, M. Azuma, M. Takano, A. Fujimori, and Z.-X. Shen, "Fully gapped single-particle excitations in lightly doped cuprates," *Phys. Rev. B.*, vol. 69, p. 054503, 2004.

[74] Y. Peng, J. Meng, D. Mou, J. He, L. Zhao, Y. Wu, G. Liu, X. Dong, S. He, J. Zhang, X. Wang, Q. Peng, Z. Wang, S. Zhang, F. Yang, C. Chen, Z. Xu,

T. K. Lee, and X. J. Zhou, "Disappearance of nodal gap across the insulator-superconductor transition in a copper-oxide superconductor," *arXiv:1302.3017*, 2013.

[75] S. E. Sebastian, N. Harrison, M. M. Altarawnehb, C. H. Mielke, R. Liang, D. A. Bonn, W. N. Hardy, and G. G. Lonzarich, "Metal-insulator quantum critical point beneath the high T_c superconducting dome," *Proc. Nat. Acad. Sci.*, vol. 107, pp. 6175–6179, Mar 2010.

[76] D. LeBoeuf, N. Doiron-Leyraud, B. Vignolle, M. Sutherland, B. J. Ramshaw, J. Levallois, R. Daou, F. Laliberté, O. Cyr-Choinière, J. Chang, Y. J. Jo, L. Balicas, R. Liang, D. A. Bonn, W. N. Hardy, C. Proust, and L. Taillefer, "Lifshitz critical point in the cuprate superconductor $YBa_2Cu_3O_y$ from high-field hall effect measurements," *Phys. Rev. B*, vol. 83, p. 054506, Feb 2011.

[77] M. Sutherland, S. Y. Li, D. G. Hawthorn, R. W. Hill, F. Ronning, M. A. Tanatar, J. Paglione, H. Zhang, L. Taillefer, J. DeBenedictis, R. Liang, D. A. Bonn, and W. N. Hardy, "Delocalized Fermions in underdoped cuprate superconductors," *Phys. Rev. Lett.*, vol. 94, p. 147004, Apr 2005.

[78] V. Hinkov, D. Haug, B. Fauqu, P. Bourges, Y. Sidis, A. Ivanov, C. Bernhard, C. T. Lin, and B. Keimer, "Electronic liquid crystal state in the high-temperature superconductor $YBa_2Cu_3O_{6.45}$," *Science*, vol. 319, no. 5863, pp. 597–600, 2008.

[79] V. Emery and S. Kivelson, "Importance of phase fluctuations in superconductors with small superfluid density," *Nature*, vol. 374, no. 6521, pp. 434–437, 1995.

[80] J. L. Tallon, J. W. Loram, J. R. Cooper, C. Panagopoulos, and C. Bernhard, "Superfluid density in cuprate high-T_c superconductors: A new paradigm," *Phys. Rev. B*, vol. 68, p. 180501, Nov 2003.

[81] M. C. Boyer, W. D. Wise, K. Chatterjee, M. Yi, T. Kondo, T. Takeuchi, H. Ikuta, and E. W. Hudson, "Imaging the two gaps of the high-temperature superconductor $Bi_2Sr_2CuO_{6+x}$," *Nat. Phys.*, vol. 3, pp. 802–806, 2007.

[82] A. Pushp, C. V. Parker, A. N. Pasupathy, K. K. Gomes, S. Ono, J. Wen, Z. Xu, G. Gu, and A. Yazdani, "Extending universal nodal excitations optimizes superconductivity in $Bi_2Sr_2CaCu_2O_{8+\delta}$," *Science*, vol. 324, pp. 5935–5939, June 2009.

[83] H. Anzai, A. Ino, M. Arita, H. Namatame, M. Taniguchi, M. Ishikado, K. Fujita, S. Ishida, and S. Uchida, "Relation between the nodal and antinodal gap and critical temperature in superconducting bi2212," *Nature communications*, vol. 4, p. 1815, 2013.

[84] W. Anukool, S. Barakat, C. Panagopoulos, and J. R. Cooper, "Effect of hole doping on the London penetration depth in $Bi_{2.15}Sr_{1.85}CaCu_2O_{8+\delta}$ and $Bi_{2.1}Sr_{1.9}Ca_{0.85}Y_{0.15}Cu_2O_{8+\delta}$," *Phys. Rev. B*, vol. 80, p. 024516, Jul 2009.

[85] R.-H. He, K. Tanaka, S.-K. Mo, T. Sasagawa, M. Fujita, T. Adachi, N. Mannella, K. Yamada, Y. Koike, Z. Hussain, and Z.-X. Shen, "Energy gaps in the failed high-T_c superconductor $la_{1.875}ba_{0.125}cuo_4$," *Nat. Phys.*, vol. 5, pp. 119–123, 2009.

[86] J. C. Campuzano, H. Ding, M. R. Norman, H. M. Fretwell, M. Randeria, A. Kaminski, J. Mesot, T. Takeuchi, T. Sato, T. Yokoya, T. Takahashi, T. Mochiku, K. Kadowaki, P. Guptasarma, D. G. Hinks, Z. Konstantinovic, Z. Z. Li, and R. H., "Electronic spectra and their relation to the (π, π) collective mode in high-T_c superconductors," *Phys. Rev. Lett.*, vol. 83, no. 18, p. 3709, 1999.

[87] T. Kondo, Y. Hamaya, A. D. Palczewski, T. Takeuchi, J. S. Wen, Z. J. Xu, G. Gu, J. Schmalian, and A. Kaminski, "Disentangling Cooper-pair formation above the transition temperature from the pseudogap state in the cuprates," *Nat. Phys.*, vol. 7, pp. 21–25, 2011.

[88] S. Chakravarty, "Quantum oscillations and key theoretical issues in high temperature superconductors from the perspective of density waves," *Rep. on Prog. Phys.*, vol. 74, no. 2, p. 022501, 2011.

[89] J.-B. Wu, M.-X. Pei, and Q.-H. Wang, "Competing orders and interlayer tunneling in cuprate superconductors: A finite-temperature Landau theory," *Phys. Rev. B*, vol. 71, p. 172507, May 2005.

[90] A. M. Gabovich, A. I. Voitenko, T. Ekino, M. S. Li, H. Szymczak, and M. Pekala, "Competition of superconductivity and charge density waves in cuprates: Recent evidence and interpretation," *Adv. Cond. Mat. Phys.*, vol. 2010, p. 681070, 2010.

[91] T. Ekino, A. M. Gabovich, M. S. Li, M. Pkaa, H. Szymczak, and A. I. Voitenko, "The phase diagram for coexisting d-wave superconductivity and charge-density waves: cuprates and beyond," *J. of Phys.: Cond. Matt.*, vol. 23, no. 38, p. 385701, 2011.

[92] E. G. Moon and S. Sachdev, "Quantum critical point shifts under superconductivity: Pnictides and cuprates," *Phys. Rev. B*, vol. 82, p. 104516, Sep 2010.

[93] E. Wiesenmayer, H. Luetkens, G. Pascua, R. Khasanov, A. Amato, H. Potts, B. Banusch, H.-H. Klauss, and D. Johrendt, "Microscopic coexistence of superconductivity and magnetism in $Ba_{1-x}K_xFe_2As_2$," *Phys. Rev. Lett.*, vol. 107, p. 237001, Nov 2011.

[94] K. K. Gomes, A. N. Pasupathy, A. Pushp, S. Ono, Y. Ando, and A. Yazdani, "Visualizing pair formation on the atomic scale in the high-T_c superconductor $Bi_2Sr_2CaCu_2O_{8+\delta}$," *Nature*, vol. 447, pp. 569–572, 2007.

[95] R. M. Dipasupil, M. Oda, N. Momono, and M. Ido, "Energy gap evolution in the tunneling spectra of $Bi_2Sr_2CaCu_2O_{8+\delta}$," *J. Phys. Soc. Jpn.*, vol. 71, pp. 1535–1540, 2002.

[96] L. Ozyuzer, J. F. Zasadzinski, K. E. Gray, C. Kendziora, and N. Miyakawa, "Absence of pseudogap in heavily overdoped $Bi_2Sr_2CaCu_2O_{8+\delta}$ from tunneling spectroscopy ofbreak junctions," *Europhys. Lett.*, vol. 58, no. 4, pp. 589–595, 2002.

[97] M. Shi, J. Chang, S. Pailhés, M. R. Norman, J. C. Campuzano, M. Månsson, T. Claesson, O. Tjernberg, A. Bendounan, L. Patthey, N. Momono, M. Oda, M. Ido, C. Mudry, and J. Mesot, "Coherent d-wave superconducting gap in underdoped $La_{2-x}Sr_xCuO_4$ by angle-resolved photoemission spectroscopy," *Phys. Rev. Lett.*, vol. 101, p. 047002, Jul 2008.

[98] J. Wei, Y. Zhang, H. W. Ou, B. P. Xie, D. W. Shen, J. F. Zhao, L. X. Yang, M. Arita, K. Shimada, H. Namatame, M. Taniguchi, Y. Yoshida, H. Eisaki, and D. L. Feng, "Superconducting coherence peak in the electronic excitations of a single-layer $Bi_2Sr_{1.6}La_{0.4}CuO_{6+\delta}$ cuprate superconductor," *Phys. Rev. Lett.*, vol. 101, p. 097005, Aug 2008.

[99] C. Howald, H. Eisaki, N. Kaneko, M. Greven, and A. Kapitulnik, "Periodic density-of-states modulations in superconducting $Bi_2Sr_2CaCu_2O_{8+\delta}$," *Phys. Rev. B*, vol. 67, p. 014533, Jan 2003.

[100] Y. Kohsaka, C. Taylor, P. Wahl1, A. Schmidt, J. Lee, K. Fujita, J. W. Alldredge, K. McElroy, J. Lee, H. Eisaki, S. Uchida, D.-H. Lee, and J. C. Davis, "How Cooper pairs vanish approaching the Mott insulator in $Bi_2Sr_2CaCu_2O_{8+\delta}$," *Nature*, vol. 454, pp. 1072–1078, Aug 2008.

[101] K. McElroy, R. W. Simmonds, J. E. Hoffman, D.-H. Lee, J. Orenstein, H. Eisaki, S. Uchida, and J. C. Davis, "Relating atomic-scale electronic phenomena to wave-like quasiparticle states in superconducting $Bi_2Sr_2CaCu_2O_{8+\delta}$," *Nature*, vol. 422, pp. 592–596, April 2003.

[102] W. D. Wise, K. Chatterjee, M. C. Boyer, T. Kondo, T. Takeuchi, H. Ikuta, Z. Xu, W. Jinsheng, G. D. Gu, Y. Wang, and E. W. Hudson, "Imaging nanoscale

Fermi-surface variations in an inhomogeneous superconductor," *Nature Physics*, vol. 5, pp. 213–216, Jan 2009.

[103] M. Hashimoto, R.-H. He, J. P. Testaud, W. Meevasana, R. G. Moore, D. H. Lu, Y. Yoshida, H. Eisaki, T. P. Devereaux, Z. Hussain, and Z.-X. Shen, "Reaffirming the $d_{x^2-y^2}$ superconducting gap using the autocorrelation angle-resolved photoemission spectroscopy of $Bi_{1.5}Pb_{0.55}Sr_{1.6}La_{0.4}CuO_{6+\delta}$," *Phys. Rev. Lett.*, vol. 106, p. 167003, Apr 2011.

[104] C. V. Parker, P. Aynajian, E. H. da Silva Neto, A. Pushp, S. Ono, J. Wen, Z. Xu, G. Gu, and A. Yazdani, "Fluctuating stripes at the onset of the pseudogap in the high-T_c superconductor $Bi_2Sr_2CaCu_2O_{8+x}$," *Nature*, vol. 468, pp. 677–680, 2010.

[105] O. Fischer, M. Kugler, I. Maggio-Aprile, C. Berthod, and C. Renner, "Scanning tunneling spectroscopy of high-temperature superconductors," *Rev. Mod. Phys.*, vol. 79, pp. 353–419, Mar 2007.

[106] J. W. Alldredge, J. Lee, K. McElroy, M. Wang, K. Fujita, Y. Kohsaka, C. Taylor, H. Eisaki, S. Uchida, P. J. Hirschfeld, and J. C. Davis, "Evolution of the electronic excitation spectrum with strongly diminishing hole density in superconducting $Bi_2Sr_2CaCu_2O_{8+\delta}$," *Nat. Phys.*, vol. 4, pp. 319–326, 2008.

[107] H. Matsui, T. Sato, T. Takahashi, S.-C. Wang, H.-B. Yang, H. Ding, T. Fujii, T. Watanabe, and A. Matsuda, "Bcs-like bogoliubov quasiparticles in high-T_c superconductors observed by angle-resolved photoemission spectroscopy," *Phys. Rev. Lett.*, vol. 90, p. 217002, May 2003.

[108] S.-i. Ideta, T. Yoshida, A. Fujimori, H. Anzai, T. Fujita, A. Ino, M. Arita, H. Namatame, M. Taniguchi, Z.-X. Shen, K. Takashima, K. Kojima, and S.-i. Uchida, "Energy scale directly related to superconductivity in high-T_c cuprates: Universality from the temperature-dependent angle-resolved photoemission of $Bi_2Sr_2Ca_2Cu_3O_{10+\delta}$," *Phys. Rev. B*, vol. 85, p. 104515, Mar 2012.

[109] S. E. Sebastian, N. Harrison, and G. G. Lonzarich, "Towards resolution of the Fermi surface in underdoped high- T_c superconductors," *Reports on Progress in Physics*, vol. 75, no. 10, p. 102501, 2012.

[110] T. Kondo, A. Palczewski, Y. Hamaya, K. Ogawa, T. Takeuchi, J. S. Wen, G. Z. J. Xu, G. Gu, and A. Kaminski, "Collapse of the fermi surface and fingerprints of order in the pseudogap state of cuprate superconductors," *arXiv:1208.3448 [cond-mat.supr-con]*, 2013.

[111] G. Ghiringhelli, M. Le Tacon, M. Minola, S. Blanco-Canosa, C. Mazzoli, N. B. Brookes, G. M. De Luca, A. Frano, D. G. Hawthorn, F. He, T. Loew, M. M. Sala, D. C. Peets, M. Salluzzo, E. Schierle, R. Sutarto, G. A. Sawatzky, E. Weschke, B. Keimer, and L. Braicovich, "Long-range incommensurate charge fluctuations in (Y,Nd)$Ba_2Cu_3O_{6+x}$," *Science*, vol. 337, no. 6096, pp. 821–825, 2012.

[112] J. Chang, E. Blackburn, A. T. Holmes, N. B. Christensen, J. Larsen, J. Mesot, R. Liang, D. A. Bonn, W. N. Hardy, A. Watenphul, M. v. Zimmermann, E. M. Forgan, and S. M. Hayden, "Direct observation of competition between superconductivity and charge density wave order in $YBa_2Cu_3O_{6.67}$," *Nat Phys*, vol. 8, pp. 871–876, 2012.

[113] Y.-W. Zhong, T. Li, and Q. Han, "Monte carlo study of thermal fluctuations and fermi-arc formation in *d*-wave superconductors," *Phys. Rev. B*, vol. 84, p. 024522, Jul 2011.

[114] A. A. Kordyuk, S. V. Borisenko, M. Knupfer, and J. Fink, "Measuring the gap in angle-resolved photoemission experiments on cuprates," *Phys. Rev. B*, vol. 67, p. 064504, Feb 2003.

[115] T. J. Reber, N. C. Plumb, Z. Sun, Y. Cao, Q. Wang, K. McElroy, H. Iwasawa, M. Arita, J. S. Wen, Z. J. Xu, G. Gu, Y. Yoshida, H. Eisaki, Y. Aiura, and D. S. Dessau, "The origin and non-quasiparticle nature of Fermi arcs in $Bi_2Sr_2CaCu_2O_{8+\delta}$," *Nat Phys*, vol. 8, pp. 606–610.

[116] R. C. Dynes, V. Narayanamurti, and J. P. Garno, "Direct measurement of quasiparticle-lifetime broadening in a strong-coupled superconductor," *Phys. Rev. Lett.*, vol. 41, pp. 1509–1512, Nov 1978.

[117] S. Chakravarty, R. B. Laughlin, D. K. Morr, and C. Nayak, "Hidden order in the cuprates," *Phys. Rev. B*, vol. 63, p. 094503, Jan 2001.

[118] D. LeBoeuf, S. Krämer, W. Hardy, R. Liang, D. Bonn, and C. Proust, "Thermodynamic phase diagram of static charge order in underdoped $YBa_2Cu_3O_y$," *Nature Physics*, vol. 9, no. 2, pp. 79–83, 2012.

[119] N. Bariic, M. K. Chan, Y. Li, G. Yu, X. Zhao, M. Dressel, A. Smontara, and M. Greven, "Universal sheet resistance and revised phase diagram of the cuprate high-temperature superconductors," *Proceedings of the National Academy of Sciences*, 2013.

[120] A. Shekhter, B. Ramshaw, R. Liang, W. Hardy, D. Bonn, F. F. Balakirev, R. D. McDonald, J. B. Betts, S. C. Riggs, and A. Migliori, "Bounding the pseudogap with a line of phase transitions in $YBa_2Cu_3O_{6+\delta}$," *Nature*, vol. 498, no. 7452, pp. 75–77, 2013.

[121] E. Fradkin and S. A. Kivelson, "High-temperature superconductivity: Ineluctable complexity," *Nature Physics*, vol. 8, no. 12, pp. 864–866, 2012.

[122] S. V. Borisenko, A. A. Kordyuk, V. B. Zabolotnyy, D. S. Inosov, D. Evtushinsky, B. Büchner, A. N. Yaresko, A. Varykhalov, R. Follath, W. Eberhardt, L. Patthey, and H. Berger, "Two energy gaps and Fermi-surface "arcs" in $NbSe_2$," *Phys. Rev. Lett.*, vol. 102, p. 166402, Apr 2009.

[123] Y. He, Y. Yin, M. Zech, A. Soumyanarayanan, I. Zeljkovic, M. M. Yee, M. Boyer, K. Chatterjee, W. Wise, T. Kondo, *et al.*, "Fermi surface pairing & coherence in a high T_c superconductor," *arXiv preprint arXiv:1305.2778*, 2013.

[124] S. Sachdev and R. La Placa, "Bond order in two-dimensional metals with antiferromagnetic exchange interactions," *Phys. Rev. Lett.*, vol. 111, p. 027202, Jul 2013.

[125] J. D. Rameau, H.-B. Yang, G. D. Gu, and P. D. Johnson, "Coupling of low-energy electrons in the optimally doped $Bi_2Sr_2CaCu_2O_8$ superconductor to an optical phonon mode," *Phys. Rev. B*, vol. 80, p. 184513, Nov 2009.

[126] I. M. Vishik, W. S. Lee, F. Schmitt, B. Moritz, T. Sasagawa, S. Uchida, K. Fujita, S. Ishida, C. Zhang, T. P. Devereaux, and Z.-X. Shen, "Doping-dependent nodal Fermi velocity of the high-temperature superconductor $Bi_2Sr_2CaCu_2O_{8+\delta}$ revealed using high-resolution angle-resolved photoemission spectroscopy," *Phys. Rev. Lett.*, vol. 104, p. 207002, 2010.

[127] H. Anzai, A. Ino, T. Kamo, T. Fujita, M. Arita, H. Namatame, M. Taniguchi, A. Fujimori, Z.-X. Shen, M. Ishikado, and S. Uchida, "Energy-dependent enhancement of the electron-coupling spectrum of the underdoped $Bi_2Sr_2CaCu_2O_8$ superconductor," *Phys. Rev. Lett.*, vol. 105, p. 227002, Nov 2010.

[128] N. C. Plumb, T. J. Reber, J. D. Koralek, Z. Sun, J. F. Douglas, Y. Aiura, K. Oka, H. Eisaki, and D. S. Dessau, "Low-energy ($\approx$10 meV) feature in the nodal electron self-energy and strong temperature dependence of the Fermi velocity in $Bi_2Sr_2CaCu_2O_8$," *Phys. Rev. Lett.*, vol. 105, p. 046402, Jul 2010.

[129] T. Kondo, Y. Nakashima, W. Malaeb, Y. Ishida, Y. Hamaya, T. Takeuchi, and S. Shin, "Doping-dependent energy scale of the low-energy band renormalization in $(Bi,Pb)_2(Sr,La)_2CuO_{6+\delta}$," *arXiv:1212.0335 [cond-mat.supr-con]*, 2013.

[130] S. Johnston, I. M. Vishik, W. S. Lee, F. Schmitt, S. Uchida, K. Fujita, S. Ishida, N. Nagaosa, Z. X. Shen, and T. P. Devereaux, "Evidence for the importance of extended coulomb interactions and forward scattering in cuprate superconductors," *Phys. Rev. Lett.*, vol. 108, p. 166404, Apr 2012.

[131] X. J. Zhou, T. Yoshida, A. Lanzara, P. V. Bogdanov, S. A. Kellar, K. M. Shen, W. L. Yang, F. Ronning, T. Sasagawa, T. Kakeshita, T. Noda, H. Eisaki,

S. Uchida, C. T. Lin, F. Zhou, J. W. Xiong, W. X. Ti, Z. X. Zhao, A. Fujimori, Z. Hussain, and Z.-X. Shen, "High temperature superconductors: Universal nodal Fermi velocity," *Nature*, vol. 423, p. 398, May 2003.

[132] Y. Ando, S. Komiya, K. Segawa, S. Ono, and Y. Kurita, "Electronic phase diagram of high-T_c cuprate superconductors from a mapping of the in-plane resistivity curvature," *Phys. Rev. Lett.*, vol. 93, p. 267001, Dec 2004.

[133] T. Yoshida, X. J. Zhou, D. H. Lu, S. Komiya, Y. Ando, H. Eisaki, T. Kakeshita, S. Uchida, Z. Hussain, Z.-X. Shen, and A. A Fujimori, "Low-energy electronic structure of the high-T_c cuprates $La_{2-x}Sr_xCuO_4$ studied by angle-resolved photoemission spectroscopy," *J. Phys.: Condens. Matter*, vol. 19, p. 125209, Mar 2007.

[134] X. F. Sun, S. Ono, Y. Abe, S. Komiya, K. Segawa, and Y. Ando, "Electronic inhomogeneity and breakdown of the universal thermal conductivity of cuprate superconductors," *Phys. Rev. Lett.*, vol. 96, p. 017008, Jan 2006.

[135] B. M. Andersen and P. Hirschfeld, "Breakdown of universal transport in correlated *d*-wave superconductors," *Phys. Rev. Lett.*, vol. 100, p. 257003, Jun 2008.

[136] P. D. Johnson, A. V. Fedorov, and T. Valla, "Photoemission studies of self-energy effects in cuprate superconductors," *J. Electron Spectrosc. Relat. Phenom.*, vol. 117-118, p. 153, Jun 2001.

[137] W. S. Lee, W. Meevasana, S. Johnston, D. H. Lu, I. M. Vishik, R. G. Moore, H. Eisaki, N. Kaneko, T. P. Devereaux, and Z.-X. Shen, "Superconductivity-induced self-energy evolution of the nodal electron of optimally doped $Bi_2Sr_2Ca_{0.92}Y_{0.08}Cu_2O_{8+\delta}$," *Phys. Rev. B*, vol. 77, p. 140504(R), Apr 2008.

[138] W. S. Lee, S. Johnston, T. P. Devereaux, and Z.-X. Shen, "Aspects of electron-phonon self-energy revealed from angle-resolved photoemission spectroscopy," *Phys. Rev. B*, vol. 75, p. 195116, May 2007.

[139] X. J. Zhou, J. Shi, T. Yoshida, T. Cuk, W. L. Yang, V. Brouet, J. Nakamura, N. Mannella, S. Komiya, Y. Ando, F. Zhou, W. X. Ti, J. Xiong, Z. X. Zhao, T. Sasagawa, T. Kakeshita, H. Eisaki, S. Uchida, A. Fujimori, Z. Zhang, E. W. Plummer, R. B. Laughlin, Z. Hussain, and Z.-X. Shen, "Multiple bosonic mode coupling in the electron self-energy of $La_{2-x}Sr_xCuO_4$," *Phys. Rev. Lett.*, vol. 95, p. 117001, Sep 2005.

[140] W. Meevasana, X. J. Zhou, S. Sahrakorpi, W. S. Lee, W. L. Yang, K. Tanaka, N. Mannella, T. Yoshida, D. H. Lu, Y. L. Chen, R. H. He, H. Lin, S. Komiya, Y. Ando, F. Zhou, W. X. Ti, J. W. Xiong, Z. X. Zhao, T. Sasagawa, T. Kakeshita, K. Fujita, S. Uchida, H. Eisaki, A. Fujimori, Z. Hussain, R. S. Markiewicz, A. Bansil, N. Nagaosa, J. Zaanen, T. P. Devereaux, and Z.-X. Shen, "Hierarchy of multiple many-body interaction scales in high-temperature superconductors," *Phys. Rev. B*, vol. 75, no. 17, p. 174506, 2007.

[141] M. Chiao, R. W. Hill, C. Lupien, L. Taillefer, P. Lambert, R. Gagnon, and P. Fournier, "Low-energy quasiparticles in cuprate superconductors: A quantitative analysis," *Phys. Rev. B*, vol. 62, pp. 3554–3558, Apr 2000.

[142] N. E. Hussey, "Low-energy quasiparticles in high-T_c cuprates," *Adv. Phys*, vol. 51, pp. 1685–1771, Dec 2002.

[143] H. Shakeripour, C. Petrovic, and L. Taillefer, "Heat transport as a probe of superconducting gap structure," *New Journal of Physics*, vol. 11, p. 055065, 2009.

[144] A. C. Durst and P. A. Lee, "Impurity-induced quasiparticle transport and universal-limit wiedemann-franz violation in d-wave superconductors," *Phys. Rev. B*, vol. 62, p. 1270, Jan 2000.

[145] J. Takeya, Y. Ando, S. Komiya, and X. F. Sun, "Low-temperature electronic heat transport in $La_{2-x}Sr_xCuO_4$ single crystals: Unusual low-energy physics in the normal and superconducting states," *Phys. Rev. Lett.*, vol. 88, p. 077001, Feb 2002.

[146] M. Sutherland, D. G. Hawthorn, R. W. Hill, F. Ronning, S. Wakimoto, H. Zhang, C. Proust, E. Boaknin, C. Lupien, L. Taillefer, R. Liang, D. A. Bonn, W. N. Hardy, R. Gagnon, N. E. Hussey, T. Kimura, M. Nohara, and H. Takagi, "Thermal conductivity across the phase diagram of cuprates: Low-energy quasiparticles and doping dependence of the superconducting gap," *Phys. Rev. B*, vol. 67, p. 174520, May 2003.

[147] Y. Ando, S. Ono, X. F. Sun, J. Takeya, F. F. Balakirev, J. B. Betts, and G. S. Boebinger, "Quantum phase transitions in the cuprate superconductor $Bi_2Sr_{2-x}La_xCuO_{6-\delta}$," *Phys. Rev. Lett.*, vol. 92, p. 247004, Jun 2004.

[148] J. Mesot, M. R. Norman, H. Ding, M. Randeria, J. C. Campuzano, A. Paramekanti, H. M. Fretwell, A. Kaminski, T. Takeuchi, T. Yokoya, T. Sato, T. Takahashi, T. Mochiku, and K. Kadowaki, "Superconducting gap anisotropy and quasiparticle interactions: A doping dependent photoemission study," *Phys. Rev. Lett.*, vol. 83, pp. 840–843, Jul 1999.

[149] Y. Ando, J. Takeya, Y. Abe, X. F. Sun, and A. N. Lavrov, "Novel anisotropy in the superconducting gap structure of $Bi_2Sr_2CaCu_2O_{8+\delta}$ probed by quasiparticle heat transport," *Phys. Rev. Lett.*, vol. 88, p. 147004, Apr 2002.

[150] P. R. Schiff and A. C. Durst, "Effect of coexisting order of various form and wave vector on low-temperature thermal conductivity in d-wave superconductors," *Phys. Rev. B*, vol. 81, p. 054504, Feb 2010.

[151] J. Wei, Y. Zhang, H. W. Ou, B. P. Xie, D. W. Shen, J. F. Zhao, L. X. Yang, M. Arita, K. Shimada, H. Namatame, M. Taniguchi, Y. Yoshida, H. Eisaki, and D. L. Feng, "Superconducting coherence peak in the electronic excitations of a single-layer $Bi_2Sr_{1.6}La_{0.4}CuO_{6+\delta}$ cuprate superconductor," *Phys. Rev. Lett.*, vol. 101, p. 097005, Aug 2008.

[152] T. Yoshida, M. Hashimoto, S. Ideta, A. Fujimori, K. Tanaka, N. Mannella, Z. Hussain, Z.-X. Shen, M. Kubota, K. Ono, S. Komiya, Y. Ando, H. Eisaki, and S. Uchida, "Universal versus material-dependent two-gap behaviors of

the high-T_c cuprate superconductors: Angle-resolved photoemission study of $La_{2-x}Sr_xCuO_4$," *Phys. Rev. Lett.*, vol. 103, p. 037004, Jul 2009.

[153] K. Nakayama, T. Sato, T. Takahashi, T. Nishizaki, Y. Takahashi, and N. Kobayashi, "High-resolution angle-resolved photoemission study of bulk electronic states in $YBa_2Cu_3O_{7-\delta}$," *J. Phys. Chem. Solids*, vol. 69, pp. 2967–2970, Dec 2008.

[154] S. Johnston, F. Vernay, B. Moritz, Z.-X. Shen, N. Nagaosa, J. Zaanen, and T. P. Devereaux, "Systematic study of electron-phonon coupling to oxygen modes across the cuprates," *Phys. Rev. B*, vol. 82, p. 064513, Aug 2010.

[155] N. Bulut and D. J. Scalapino, "$d_{x^2-y^2}$ symmetry and the pairing mechanism," *Phys. Rev. B*, vol. 54, pp. 14971–14973, Dec 1996.

[156] N. Baric, Y. Li, X. Zhao, Y.-C. Cho, G. Chabot-Couture, G. Yu, and M. Greven, "Demonstrating the model nature of the high-temperature superconductor $HgBa_2CuO_{4+\delta}$," *Phys. Rev. B*, vol. 78, p. 054518, Aug 2008.

[157] M. Hashimoto, R.-H. He, I. M. Vishik, F. Schmitt, R. G. Moore, D. H. Lu, Y. Yoshida, H. Eisaki, Z. Hussain, T. P. Devereaux, and Z.-X. Shen, "Superconductivity distorted by the coexisting pseudogap in the antinodal region of $Bi_{1.5}Pb_{0.55}Sr_{1.6}LaCuO_{6+\delta}$: A photon-energy-dependent angle-resolved photoemission study," *Phys. Rev. B*, vol. 86, p. 094504, Sep 2012.

[158] T. Das, "Q=0 collective modes originating from the low-lying Hg-O band in superconducting $HgBa_2CuO_{4+d}$," *Phys. Rev. B*, vol. 86, p. 054518, Aug 2012.

[159] W. Meevasana, *Electronic structure and collective mode coupling in single-layer high-T_c superconductor, $Bi_2Sr_2CuO_6$*. PhD thesis, Stanford University, 2009.

[160] T. Yoshida, X. J. Zhou, K. Tanaka, W. L. Yang, Z. Hussain, Z.-X. Shen, A. Fujimori, S. Sahrakorpi, M. Lindroos, R. S. Markiewicz, A. Bansil, S. Komiya, Y. Ando, H. Eisaki, T. Kakeshita, and S. Uchida, "Systematic doping evolution of the underlying Fermi surface of $La_{2-x}Sr_xCuO_4$," *Phys. Rev. B*, vol. 74, p. 224510, Dec 2006.

[161] D. C. Peets, D. G. Hawthorn, K. M. Shen, Y.-J. Kim, D. S. Ellis, H. Zhang, S. Komiya, Y. Ando, G. A. Sawatzky, R. Liang, D. A. Bonn, and W. N. Hardy, "X-ray absorption spectra reveal the inapplicability of the single-band Hubbard model to overdoped cuprate superconductors," *Phys. Rev. Lett.*, vol. 103, p. 087402, Aug 2009.

[162] Y. Sakurai, M. Itou, B. Barbiellini, P. E. Mijnarends, R. S. Markiewicz, S. Kaprzyk, J.-M. Gillet, S. Wakimoto, M. Fujita, S. Basak, Y. J. Wang, W. Al-Sawai, H. Lin, A. Bansil, and K. Yamada, "Imaging doped holes in a cuprate superconductor with high-resolution Compton scattering," *Science*, vol. 332, no. 6030, pp. 698–702, 2011.

[163] J. Y. T. Wei, C. C. Tsuei, P. J. M. van Bentum, Q. Xiong, C. W. Chu, and M. K. Wu, "Quasiparticle tunneling spectra of the high-T_c mercury cuprates: Implications of the d-wave two-dimensional van hove scenario," *Phys. Rev. B*, vol. 57, pp. 3650–3662, Feb 1998.

[164] V. Brouet, A. Nicolaou, M. Zacchigna, A. Taleb-Ibrahimi, P. L. Fvre, and F. Bertran, "Measuring fermi velocities with arpes in narrow band systems: The case of layered cobaltates," *Journal of Electron Spectroscopy and Related Phenomena*, vol. 185, no. 5-7, pp. 146 – 151, 2012.

[165] E. D. Hansen, T. Miller, and T.-C. Chiang, "Surface photoemission in ag(100)," *Phys. Rev. B*, vol. 55, pp. 1871–1875, Jan 1997.

[166] T. Devereaux, T. Cuk, Z.-X. Shen, and N. Nagaosa, "Anisotropic electron-phonon interaction in the cuprates," *Phys. Rev. Lett.*, vol. 93, p. 117004, sept 2004.

[167] A. Kaminski, M. Randeria, J. C. Campuzano, M. R. Norman, H. Fretwell, J. Mesot, T. Sato, T. Takahashi, and K. Kadowaki, "Renormalization of spectral line shape and dispersion below T_c in $Bi_2Sr_2CaCu_2O_{8+\delta}$," *Phys. Rev. Lett.*, vol. 86, p. 1070, Feb 2001.

[168] S. V. Borisenko, A. A. Kordyuk, T. K. Kim, A. Koitzsch, M. Knupfer, J. Fink, M. S. Golden, M. Eschrig, H. Berger, and R. Follath, "Anomalous enhancement of the coupling to the magnetic resonance mode in underdoped Pb-Bi2212," *Phys. Rev. Lett.*, vol. 90, p. 207001, May 2003.

[169] A. W. Sandvik, D. J. Scalapino, and N. E. Bickers, "Effect of an electron-phonon interaction on the one-electron spectral weight of a d-wave superconductor," *Phys. Rev. B*, vol. 69, p. 094523, Mar 2004.

[170] M. d'Astuto, A. Mirone, P. Giura, D. Colson, A. Forget, and M. Krisch, "Phonon dispersion in the one-layer cuprate $HgBa_2CuO_4$," *Journal of Physics: Condensed Matter*, vol. 15, no. 50, p. 8827, 2003.

[171] Y. Li, V. Baledent, G. Yu, N. Barisic, K. Hradil, R. A. Mole, Y. Sidis, P. Steffens, X. Zhao, and M. Bourges, P. andGreven, "Hidden magnetic excitation in the pseudogap phase of a high-T_c superconductor," *Nature*, vol. 468, pp. 283–285.

[172] A. Lanzara, P. V. Bogdanov, X. J. Zhou, S. A. Kellar, D. L. Feng, E. D. Lu, T. Yoshida, H. Eisaki, A. Fujimori, K. Kishio, J.-I. Shimoyama, T. Noda, S. Uchida, Z. Hussain, and Z.-X. Shen, "Evidence for ubiquitous strong electronphonon coupling in high-temperature superconductors," *Nature*, vol. 412, pp. 510–514, Aug 2001.

[173] E. van Heumen, E. Muhlethaler, A. B. Kuzmenko, H. Eisaki, W. Meevasana, M. Greven, and D. van der Marel, "Optical determination of the relation between the electron-boson coupling function and the critical temperature in high-T_c cuprates," *Phys. Rev. B*, vol. 79, p. 184512, May 2009.

[174] T. Muro, Y. Kato, T. Kinoshita, and Y. Watanabe, "Ultrahigh-vacuum cleaving system for sub-100-μm crystals," *Review of Scientific Instruments*, vol. 81, no. 4, p. 043901, 2010.

[175] M. Mansson, T. Claesson, U. O. Karlsson, O. Tjernberg, S. Pailhes, J. Chang, J. Mesot, M. Shi, L. Patthey, N. Momono, M. Oda, and M. Ido, "On-board

sample cleaver," *Review of Scientific Instruments*, vol. 78, no. 7, p. 076103, 2007.

[176] H.-J. Noh, J. Jeong, J. Jeong, E.-J. Cho, S. B. Kim, K. Kim, B. I. Min, and H.-D. Kim, "Anisotropic electric conductivity of delafossite $PdCoO_2$ studied by angle-resolved photoemission spectroscopy," *Phys. Rev. Lett.*, vol. 102, p. 256404, Jun 2009.

[177] T. J. Reber, N. C. Plumb, Y. Cao, Z. Sun, Q. Wang, K. McElroy, H. Iwasawa, M. Arita, J. S. Wen, Z. J. Xu, G. Gu, Y. Yoshida, H. Eisaki, Y. Aiura, and D. S. Dessau, "Prepairing and the "filling" gap in the cuprates from the tomographic density of states," *Phys. Rev. B*, vol. 87, p. 060506, Feb 2013.

[178] H.-B. Yang, J. Rameau, P. Johnson, T. Valla, A. Tsvelik, and G. Gu, "Emergence of preformed Cooper pairs from the doped Mott insulating state in $Bi_2Sr_2CaCu_2O_{8+\delta}$," *Nature*, vol. 456, no. 7218, pp. 77–80, 2008.

[179] N. Mannella, S. Marchesini, A. Kay, A. Nambu, T. Gresch, S.-H. Yang, B. Mun, J. Bussat, A. Rosenhahn, and C. Fadley, "Correction of non-linearity effects in detectors for electron spectroscopy," *Journal of electron spectroscopy and related phenomena*, vol. 141, no. 1, pp. 45–59, 2004.

[180] J. He, W. Zhang, J. M. Bok, D. Mou, L. Zhao, Y. Peng, S. He, G. Liu, X. Dong, J. Zhang, J. S. Wen, Z. J. Xu, G. D. Gu, X. Wang, Q. Peng, Z. Wang, S. Zhang, F. Yang, C. Chen, Z. Xu, H.-Y. Choi, C. M. Varma, and X. J. Zhou, "Coexistence of two sharp-mode couplings and their unusual momentum dependence in the superconducting state of $Bi_2Sr_2CaCu_2O_{8+\delta}$ superconductor revealed by laser-based angle-resolved photoemission," *arXiv:1210.0710 [cond-mat.supr-con]*, 2012.

[181] S. R. Park, Y. Cao, Q. Wang, M. Fujita, K. Yamada, S.-K. Mo, D. S. Dessau, and D. Reznik, "Broken relationship between superconducting pairing interaction and electronic dispersion kinks in LSCO," *arXiv:1304.0505 [cond-mat.supr-con]*, 2013.

[182] T. Cuk, F. Baumberger, D. H. Lu, N. Ingle, X. J. Zhou, H. Eisaki, N. Kaneko, Z. Hussain, T. P. Devereaux, N. Nagaosa, and Z.-X. Shen, "Coupling of the B_{1g} phonon to the antinodal electronic states of $Bi_2Sr_2CaCu_2O_{8+\delta}$," *Phys. Rev. Lett.*, vol. 93, p. 117003, Sep 2004.

[183] T. Devereaux, A. Virosztek, A. Zawadowski, M. Opel, P. Mller, C. Hoffmann, R. Philipp, R. Nemetschek, R. Hackl, A. Erb, E. Walker, H. Berger, and L. Forr, "Enhanced electron-phonon coupling and its irrelevence to high T_c superconductivity," *Solid State Communications*, vol. 108, no. 7, pp. 407 – 411, 1998.

[184] L. Capogna, B. Fauqué, Y. Sidis, C. Ulrich, P. Bourges, S. Pailhès, A. Ivanov, J. L. Tallon, B. Liang, C. T. Lin, A. I. Rykov, and B. Keimer, "Odd and even magnetic resonant modes in highly overdoped $Bi_2Sr_2CaCu_2O_{8+\delta}$," *Phys. Rev. B*, vol. 75, p. 060502, Feb 2007.

[185] S. Johnston, W. S. Lee, and Y. e. a. Chen

[186] M. Hashimoto, E. A. Nowadnick, R.-H. He, I. M. Vishik, B. Moritz, Y. He, K. Tanaka, R. G. Moore, D. H. Lu, Y. Yoshida, M. Ishikado, K. Fujita, S. Ishida, S. Uchida, H. Eisaki, Z. Hussain, T. P. Devereaux, and Z.-X. Shen, "Spectroscopic fingerprint of the interplay between the pseudogap and superconductivity in $Bi_2Sr_2CaCu_2O_{8+\delta}$," *Submitted*, 2013.

[187] J. Graf, C. Jozwiak, C. L. Smallwood, H. Eisaki, R. A. Kaindl, D.-H. Lee, and A. Lanzara, "Nodal quasiparticle meltdown in ultrahigh-resolution pump-probe angle-resolved photoemission," *Nat Phys*, vol. 7, pp. 805–809, 2011.

[188] L. Perfetti, P. A. Loukakos, M. Lisowski, U. Bovensiepen, H. Eisaki, and M. Wolf, "Ultrafast electron relaxation in superconducting $Bi_2Sr_2CaCu_2O_{8+\delta}$ by time-resolved photoelectron spectroscopy," *Phys. Rev. Lett.*, vol. 99, p. 197001, Nov 2007.

[189] P. D. Johnson, T. Valla, A. V. Fedorov, Z. Yusof, B. O. Wells, Q. Li, A. R. Moodenbaugh, G. D. Gu, N. Koshizuka, C. Kendziora, S. Jian, and D. G. Hinks,

"Doping and temperature dependence of the mass enhancement observed in the cuprate $Bi_2Sr_2CaCu_2O_{8+\delta}$," *Phys. Rev. Lett.*, vol. 87, p. 177007, Oct 2001.

[190] T. Sato, H. Matsui, T. Takahashi, H. Ding, H.-B. Yang, S.-C. Wang, T. Fujii, T. Watanabe, A. Matsuda, T. Terashima, and K. Kadowaki, "Observation of band renormalization effects in hole-doped high-T_c superconductors," *Phys. Rev. Lett.*, vol. 91, p. 157003, Oct 2003.

[191] Z. M. Yusof, B. O. Wells, T. Valla, A. V. Fedorov, P. D. Johnson, Q. Li, C. Kendziora, S. Jian, and D. G. Hinks, "Quasiparticle liquid in the highly overdoped $Bi_2Sr_2CaCu_2O_{8+\delta}$," *Phys. Rev. Lett.*, vol. 88, p. 167006, Apr 2002.

[192] H. Takatsu, S. Yonezawa, S. Mouri, S. Nakatsuji, K. Tanaka, and Y. Maeno, "Roles of high-frequency optical phonons in the physical properties of the conductive delafossite $PdCoO_2$," *Journal of the Physical Society of Japan*, vol. 76, no. 10, p. 104701, 2007.

[193] K. Takada, H. Sakurai, E. Takayama-Muromachi, F. Izumi, R. A. Dilanian, and T. Sasaki, "Superconductivity in two-dimensional CoO_2 layers," *Nature*, vol. 422, no. 6927, pp. 53–55, 2003.

[194] M. Lee, L. Viciu, L. Li, Y. Wang, M. Foo, S. Watauchi, R. Pascal Jr, R. Cava, and N. Ong, "Large enhancement of the thermopower in Na_xCoo_2 at high Na doping," *Nature materials*, vol. 5, no. 7, pp. 537–540, 2006.

[195] G. Lang, J. Bobroff, H. Alloul, G. Collin, and N. Blanchard, "Spin correlations and cobalt charge states: Phase diagram of sodium cobaltates," *Phys. Rev. B*, vol. 78, p. 155116, Oct 2008.

[196] A. Bhalla, R. Guo, and R. Roy, "The perovskite structure–a review of its role in ceramic science and technology," *Material Research Innovations*, vol. 4, no. 1, pp. 3–26, 2000.

[197] V. Eyert, R. Fresard, and A. Maignan, "On the metallic conductivity of the Delafossites $PdCoO_2$ and $PtCoO_2$," *Chemistry of Materials*, vol. 20, no. 6, pp. 2370–2373, 2008.

[198] J. A. Sobota, K. Kim, H. Takatsu, M. Hashimoto, S.-K. Mo, Z. Hussain, T. Oguchi, T. Shishidou, Y. Maeno, B. I. Min, and Z.-X. Shen, "Electronic structure of the metallic antiferromagnet $PdCrO_2$ measured by angle-resolved photoemission spectroscopy," *to appear in Phys. Rev. B*, 2013.

[199] M. P. Seah and W. A. Dench, "Quantitative electron spectroscopy of surfaces: A standard data base for electron inelastic mean free paths in solids," *Surface and Interface Analysis*, vol. 1, no. 1, pp. 2–11, 1979.

[200] M. H. Berntsen, O. Gotberg, and O. Tjernberg, "An experimental setup for high resolution 10.5 ev laser-based angle-resolved photoelectron spectroscopy using a time-of-flight electron analyzer," *Review of Scientific Instruments*, vol. 82, no. 9, pp. 095113–095113, 2011.